Scalable Plasmonic Nanopixels

Jialong Peng
Jesus College

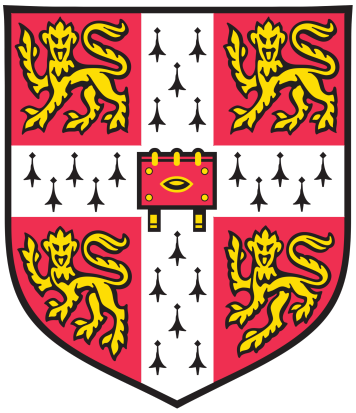

This thesis is submitted for the degree of
Doctor of Philosophy

Department of Physics
University of Cambridge

July 2020

Declaration

This thesis is the result of my own work and includes nothing which is the outcome of work done in collaboration except as declared in the Preface and specified in the text. It is not substantially the same as any that I have submitted, or, is being concurrently submitted for a degree or diploma or other qualification at the University of Cambridge or any other University or similar institution except as declared in the Preface and specified in the text. I further state that no substantial part of my thesis has already been submitted, or, is being concurrently submitted for any such degree, diploma or other qualification at the University of Cambridge or any other University or similar institution except as declared in the Preface and specified in the text. It does not exceed the prescribed word limit for the relevant Degree Committee.

Jialong Peng
July, 2020

Abstract

Scalable Plasmonic Nanopixels

Jialong Peng

Plasmonic colourations are promising for flat panel display applications due to their full-colour gamuts and high spatial resolution. However, it cannot be readily tuned and requires expensive lithographic techniques.

In this work, the concept of plasmonic nanopixels is proposed. These are fabricated by positioning electrochromic conductive polymer (*e.g.* polyaniline) coated gold nanoparticles onto a metal mirror, and termed an electrochromic nanoparticle on mirror (*e*NPoM). The tight confinement of light inside this well-defined and tiny gap volumes allows independent tuning of the individual nanoparticles, which act as active nanopixels. The scheme works by switching the charge state of the polymer shell electrically, thus rapidly shifting the resonant scattering colour of the *e*NPoM across over 100 nm wavelength ranges, in response to less than 1 V.

As the whole construction process is solution-based, electrically-driven colour-changing metafilms can be fabricated by coating these nanopixels onto films to generate distinct vivid colours. In conjunction with commercially available printing techniques, flexible patterned devices are demonstrated, offering possibilities to make fully-printed wearable plasmonic devices including displays, electronic textiles, or sensors. The whole process is lithography-free and thus readily allows to be extended with large scale processing tools, such as roll-to-roll manufacturing. Furthermore, intriguing directional optical dynamics are experimentally demonstrated in *e*NPoMs with ultra-thin metal films.

The plasmonic nanocavities not only create optical response controllable by the gap material properties which benefits for making new functional optical devices, but also allow for substantial field enhancement in the gap, offering an excellent platform for probing light-matter interactions at the nanoscale.

The nanoeletrochemistry is explored within these nanopixels. Optical dynamics of *e*NPoMs made with different conductive polymers are investigated with dark-field and Raman spectroscopy in real-time while voltage is applied. The modulation of the optical response reveals the redox mechanisms inside the tiny gap.

Dedicated to my parents.

Acknowledgements

It is an incredibly enjoyable time in NanoPhotonics Centre. My gratitude goes to many people who kindly supported me.

First and foremost, I am extremely thankful to my PhD supervisor, Jeremy Baumberg, for giving me the opportunity to join his group and his strong support throughout my PhD. His amazing enthusiasm for science is very inspiring, and his fantastic guidance for exploring the unknown always makes the hard lab work enjoyable. I have learned so much from him, not only about research but also many other transferable skills for managing work and life.

I am deeply grateful to Dr Hyeon-Ho Jeong for his support on my research. He has a great understanding of nanoscience, and is familiar with almost all sorts of nanofabrications. I sincerely thank him and hope everything is going well for him as an independent leader for his research group.

NanoPhotonics group is very stimulating and welcoming. Everyone in the group is always happy and ready to help. The discussions, collaborations, and friendships with them are beneficial. In particular, I would like to thank Sean Cormier, Qianqi Ivana Lin, Rohit Chikkaraddy, Hsin-ling Liang for their direct help in experiments. I also would like to thank Junyang, Wenting, Shu, Yidong, Wilson, Andrew, Will, Jack, Eoin, Demelza, Charlie, Bart, Marlous, Matthew, Dean, Laura and all other members in the group. They are generous to offer help whenever I am struggling with anything in labs.

I would also like to express special thanks to the collaborators: Michael F.L. De Volder, Silvia Vignolini, and Mélanie M. Bay from the R2R team, Michael Smith and Sohini Kar-Narayan from Materials Science, Bruno Pinho and Laura Torrente from Chemical Engineering, and Xuezhi Zheng from KU Leuven. They are very friendly and have provided constant support in different areas.

I am very grateful for the support from the university staff: lab technicians Anthony and Giovanni, Colin and the IT team, and the hub administrative staff. They made my research work much easier.

I would like to acknowledge the financial support for my PhD funding from the China Scholarship Council. My PhD research would not have been possible without this generous support.

Finally, I am most thankful for my parents. I am so lucky to have their love and continuous support.

List of Publications

[1] Jialong Peng, Hyeon-Ho Jeong, Michael Smith, Rohit Chikkaraddy, Qianqi Lin, Hsin-Ling Liang, Michael F. L. De Volder, Silvia Vignolini, Sohini Kar-Narayan and Jeremy J. Baumberg. Fully-printed flexible plasmonic metafilms with directional color dynamics. *Advanced Science*, 2020, 2002419.

[2] Jialong Peng, Hyeon-Ho Jeong, Qianqi Lin, Sean Cormier, Hsin-Ling Liang, Michael F. L. De Volder, Silvia Vignolini, and Jeremy J. Baumberg. Scalable electrochromic nanopixels using plasmonics. *Science Advances*, 5(5):eaaw2205, 2019.

[3] Hsin-Ling Liang, Mélanie M. Bay, Roberto Vadrucci, Charles H. Barty-King, Jialong Peng, Jeremy J. Baumberg, Michael FL De Volder, and Silvia Vignolini. Roll-to-roll fabrication of touch-responsive cellulose photonic laminates. *Nature Communications*, 9, no. 1 (2018): 4632.

In preparation:

[1] Jialong Peng, Qianqi Lin, Hyeon-Ho Jeong and Jeremy J. Baumberg. Tracking redox dynamics of nanosized conductive polymer in plasmonic nanopixels.

Contents

1. Introduction

The colours of objects arise from light-matter interactions, involving processes like reflection, diffraction, absorption, or scattering of light. Colours are visually perceived depending on what wavelength ranges of light reach our eyes. For instance, dyes and pigments render vibrant colours by absorbing specific ranges of visible light and reflecting the remaining.

Structural colouration is another way to produce hues. The iridescence of floating oil films, opal gemstones, and many other naturally occuring structures such as butterfly wings are vivid real-life examples [1, 2]. They are generally based on dielectric multilayers, periodic gratings/arrays or photonic crystal structures, interacting with light by interference or diffraction [3] (Figure 1.1). The advantage of structure-based colouration is that it can avoid toxic chemical components and provide long-term durability. However, these types of structures have limited spatial resolutions, and often suffer from viewing-angle problems due to the angular-dependent interference/diffraction conditions.

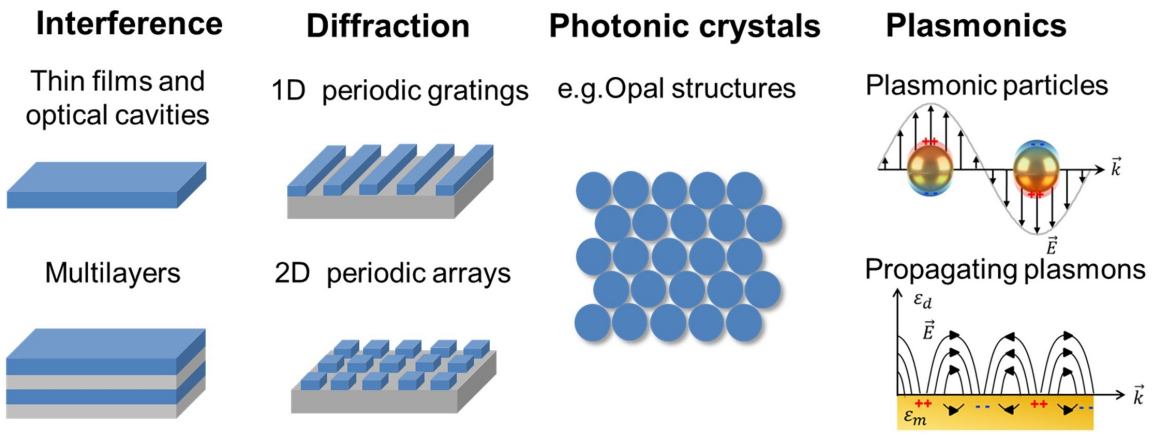

Fig. 1.1 Different mechanisms for structural colouration.

Metallic nanostructures can generate structural pigmentation. When light shines on a metallic nanostructure, the free electrons in the metal surface start to resonantly oscillate, producing distinct colours because of preferential light absorption and scattering. This is called plasmonic resonance [4], and it confines the light to a sub-wavelength volume, leading to extremely high spatial resolution. Plasmonic resonance is affected by the material properties and geometry of metallic structures, so desired colours can be obtained by engineering the architecture of the structures. Recent advances in nanofabrication provide the ability to achieve precise morphologies. Complex metallic nanostructures have been fabricated with rich colour gamuts and high spatial resolution [5].

However, benefits from plasmonic colouration devices often remain in academia. Part of the problem is that it is hard to make them active and the high cost and difficult scalability of nanofabrication. In this thesis, the main aim is to develop optical nanostructures that can give strong colour change effects on demand, and can be manufactured in a scalable approach. A concept of a plasmonic nanopixel is presented in this work by combining plasmonic nano-dimer type structure with conductive polymers. Electrically-tunable vivid colour dynamics are demonstrated with this concept and scalable from the single nanoparticle level to multi-centimetre scale films. Notably, all fabrication processes are solution-based and lithography-free, readily allowing for possible industrial-scale manufacturing.

Thesis Outline

The structure of the thesis is as follows:

Chapter 2 provides the fundamentals to understand the experimental results. The plasmonics theory is overviewed initially, focused on light interactions with plasmonic nanoparticles. A brief review is then given of the plasmonic colour generation mechanism and its applications in the dynamic display field. Finally, conjugated conductive polymers are introduced, which are extensively used in subsequent experiments.

Chapter 3 presents the main experimental methods. Optical microscopies including bright-field/dark-field and Raman spectroscopy are described, which function as non-invasive techniques to characterise the optical properties of plasmonic nanostructures in real-time. Numerical simulations help gain an understanding of the optical response of plasmonic systems which may not be experimentally accessible.

Chapter 4 introduces the functional unit of the nanopixel - Electrochromic Nanoparticle on Mirror construct (*e*NPoM), which is made by positioning a conductive polymer coated plasmonic nanoparticle onto a metal mirror. Reversible optical switching is achieved by changing the charge state of the entire polymer shell, rapidly shifting the *e*NPoM resonant scattering colour. The influence of different gap thickness and the correlation between electrical and optical switching dynamics is also investigated.

Chapter 5 demonstrates the applications of *e*NPoMs. Scalable electrically-driven colour-changing metafilms are fabricated by two lithography-free methods: meniscus-guided nanoparticle assembly and aerosol jet printing. Patterned devices are made on both solid and flexible substrates. Intriguing directional optical effects and dynamics are found in *e*NPoMs with ultra-thin metal films.

Chapter 6 explores the redox dynamics of nanosized conjugated conductive polymer within the nanopixels. Optical dynamics of *e*NPoMs made with different conjugated conductive polymers are characterised with dark-field and Raman spectroscopy in real-time while voltage is applied. The modulation of the optical response reveals the redox dynamics inside the tiny gap.

Chapter 7 summarises the main results and gives an outlook of interesting directions to explore in the future.

2. Background

In this chapter, the theoretical fundamentals required for understanding the experimental results are presented. Light interaction with metals is discussed with plasmonics theory. The nanoparticle-on-mirror construct is introduced with its key optical properties. Plasmonic resonances build the foundation for plasmonic colour generation. A brief review is given of the plasmonic colour generation mechanism with its applications in the dynamic display field, followed by an introduction of stimulus-responsive materials with a focus on conjugated conductive polymers.

2.1 Fundamentals of Plasmonics

2.1.1 Dielectric Function of Metals

The dielectric function of metals is dominated by the electrons in the conduction band. Electrons partially fill this band and are free to move within it, making metals conductive. They can be modelled as a free electron gas moving against a background of positively charged ions, which is referred to as the Drude model and commonly used for modelling the optical properties of metals.

Exposed to an external electric field $\mathbf{E}$, the electrons of charge e undergo simple harmonic oscillations. Their displacement $\mathbf{x}$ over time t, with the electron mass m, can be described by the equation [4]

$$m\frac{d^2\mathbf{x}}{dt^2} + m\gamma\frac{d\mathbf{x}}{dt} = -e\mathbf{E} \tag{2.1}$$

where γ is the damping coefficient. Assuming harmonic time dependence for both $\mathbf{E}$ and $\mathbf{x}$, solution of this equation results in the relation

$$\mathbf{x} = \frac{e}{m(\omega^2 + i\gamma\omega)}\mathbf{E} \tag{2.2}$$

where $\mathbf{E} = \mathbf{E_0}\exp^{-i\omega t}$, $\mathbf{x} = \mathbf{x_0}\exp^{-i\omega t}$, and ω is the frequency. This describes the response of a single electron, and can be used to calculate the macroscopic polarisation $\mathbf{P}$, considering all the individual dipole moments $e\mathbf{x}$ with electron density n,

$$\mathbf{P} = -ne\mathbf{x} = -\frac{ne^2}{m(\omega^2 + i\gamma\omega)}\mathbf{E} \tag{2.3}$$

The dielectric function ε is obtained by the ratio of polarisation to external field as

$$\varepsilon(\omega) = 1 + \frac{\mathbf{P}}{\varepsilon_0\mathbf{E}} = 1 - \frac{\omega_p^2}{\omega^2 + i\gamma\omega} \tag{2.4}$$

where ε_0 is the permittivity of free space, and ω_p is characteristic plasma frequency defined by

$$\omega_p = \sqrt{\frac{ne^2}{\varepsilon_0 m}} \tag{2.5}$$

Considering also the effects of bound electrons as a constant ε_∞ [6], the total dielectric function can be rewritten as

$$\varepsilon = \varepsilon_\infty - \frac{\omega_p^2}{\omega^2 + i\gamma\omega} \tag{2.6}$$

This gives the dielectric function of metals in the Drude model.

However, the Drude model does not take into account the interband transitions of electrons and thus is limited to longer wavelengths (> 500 nm). For gold, the interband transitions happen below 500 nm, which results in increased absorption in this region. A comparison of the dielectric function of gold from experimental data [7] and a Drude model fit [8] is shown in Figure 2.1. Generally, the Drude model applies well for metals such and gold and silver above 500 nm, covering the relevant spectral region for this thesis.

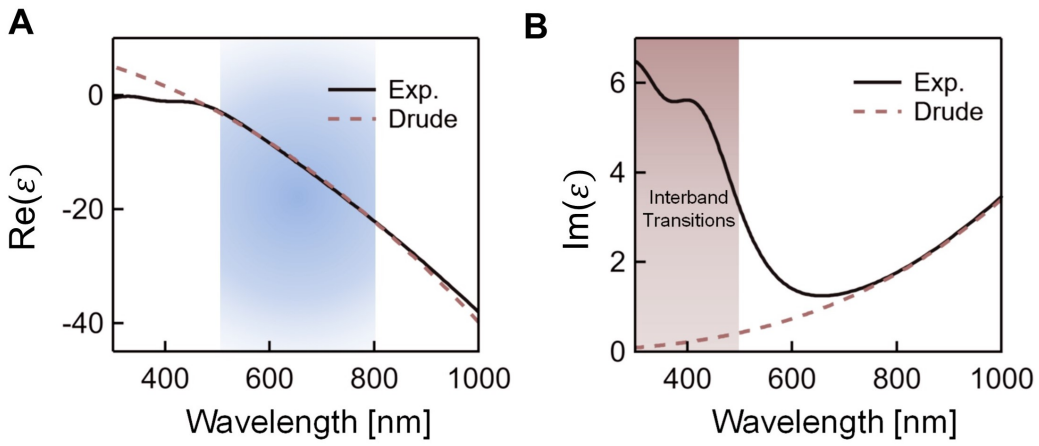

Fig. 2.1 Dielectric function of gold by Drude model. (A) Real part. (B) Imaginary part. The solid line shows experimental data from Johnson and Christy [7] and the dotted line is the prediction of the Drude model. Blue shaded region shows the relevant spectral region for this thesis. Figure adapted from [8].

2.1.2 Surface Plasmons

When an electromagnetic wave is incident on a metal, the electrons near metal surface feel the incident electromagnetic field giving forces. If the induced collective free-electron oscillations can propagate along the metal-dielectric interfaces, it is termed a surface plasmon polariton (Figure 2.2 A). If the induced modes are spatially confined to sub-wavelength scale nanostructure surfaces, they are called localised surface plasmon polaritons (Figure 2.2 B).

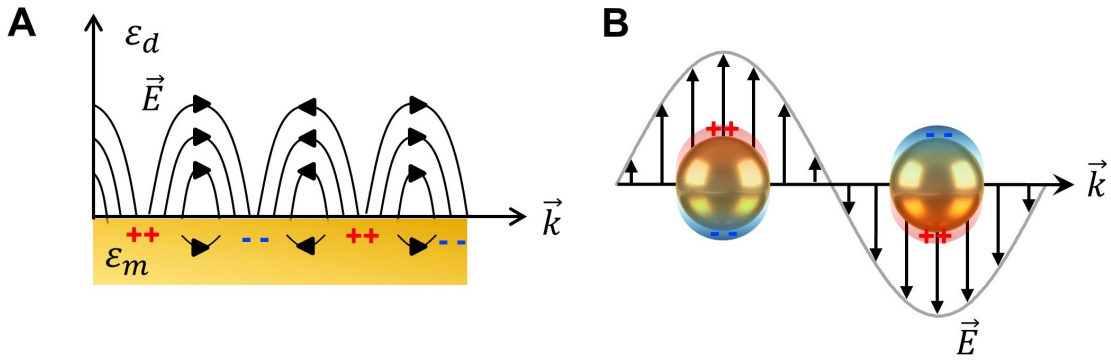

Fig. 2.2 Illustrations of propagating and localized surface plasmons. (A) Surface plasmon (SPPs) propagating along a metal-dielectric interface. (b) Localized Surface Plasmons (LSPs) bound to a nanoparticle surface.

Propagating Surface Plasmons

Propagating Surface Plasmons (SPPs) are bound to the metal-dielectric surface, and the electric field decays exponentially away from the interface. The dispersion relation for a propagating SPPs is given by [4]

$$k = \frac{\omega}{c}\sqrt{\frac{\varepsilon_m \varepsilon_d}{\varepsilon_m + \varepsilon_d}} \tag{2.7}$$

where k is the wavenumber of SPPs, ε_m, ε_d are the dielectric functions of metal and dielectric, respectively. This dispersion relation does not allow direct excitation of SPPs by free-space waves due to the momentum mismatch. Because ε_m is negative in the visible region, meaning that $k > \frac{\omega}{c}$, *i.e.*, SPPs have a higher momentum than the photon. Coupling techniques such as grating or fibre coupling have been developed to excite SPPs effectively [4].

Localised Surface Plasmons

However, direct excitation of plasmon can be obtained in sub-wavelength metal nanostructures, where the light is confined to the surface of the nanostructures, known as localised surface plasmons (LSPs). Plasmonic nanoparticles are the most common structure for supporting LSP, as their curved surfaces easily allow for free-wave excitation. The LSPs properties of nanoparticles are dominated by their sizes, shapes, materials and proximities to other plasmonic structures, providing ample tuning space for light manipulation.

The simplest structure is a spherical metallic nanoparticle, and its LSP resonances can be analytically derived in a quasi-static approximation (for particle size $\lesssim 100$ nm) [4]. Under this approximation, the particle can be modelled as an oscillating dipole with a polarisability α

$$\alpha = 4\pi R^3 \frac{\varepsilon_m - \varepsilon_d}{\varepsilon_m + 2\varepsilon_d}, \tag{2.8}$$

where R is the radius of nanoparticle, ε_m and ε_d are the permittivity of the nanoparticle and the surrounding dielectric, respectively [9]. This results in the plasmonic resonance condition $\varepsilon_m = -2\varepsilon_d$, making the plasmon resonance very sensitive to the refractive index of the surrounding medium, which is the basis for plasmonic sensing and active tuning. The scattering σ_{scat}, extinction σ_{ext} and absorption σ_{abs} cross-sections of

spherical metallic nanoparticles are given by [4]

$$\sigma_{\text{scat}} = \frac{k^4}{6\pi}|\alpha|^2 \tag{2.9}$$

$$\sigma_{\text{ext}} = k\,\text{Im}(\alpha) \tag{2.10}$$

$$\sigma_{\text{abs}} = \sigma_{ext} - \sigma_{scat} = k\,\text{Im}(\alpha) - \frac{k^4}{6\pi}|\alpha|^2 \tag{2.11}$$

where $k = \frac{2\pi n}{\lambda}$ is the wavenumber, and $n = \sqrt{\varepsilon_d}$ is the refractive index of the dielectric surroundings. It is notable that $\sigma_{\text{scat}} \propto R^6$ and $\sigma_{\text{abs}} \propto R^3$, so for smaller particles absorption dominates, while for larger particles scattering is more prominent.

2.1.3 Plasmonic Coupling - Hybridisation

Plasmonic coupling happens when plasmonic nanostructures are in close proximity, which leads to additional coupled resonances. Plasmonic coupling can be described by a hybridisation model of two identical nanoparticles, analogous to the formation of molecular orbitals with two atoms [10, 11], as shown in Figure 2.3. According to whether the overall net dipolar moment is aligned or cancelled, the dimer shows 'bright' modes which can couple to light, or 'dark' modes which cannot couple to light and thus are not visible in the scattering spectra.

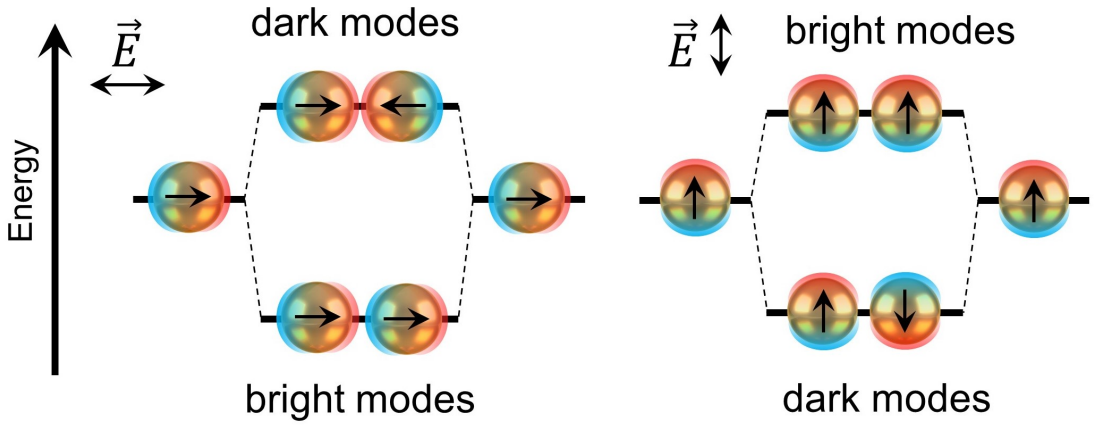

Fig. 2.3 Schematics of the hybridisation model for a nanoparticle dimer, with electric field along or perpendicular to the dimer axis. Figure adapted from [10].

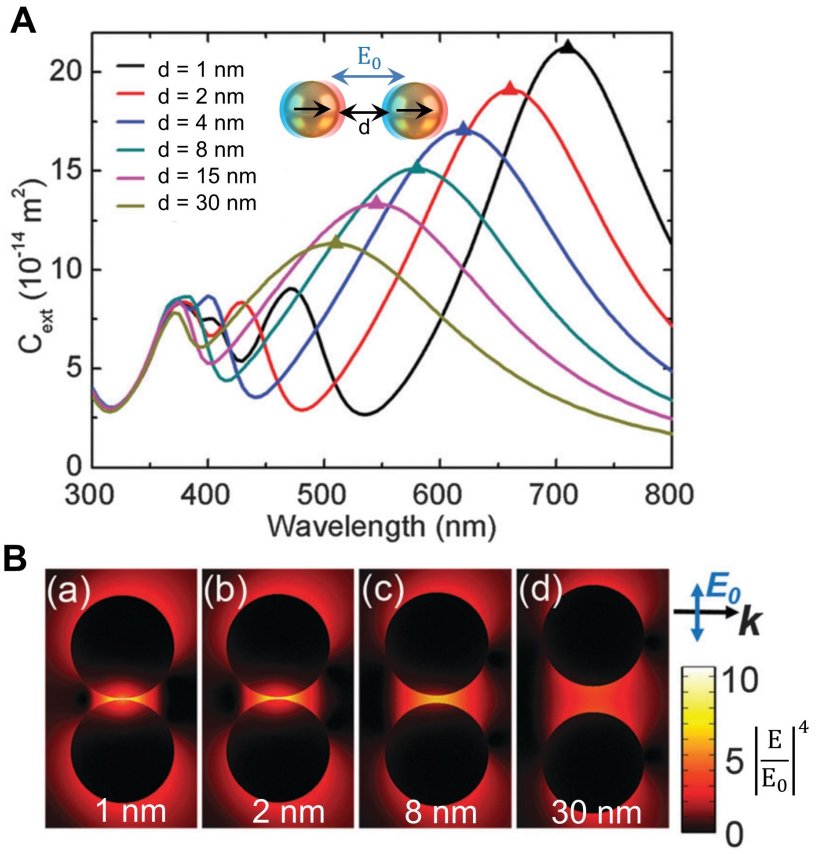

Fig. 2.4 Optical properties of coupling plasmonic dimers. (A) Calculated extinction cross-sections for 60 nm radius silver nanoparticle (Ag NP) dimers *vs* different gap sizes d and (B) the near-field electric field enhancement of (a) d =1 nm, λ = 700 nm, (b) d =2 nm, λ = 660 nm, (c) d =8 nm, λ = 610 nm, and (d) d = 30 nm, λ = 570 nm. The electric field is polarised parallel to the dimer axis and n_{gap}= 1. Figure adapted from [12].

The plasmonic coupling leads to two crucial features useful for applications:

(i) the coupled resonance is highly sensitive to the spacing between particles. As shown in Figure 2.4 A, the coupled resonance redshifts with the gap spacing d decreasing, shifting from around 500 nm to 700 nm when d decreases from 30 nm to 1 nm, which means the coupled resonance can be tuned effectively with controlled gap spacing. Additional modes around the 400-500 nm shorter wavelength region correspond to higher-order modes and are not as sensitive as the coupled mode to the gap spacing.

(ii) the near-field intensity is strongly enhanced in the dimer gap, termed as 'hotspot'. The field intensity is up to 10^6 for d = 1 nm gaps while lower than 10^3 for d = 30 nm gaps (Figure 2.4 B) [12]. The extremely strong field enhancement from small-size gaps

offers unique possibilities for exploring light-matter interaction, down to the single molecule level [13].

2.1.4 Nanoparticle-on-mirror constructs

The nanoparticle on mirror construct (NPoM) consists of a metal nanoparticle (NP) placed over a flat metal substrate with a small dielectric gap. The oscillating charges in the nanoparticle induce image charges in the flat metal substrate, resulting in a dipolar coupling which appears as an effective dimer system (Figure 2.5) [13–15]. Enclosed nanocavities formed in the gap exhibit substantial field enhancement upon the resonant condition. The NPoM is the main plasmonic construct used in this thesis, typically made by gold nanoparticles (Au NP) on a gold mirror.

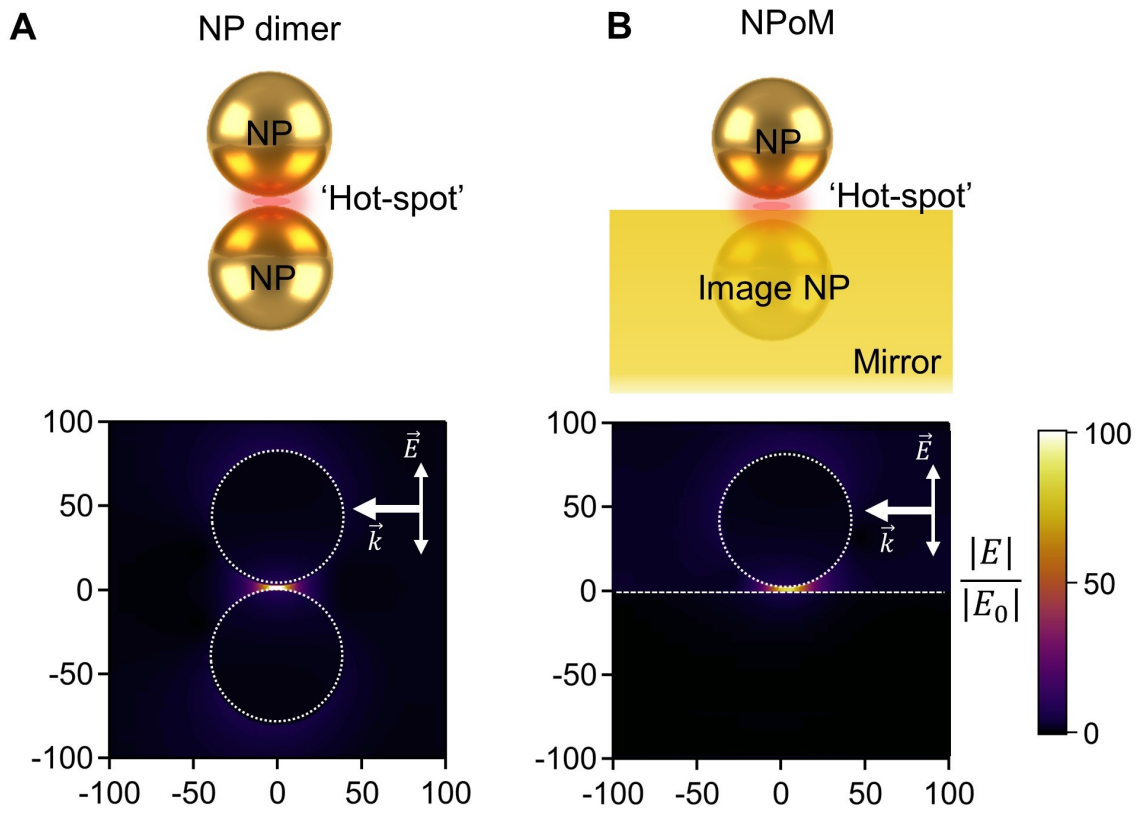

Fig. 2.5 Schematics of (A) coupled Au NP dimer and (B) Au NPoM. Bottom panel shows simulated near-field enhancement at resonance for the 80 nm Au NP dimer and Au NPoM with 3 nm gap (n=1). Equivalent near-field enhancement reaches $\sim 10^4$ in the 'hot-spot'.

The NPoM construct has several advantages compared with other plasmonic dimer systems, especially in its simplicity and reproducibility of fabrication. Traditional top-down techniques such as e-beam lithography [16] can fabricate arrays of plasmonic dimer systems with controlled sizes and shapes, but are rather expensive and time-consuming, not ideal for large scale production. Moreover, the particle spacing < 10 nm is rather challenging to control [17]. Bottom-up methods like chemical self-assembly with molecular linkers are capable of spatial control less than a nanometre [18–20], but generally have low yields and tend to produce aggregates. For NPoMs, by simple drop-casting a large number of plasmonic dimer systems can be efficiently prepared with high precision and excellent reproducibility, make it an ideal platform of cavity plasmonics.

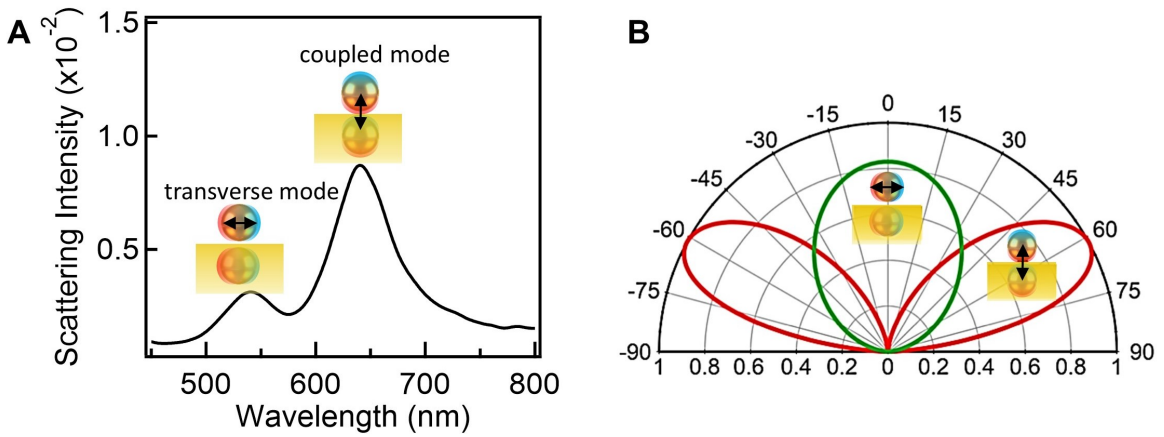

Fig. 2.6 (A) Experimental dark-field scattering response of a 80 nm Au NPoM with a 5 nm polymer poly(N-isopropylacrylamide) spacing layer. Two different modes are identified. (B) Simulated emission profile of the NPoM system. Figure adapted from [21].

A typical dark-field scattering spectrum of Au NP on a gold mirror with a thin polymer spacing is shown in Figure 2.6 A. Two distinct plasmonic modes are identified: a mode of horizontal charge oscillation in the Au NP weakly coupled to the gold mirror (transverse mode), and a mode strongly coupled to the gold mirror (coupled mode) [13]. The transverse mode emits upwards while the coupled mode scatters at a high angle (calculated angular emission patterns see Figure 2.6 B). The coupled mode show maximum emission at $\sim 60°$, making the optical excitation of NPoMs different from other nano-dimer systems. High-angle optical illumination is needed to excite both modes effectively. In practice, this is achieved by objectives with high numerical aperture. These two modes dominate the NPoM scattering, since other higher-order

modes generally occur at higher energies or have lower radiative efficiencies (detailed discussions are found in the review paper [13]).

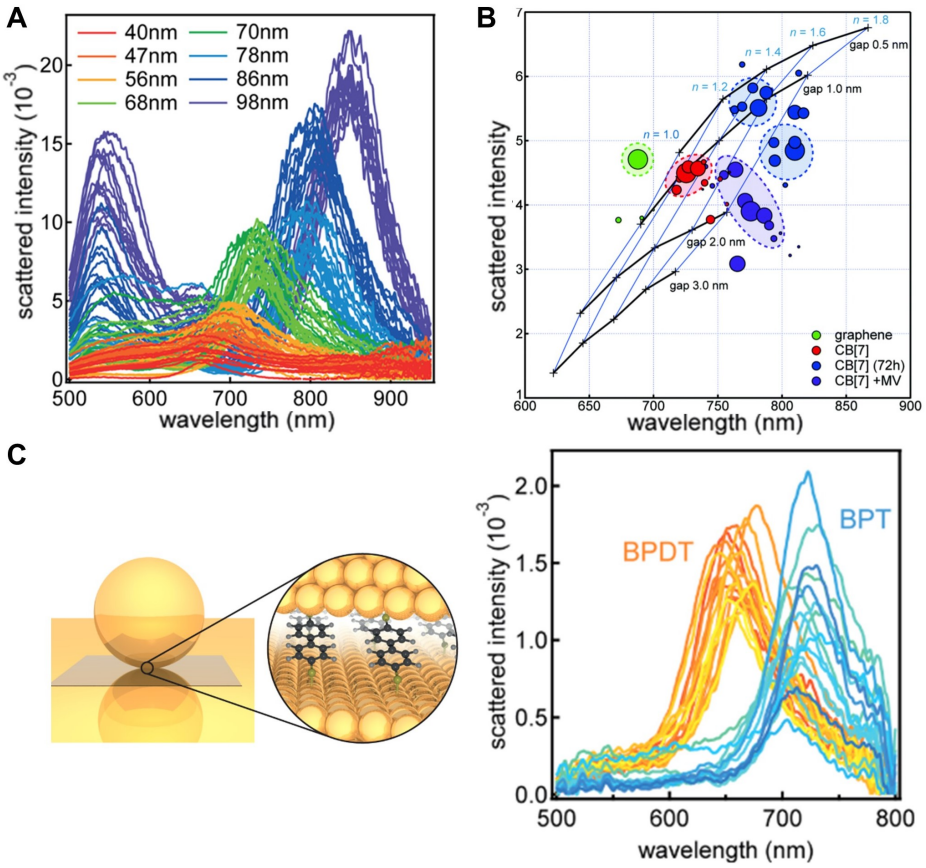

Fig. 2.7 Tuning parameters for NPoM constructs. (A) Scattering spectrum of different Au NPoMs with sizes varying from 40 - 100 nm. Figure adapted from [22]. (B) Gap size and refractive index dependence of Au NPoM. This was demonstrated by using different gap materials such as graphene or cucurbit-7-uril (CB[7]), and loading the CB[7] with guest molecules like methyl-viologen (MV). Figure adapted from [23]. (C) Au NPoM with a self-assembled monolayer as gap material. The NPoM coupled mode resonance blueshifts around 50 nm when the SAM changes from an insulating BPT molecule to more conductive BPDT. Figure adapted from [24].

The coupled mode is susceptible to the nanoparticle properties (sizes, shapes, materials), the surrounding refractive index, and the gap parameters including gap sizes and gap material properties (Figure 2.7). The resonance position of the coupled mode redshifts almost linearly as the diameter of the nanoparticle increases (Figure 2.7 A) [25], and also redshifts with increasing gap refractive index, due to the better confined electric field in the gap with high n (Figure 2.7 B) [23]. The properties of gap materials have

a considerable effect on the optical response of the NPoM. For example, changing the gap material from an insulating biphenyl-4-thiol (BPT) self-assembled monolayer (SAM) to more conductive biphenyl-4,4'-dithiol (BPDT) SAM makes the coupled mode blueshift, influenced by the molecular conductive link between the neighbouring plasmonic structures [24]. In contrast, the transverse mode is not sensitive to the gap conditions as it merely couples weakly to mirror [26].

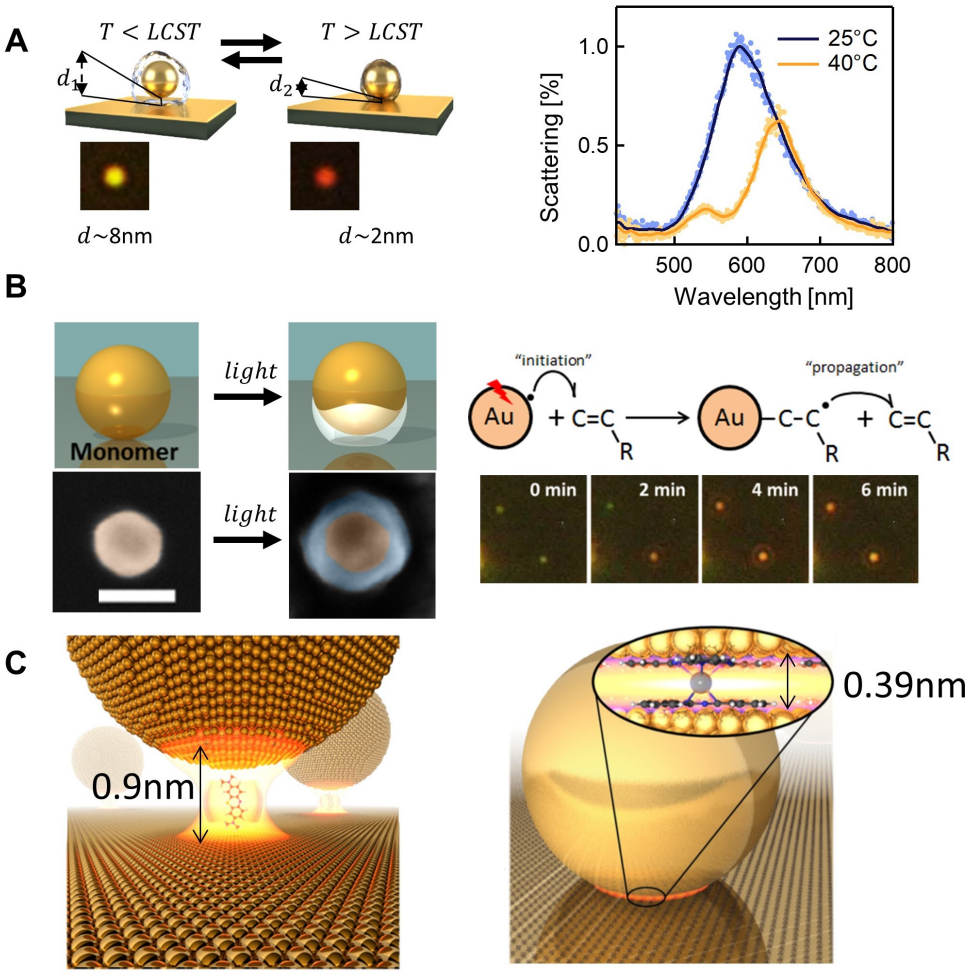

Fig. 2.8 Applications of NPoM constructs. (A) Single-nanoparticle switch made by thermo-responsive polymer poly(N-isopropylacrylamide) coated Au NPs on Au mirror. Opto-thermally-induced gap distance change leads to the scattering switching. Figure adapted from [8, 27]. (B) Hot-electron induced polymerization dynamically grows local polymer coatings. The resulted gap size change tunes the plasmon resonances. The scale bar is 100 nm. Figure adapted from [28]. (C) Sub-nanometre gap strongly enhances the local field intensities, which could be used to expore from single-molecule strong coupling to quantum effects [24, 29]. Figure adapted from [30, 31].

In summary, the simplicity and reproducibility of large-scale fabrication, the strong field enhancement in the gap, the ample tuning parameter space of optical response together with the sensitivity of the plasmonic coupling between nanoparticles and mirror, have made NPoM constructs an extremely plausible platform for making new devices with functional gap materials and probing light-matter interactions at the nanoscale. The advantages of NPoM have been successfully proved in various applications (Figure 2.8). New active devices have been proposed by exploiting novel functional gap materials, such as stimulus-materials like thermo-responsive poly(N-isopropylacrylamide) [27, 32, 33], or by changing the gap conditions to modify far-field optical properties (Figure 2.8 A). Combined with surface-enhanced Raman spectroscopy, new details of physics and chemistry can be explored through purely optical means [13, 22, 34–36].

2.2 Plasmonic Colouration

Plasmonic colouration describes the structural pigmentation generated by metallic nanostructures and has emerged as a critical application space for plasmonics. The applications of plasmonic colouration can be dated back to the fourth century AD for the celebrated Lycurgus Cup [37], which appears green/red coloured in reflection/transmission. The colouring mechanism behind this is that the localized surface plasmon resonances (LSPRs) from the dispersed gold and silver nanoparticles in this glass generate different colours in reflected or transmitted light, which has inspired uses from colourful church windows [38], daguerreotypes [39], to the burgeoning field of plasmonic displays [5].

2.2.1 Plasmonic Colour Generation

The preferential light absorption and scattering supported by plasmonic nanostructures at resonance, emerge as distinct resonant features giving rise to plasmonic colouration. Current advances in nanolithography provide the ability to fabricate complex plasmonic building blocks that generate a rich set of colours while keeping their overall size small.

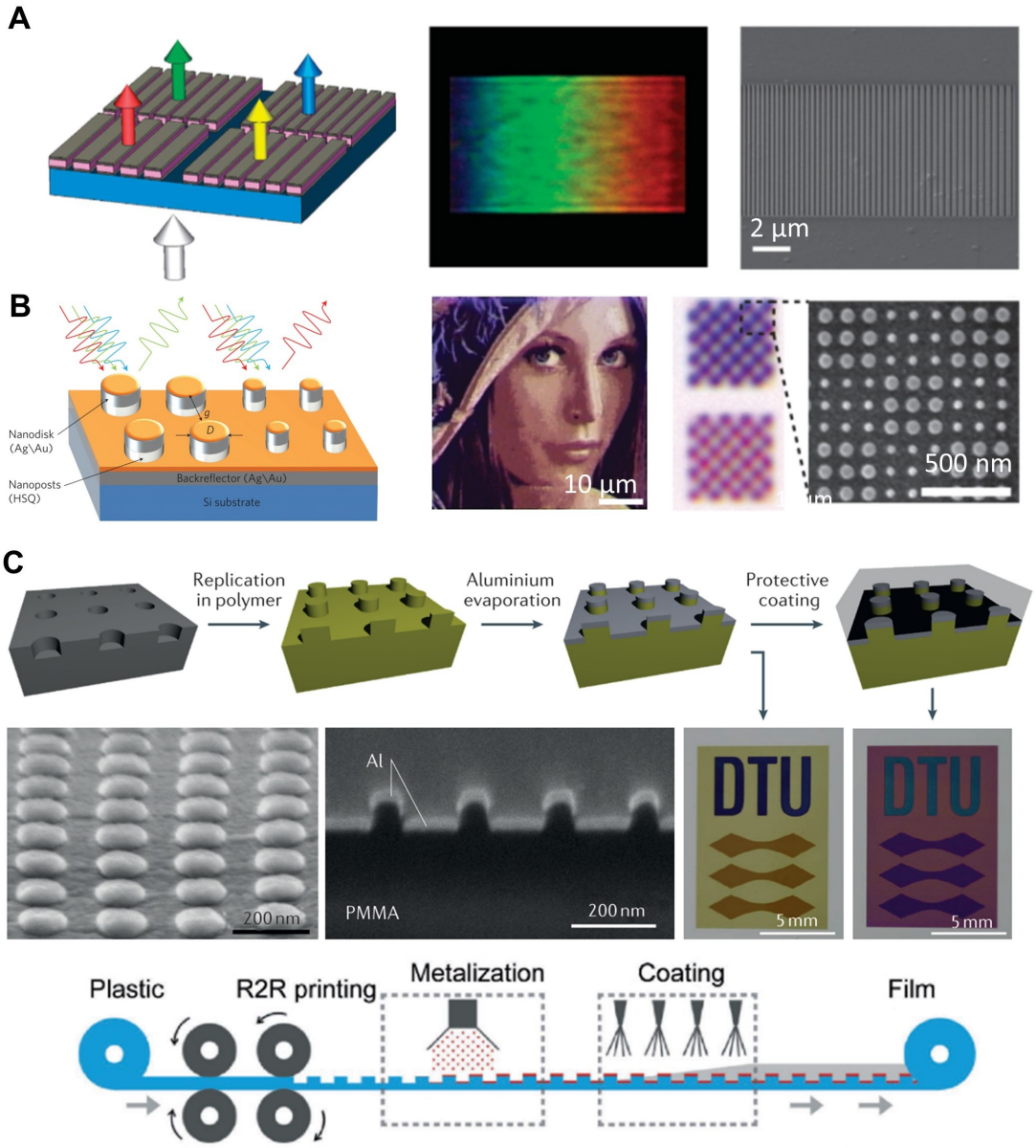

Fig. 2.9 Colour generation from plasmonic nanostructures. (A) Plasmonic colour filters made by MIM grating structure. Its colour changes from red to blue when the pitch of the gratings changes from 400 to 200 nm. Figure adapted from [40]. (B) High-resolution plasmonic printing by metal (Au/Ag) disk arrays on a metallic mirror. A full-colour Lena image is made with 250 nm pixel sizes. Figure adapted from [41]. (C) Large-scale patterning of plasmonic nanostructures. Disk-hole arrays are transferred from an e-beam patterned silicon master template to a polymer layer by nanoimprint lithography. A subsequent metal deposition process then achieves plasmonic colour structures. Industrial-scale platform like roll-to-roll processing can be readily integrated for mass production. Figure adapted from [42, 43].

Selective colour filtering can be achieved by metallic nanograting structures [5, 40]. For example, Xu *et al.* [40] made a Metal-Insulator-Metal (MIM) stack grating structure, composed of a dielectric spacing sandwiched between two metallic layers (Figure 2.2 A). The MIM structure can efficiently couple light in and out at the lower and upper metal-dielectric interfaces, through the hybridization of propagating surface plasmon modes and LSPR modes. The filtered colours can be controlled by varying the stack grating periodicities or the layer thickness. The filters are fabricated by focussed ion beam milling and are 1-2 orders of magnitude thinner than commercial colour filters used in liquid crystal displays.

High-resolution plasmonic patterns can be achieved due to the tight field localisation of plasmonic nanostructures. Nanoantenna-type structures like nanodisk or nanohole array [41, 44] are typical examples for realising colour patterning below the size of diffraction limit, due to their larger scattering and absorption cross-sections compared with their actual physical sizes [4]. By controlling the size and position of the plasmonic building blocks, full-colour patterns can be made. About 100,000 dots per inch (DPI) resolution is achieved with 250×250 nm^2 pixel size by electron-beam (e-beam) lithography (Figure 2.2 B) [41].

However, nanofabrication based on lithography techniques is generally expensive and time-consuming, not ideal for large-scale fabrication. Nanoimprinting is one of the plausible solutions, although a template master still needs to be prefabricated with lithography techniques. Nanoimprinting uses the prefabricated template to transfer desired patterns into a polymer-resist-coated substrate, replicating the desired patterns via mechanical deformation or UV-crosslinking (Figure 2.2 C) [45]. It can be extended with roll-to-roll (R2R) processing, highly suitable for mass production [46]. Other bottom-up fabrication techniques like colloidal lithography [47, 48] are useful for but limited to nanohole-type structures, so not discussed here.

In summary, compared with conventional pigment-based colouration, plasmonic colouration offers a range of advantages, including extremely high spatial resolution beyond the diffraction limit, long-term durability with non-fading colouring, and vibrant colour gamuts using simple metallic components, holding great potentials for real-life applications such as surface decoration, optical sensing or anti-counterfeiting labelling [5]. However, they have been limited to generation of static colours obtained by intricate arrangements of scattering elements [43]. Dynamic control is highly desired for display type devices.

2.2.2 Plasmonic Colour for Display Applications

Different from backlit or emissive displays made by liquid crystal displays (LCDs) or light-emitting diodes (LEDs) and organic LEDs, plasmonic display applications are generally 'reflective' type and can be read under ambient light, which provides very low energy consumption and are suitable for applications like electronic paper, 'always-on' shelf labels or building-scale displays. Active plasmonic colours can be obtained when the optical properties of the surrounding media are controlled by an applied stimulus [43]. Stimulus-responsive materials are most commonly used.

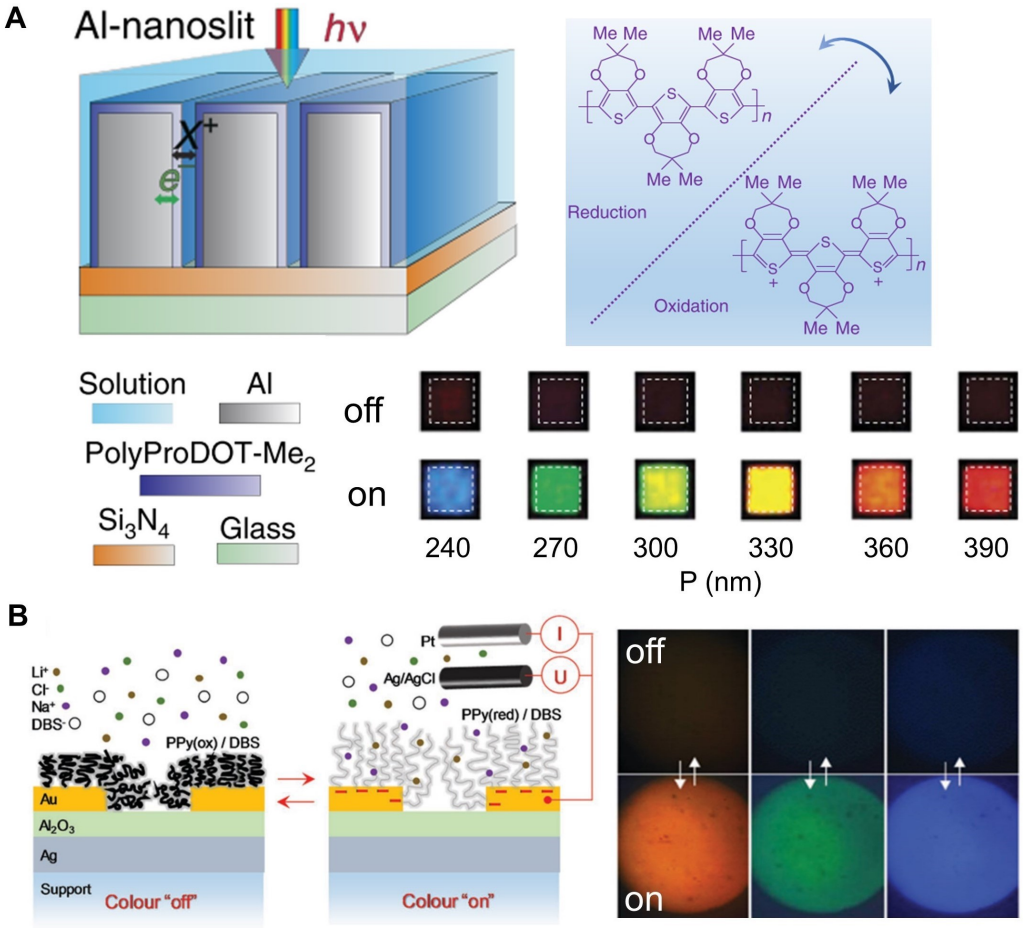

Fig. 2.10 Plasmonic colour switching. (A) Plasmonic electrochromic electrodes composed of a PolyProDOT-Me_2 coated Al-nanoslit array. The colour appearance is tuned by the slit pitch P and the on-off switching is achieved by changing the redox state of PolyProDOT-Me_2. Figure adapted from [49]. (B) Plasmonic electronic paper with RGB colour on-off switching. The colour is generated by interference between the silver mirror and gold nanohole array. Figure adapted from [50].

By integrating electrochromic materials such as conductive polymers [49–51] and phase change materials [52], plasmonic colouration can be switched on and off. Full-colour plasmonic electrodes have been fabricated by aluminium (Al) nanoslits (Figure 2.10 A) [49]. The colours are set by the pitch sizes, and the on-off switching is achieved by changing the redox state of PolyProDOT-Me_2, an electrochromic polymer having broadband optical absorption when oxidised thus being able to turn off the plasmonic colours. Electrochromism is defined as the reversible change of a material's colour induced by an external electrical stimulus [53]. Common electrochromic materials include many conjugated conducting polymers and transition metal oxides [54]. The colour change ascribes to the generation of electronic absorption bands in the visible region, on switching the redox states [55]. Similarly, plasmonic electronic paper with RGB colours could be fabricated with conductive polymers such as polypyrrole [50] or poly(3,4-ethylenedioxythiophene) [51]. The RGB colours are rendered by interference between the silver mirror and gold nanohole array, and different light-absorption properties of the polymer's oxidized/reduced states switch the colouration (Figure 2.10 B). These combinations also enhance refresh rates and optical contrast by up to two-fold compared to the electrochromic materials alone [49]. However, the limitation lies in that only intensity switching is achieved, not dynamic colour tuning.

A continuous refractive index change is required while keeping the plasmonic resonant features in the visible range to achieve dynamic plasmonic colour tuning. For instance, Au nanostructures coated with Ag shells show full-colour dynamics through electrochemical control of the Ag shell thickness or redox state [56, 57]. The reflection peak can be tuned continuously from around 430 to 650 nm, spanning the visible colour region (Figure 2.11 A). However, rapid nanoscale morphological changes happen during the repeated Ag stripping/redepositing process, making it not durable for long-term usage ($<$ 1 month [58]). Conventional electrochromic oxide WO_3 have also been combined with gap plasmon resonators to achieve polarization-dependent colour tuning in solid state (Figure 2.11 B). The refractive index of WO_3 can be tuned continuously from $n = 2.1$ to 1.8 upon electrochemical lithiation/delithiation, which leads to a 58-nm reflection peak shift [59]. However, as the ionic diffusion is slow, these colour tuning approaches take from a few seconds [56, 57] to several minutes [59], not ideal for video-rate applications.

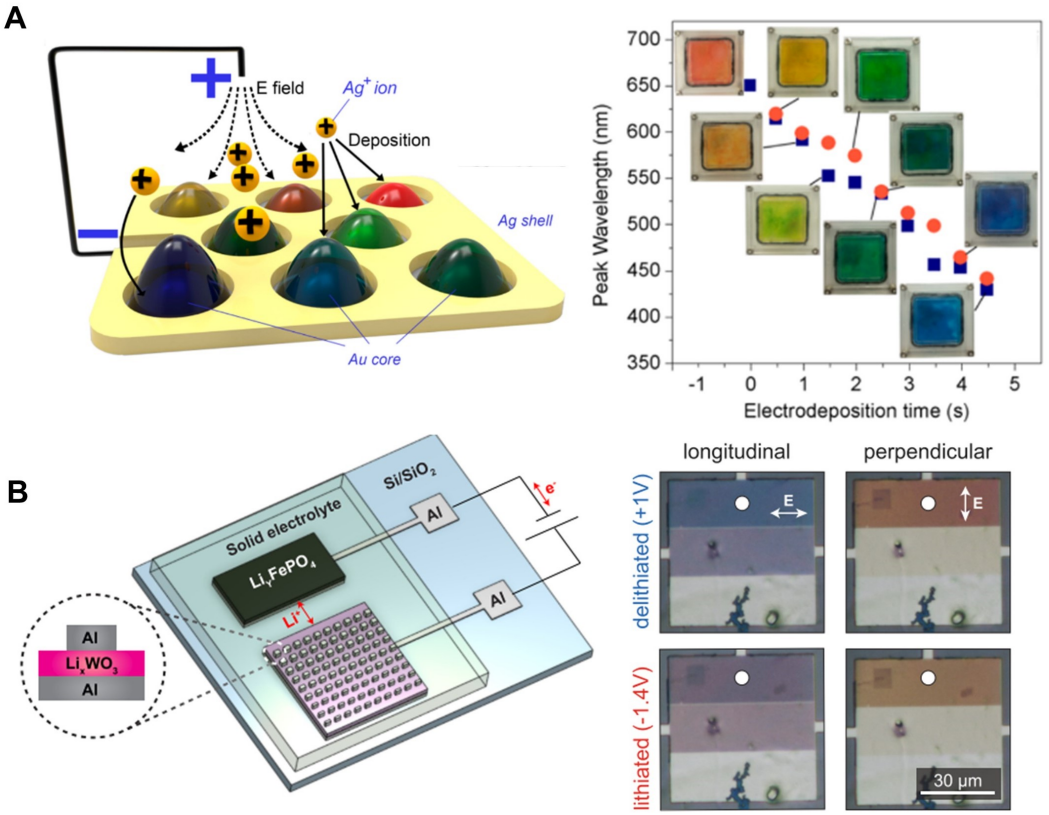

Fig. 2.11 Plasmonic colour tuning. (A) Dynamical full visible colour generation enabled by electrochemically stripping/depositing silver shell on Au nanodomes. The silver thickness determines the colour appearance and is controlled by the deposition time. Figure adapted from [56]. (B) Solid-state electrically-controlled plasmonic colour. Dynamic tuning of polarization-dependent gap plasmon resonators is demonstrated by lithiation/delithiation of electrochromic oxide WO_3 [59].

Stimulus-responsive materials make plasmonic colouration tunable and have been successfully demonstrated in various display applications [5, 43, 60, 61]. However, almost all these applications heavily rely on expensive nanofabrication techniques, not plausible for mass production and making scalable plasmonic colouration a worthwhile topic to explore.

2.3 Stimulus-responsive Materials

Stimulus-responsive materials describe materials with tunable properties adapting to external stimulus, including temperature, light, mechanical deformation, electrical and

magnetic field [62], *etc.* They have been used extensively for applications in active plasmonics field, especially for dynamic plasmonic colouration [60, 63]. Conjugated conductive polymers are one of the most popular stimulus-responsive materials applied in active plasmonics, due to their remarkable swift optical property change which can be reversibly controlled electrically and ease of processing at low cost [55].

2.3.1 Conjugated Conductive Polymer

Discovered in the late 1970s, conjugated conducting polymers have gained enormous attention from both academia and industry for their tremendous potential, especially in flexible electronics [64]. The most extensively studied and popularly used conducting polymers include polyaniline (PANI), polypyrrole (PPY), polythiophene (PTh) and their derivatives such as poly(3,4-ethylenedioxythiophene) (PEDOT) (Figure 2.12), which are produced by chemical or electrochemical oxidation of their resonance-stabilised aromatic monomers. They are easy to synthesise and are commercially available at industrial scale.

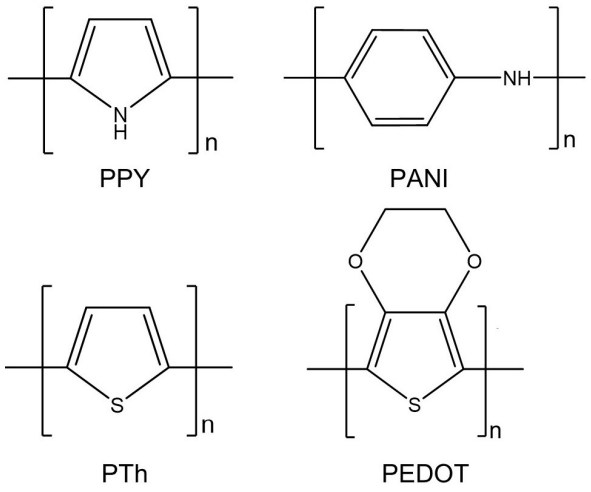

Fig. 2.12 Chemical structures of polypyrrole (PPY), polyaniline (PANI), polythiophene (PTh) and poly(3,4-ethylenedioxythiophene) (PEDOT).

Conductive polymers characteristically have conjugated backbones, generated by strong localised σ bonds and weaker overlapping π bonds. The electrons can move freely along the chains due to the delocalisation of the π bonds, leading to the conductivity (Figure 2.13 A).

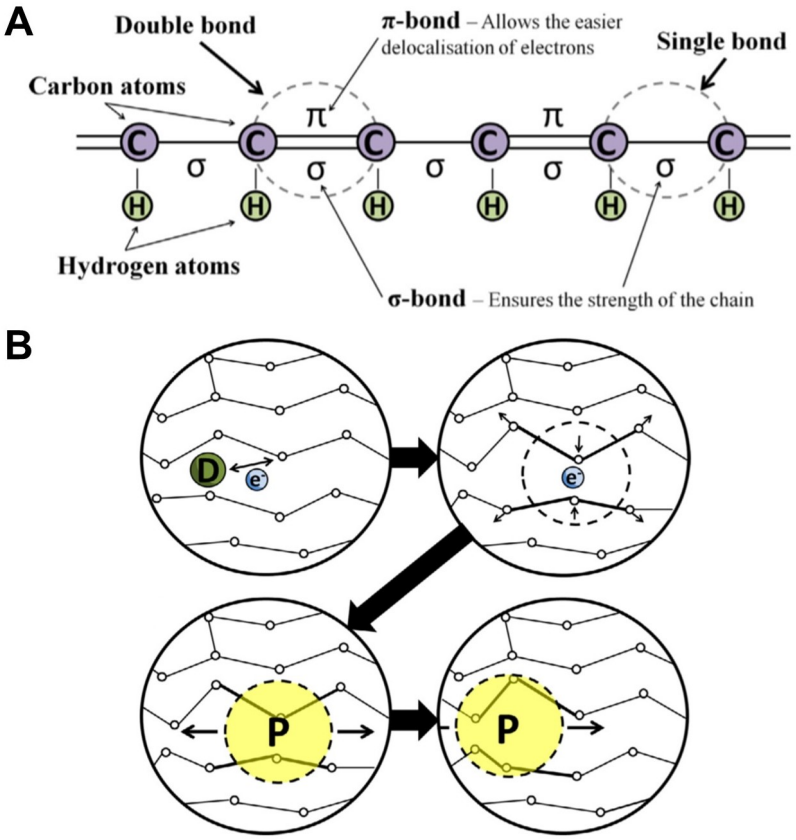

Fig. 2.13 Conjugated conductive polymer concepts. Schematics of (A) a simple conjugated backbone chain with alternating single and double bonds and (B) the formation of polaron (denoted as P) by adding an electron and stabilised by a dopant (denoted as D). Figures adapted form [65].

However, conjugated conductive polymers need a 'doping' process to be conductive (Figure 2.13 B). By either oxidation (p-doping) or reduction (n-doping), the neutral polymer chain becomes positively or negatively charged. This process introduces charge carriers in the form of polarons or bipolarons into the polymer chains (Figure 2.14 A). Polarons and bipolarons can be regarded as radical ions and di-cations/anions, respectively. In essential they are loosely-held localised lattice distortion surrounded by charges [66, 67].

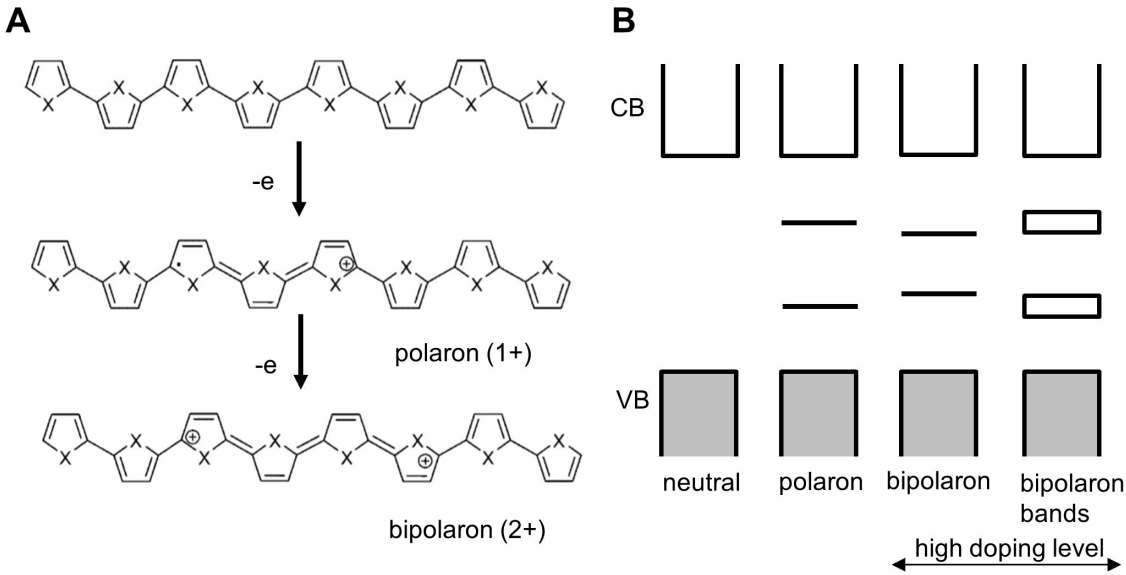

Fig. 2.14 Polaron model for conjugated conductive polymer. (A) The formation of the polaron and bipolaron by losing two electrons successively upon oxidation for PPY or PTh (PEDOT is similar) and (B) the resulted band structure. The change within the energy gap between the valance band (VB) and conduction band (CB) determines the electrical and optical properties of polymers. Figures adapted from [68].

Take PPY as an example (Figure 2.14). This is an insulator with neutral charge in the undoped state (the bandgap is approximately 3.16 eV [64]). Upon oxidation, a π electron is removed from the main chain, and a positive polaron (1+) forms with a local deformation of benzenoid-to-quinoid structure change, which results in two localised electronic states within the bandgap. The polymer can be further oxidised with another electron removed, forming a charged bipolaron (2+) with stronger benzenoid-to-quinoid deformation. As oxidation continues along the chain, two bipolaronic bands appear, and the bandgap is reduced to 1.4 eV (Figure 2.14 B) [64]. Counter-ions have to be introduced to balance the charges, so reversible insertion/extraction of ions through the polymer occurs simultaneously during redox reactions [55]. This means that the switching speed will be influenced by the ion diffusion speed [69, 70]. This model can also explain PTh or PEDOT properties in a similar way [71].

PANI is different as its protonation state also influences its properties. PANI has three oxidation states, termed leucoemeraldine (reduced, 0 state), emeraldine (half oxidised, 1+ state), and pernigraniline (fully oxidised, 2+ state) (Figure 2.15). Emeraldine or pernigraniline have a salt (protonated) or base form according to the pH level. Protonated emeraldine salt ($PANI^{1+}$) is produced directly by oxidative polymerisation

of aniline in acid solution and is conductive. The unpaired electrons on imine nitrogens form the polarons, which redistribute along the PANI chains and are responsible for the conductivity. In contrast, its base form is not conducting, where the transition happens around pH 6-7 [72]. Similarly for pernigraniline ($PANI^{2+}$), pH below 2.5 is required for its protonation and conductivity [73]. The reduced form leucoemeraldine ($PANI^{0}$) is non-conducting as it possesses no charge carriers. PANI's sensitivity for proton concentration also makes it useful for pH sensing applications [74].

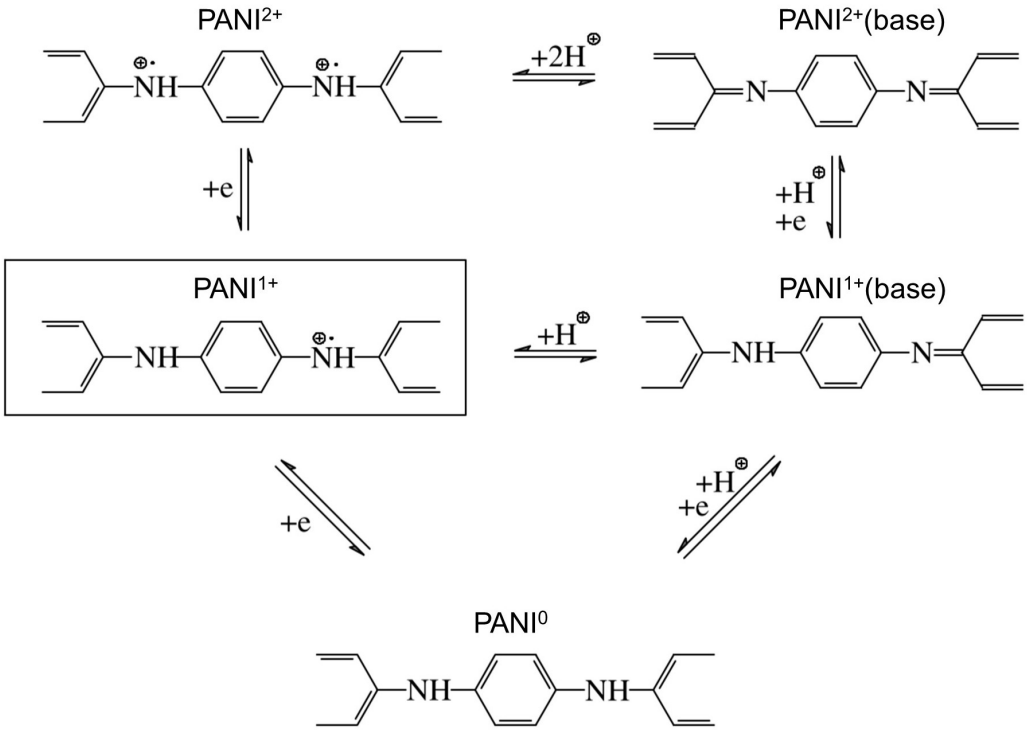

Fig. 2.15 Different PANI forms and their interconversions. Figure adapted from [72, 75].

Modification of electronic properties leads to the change of optical properties, so these materials are often electrochromic, and their colour can be tuned by controlling the doping/dedoping process or charge/redox state. The refractive index changes of PPY, PEDOT and PANI during redox are shown in Figure 2.16. The main changes happen at the longer wavelength region as the polymers approach oxidation, ascribed to the absorption modulation of subbands by polarons and bipolarons [55]. The metallic-like characteristic free-carrier absorption feature appears at high oxidation (doping) level when the bipolaron bands approach and merge with the valence and conduction bands [54]. For reduced (undoped) polymers, there are characteristic $\pi - \pi^*$ interband

transitions usually at the shorter wavelength region, determined by the intrinsic energy gap. PPY and PANI have $\pi - \pi^*$ energy gaps higher than 3 eV [64, 76], so < 400 nm and are not seen in the figure, while that of PEDOT can be seen around 500-600 nm as its energy gap is around 2 eV [54]. PANI presents a larger refractive index change in the visible region among these three, but tailored optical properties can be acquired by blending/mixing different conducting polymers or modifying their chemical structures [53, 77], providing rich possibilities to serve as active dielectric media and thus can be combined with plasmonic nanostructures to make novel functional devices.

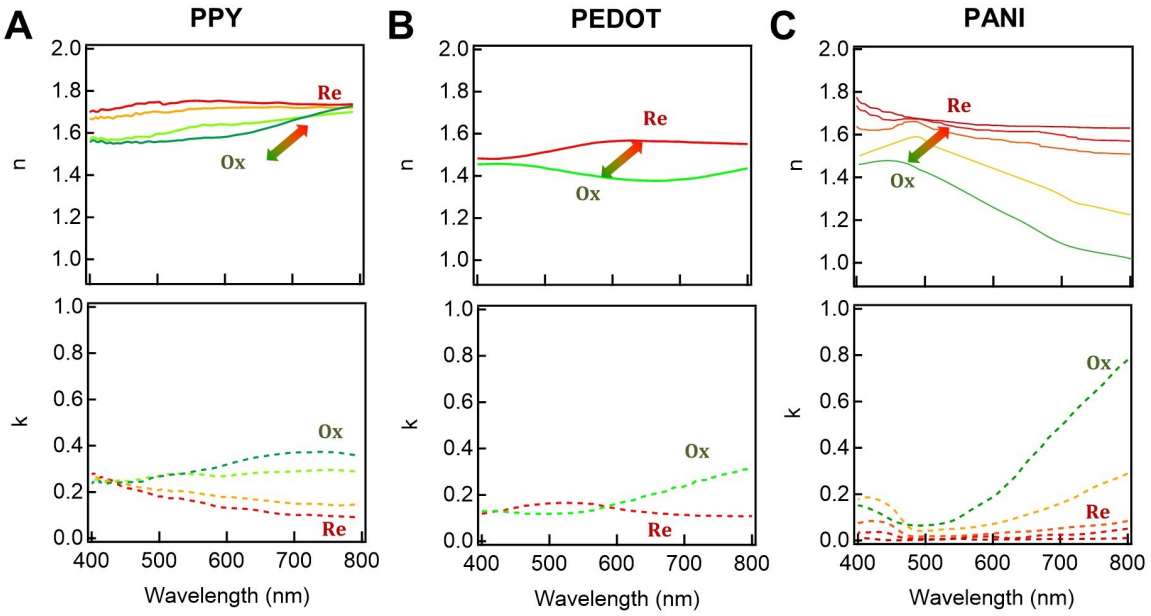

Fig. 2.16 Refractive index (n,κ) change of (A) PPY, (B) PEDOT and (C) PANI during redox. Re/Ox means reduction/oxidation. The refractive index data is from references [78], [79], [80], respectively.

2.4 Summary

The fundamentals of light interactions with metals are firstly introduced in this chapter. Plasmonic nanostructures allow for substantial field enhancement and tunable optical properties, offering an excellent platform for investigating light-matter interactions and making new functional optical devices. Plasmonic colouration is one of the key applications of plasmonics. Combined with stimuli-responsive materials, especially conjugated conductive polymers, dynamic plasmonic displays can be fabricated, holding

potential for display markets. In the last section, the unique electronic and optical properties of conjugated conductive polymers are summarized.

3. Experimental Methods

This chapter describes the main experimental methods used in the thesis. The first part addresses optical microscopies in detail, including bright-field/dark-field spectroscopy and Raman spectroscopy. The second part introduces the simulation method used, which helps to understand the optical response of plasmonic systems.

3.1 Optical Microscopies

3.1.1 Bright-Field and Dark-Field Microscopy

Optical microscopy provides the primary analytical tool to characterise the plasmonic nanostructures. In this work, a customised Olympus BX51 microscope is used (Figure 3.1), equipped with a broad-band halogen lamp (Philip 7023) as the white light source and a Lumenera Infinity 2 camera for real-time imaging. Light is collected by the microscope objective, and then guided by beam splitters to focus on a multi-mode optical fibre, which is coupled to a spectrometer for spectra acquisition (Ocean Optics QE65000, spectral range is around 400 to 900 nm). The physical size of the collection spot is set by the fibre core size and the objective magnification, approximately 1 μm in diameter for a 100× objective (Olympus LMPLanFL N-BD) with a 50 μm fibre core size. Samples are moved by a motorised three-axis translation stage (Prior II, minimum step size 100 nm). Lasers and Raman spectrometer can also be integrated into the system in a similar approach.

Optical imaging and spectroscopy can be done in both bright-field (BF) and dark-field (DF) configurations. In BF configuration (Figure 3.1), reflected and diffracted light is detected. The light illuminates at an angle θ_i and is collected with the same collection angle θ_c. The collection and illumination angle is determined by the numerical aperture

(NA) of the objective, defined as

$$NA = n \sin(\theta_c) \tag{3.1}$$

where n is the refractive index between the objective and the sample.

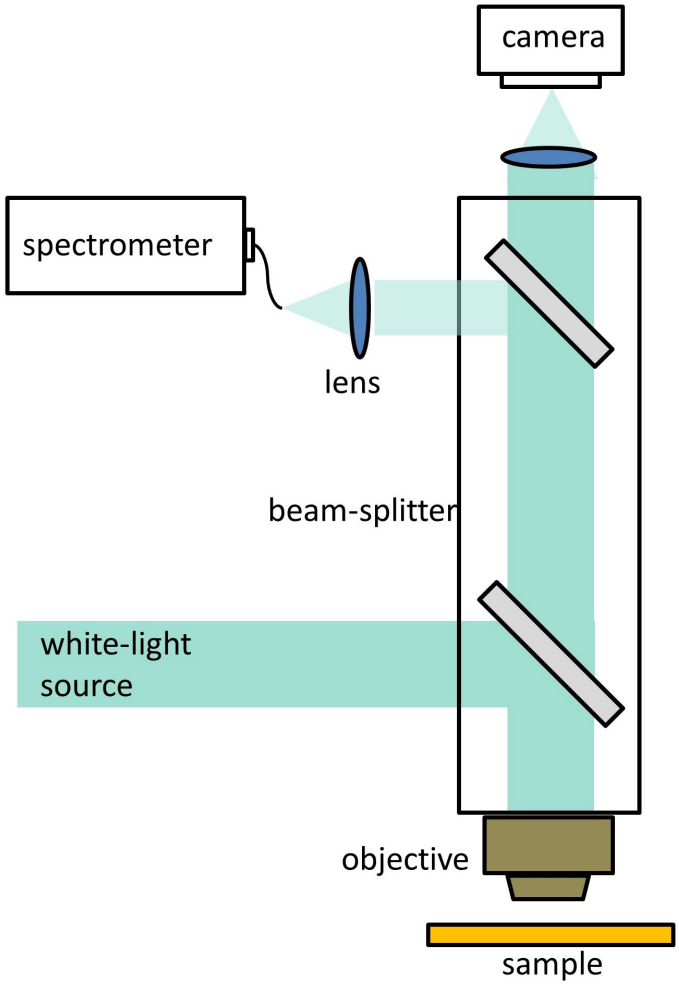

Fig. 3.1 Simplified optical diagram of bright-field spectroscopy.

NPoMs scatter light at the resonant frequencies. The strong reflection of the gold substrate needs to be blocked to enable the detection of the scattering signal, so the DF configuration needs to be used (Figure 3.2 A). An annular mirror couples a ring of light into the illumination path of the DF objective, which has a larger illumination angle θ_i than collection angle θ_c (Figure 3.2 B). The reflected light is blocked in this way, whereas the scattered light within the cone of solid angle $2\theta_c$ is collected.

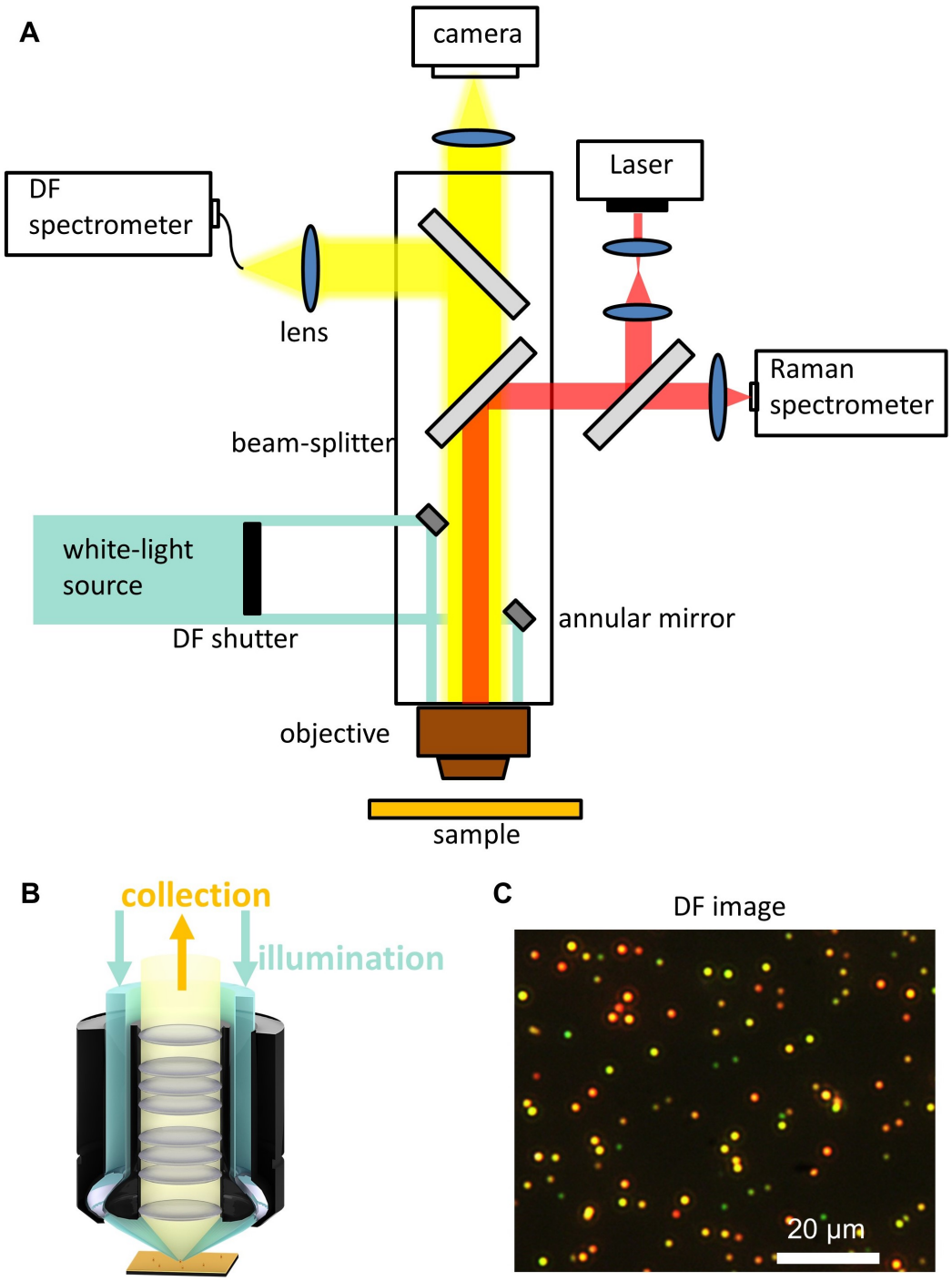

Fig. 3.2 Dark-field spectroscopy. (A) Simplified optical diagram of integrated dark-field and Raman spectroscopy. (B) Schematic of a dark-field objective. Light illuminates at a high angle, and only scattered light is collected. Figure adapted from [8]. (C) DF image of a Ag NPoM sample with various sizes/shapes, showing different scattering colours.

3.1.2 Raman Spectroscopy

Raman scattering was first experimentally demonstrated by Chandrasekhara V. Raman in 1928 [81], who was awarded the Nobel Prize. Raman spectroscopy provides a technique for identifying molecules using light.

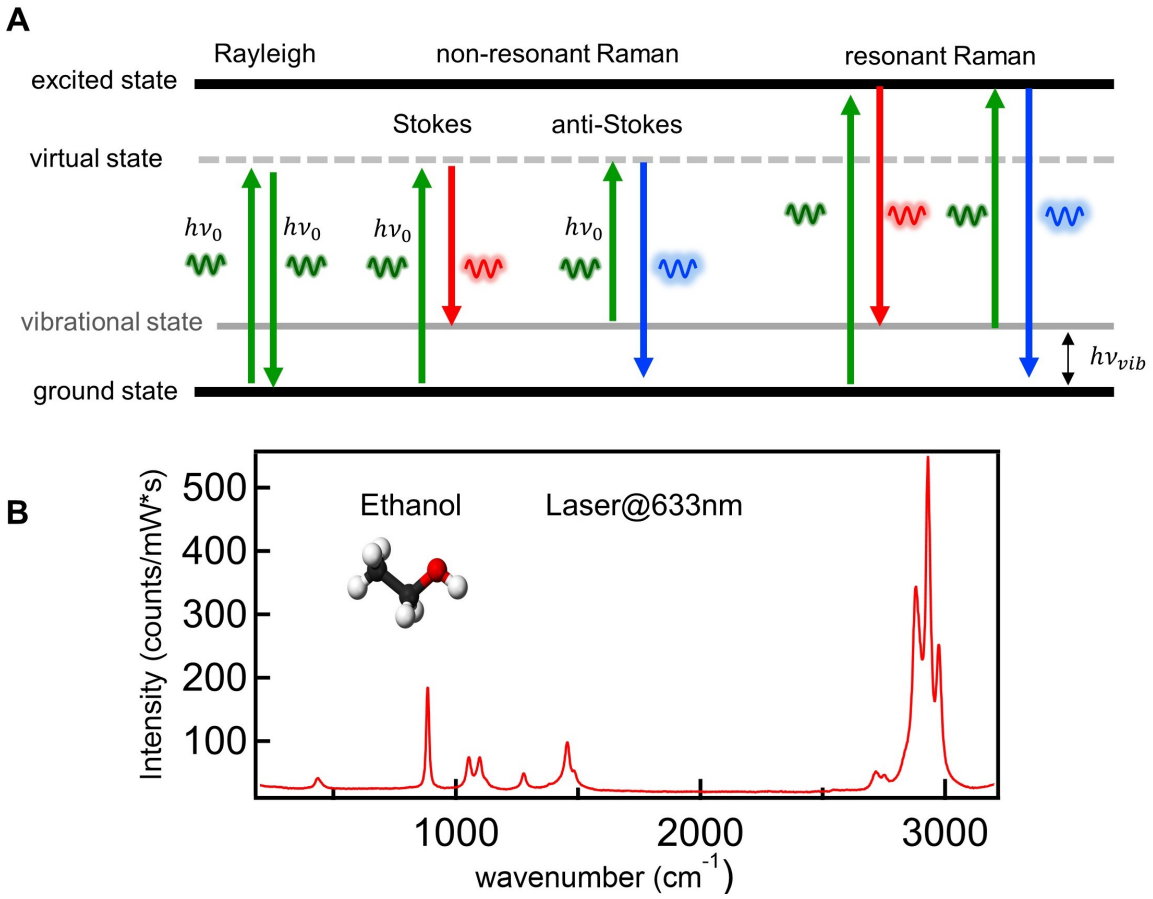

Fig. 3.3 Raman spectroscopy. (A) Energy level diagrams of Raman transitions. (B) Raman spectrum of ethanol.

The main molecular scattering processes are shown in Figure 3.3 A. After a photon of energy $h\upsilon_0$ is absorbed, the molecule is lifted into a higher energy state, and subsequently relaxes back into a lower energy state via re-emitting another photon. In most cases, the molecule re-emits photons with the same frequency $h\upsilon_0$. This elastic scattering process is denoted as Rayleigh scattering. However, a small number of molecules inelastically re-emit photons with an energy shift $h\upsilon_{vib}$, which is known as Raman scattering. Two cases are possible depending on if the final vibrational energy

is higher or lower than the initial one: if the scattered light is of lower frequency, the process is called Stokes scattering; if the scattered light is of higher frequency, the process is termed anti-Stokes scattering.

Generally, the energy shift is expressed in wavenumbers (Raman shift, cm^{-1}) $\frac{1}{\lambda_0} - \frac{1}{\lambda_{Raman}}$, where λ_0 is the incident light wavelength and λ_{Raman} is the emitted Raman light wavelength. As the Raman shift highly depends on the vibrational modes and chemical groups of the molecule, the Raman spectra can be used to generate the 'vibration fingerprints' of the molecule. An example Raman spectrum is shown in Figure 3.3 B for ethanol. However, only the vibrational modes that are Raman active can be measured, which means the polarisability of the mode needs to change during a vibration cycle [82].

For Raman scattering, the excited energy state is a short-lived virtual transition state and the population probability of this state is very low, making Raman scattering an inherently weak process. The Raman intensity can be evaluated from the Raman cross-section σ_{Raman}, calculated as the ratio between the scattered power of Raman photons and the intensity of the incident light, typically on the order of $\sim 10^{-27}$ $\mathrm{cm}^2/\mathrm{sr}$ [83, 84]. A typical technique to enhance Raman scattering is using plasmonic nanostructures, known as surface-enhanced Raman scattering (SERS) [85]. The electromagnetic enhancement g_{SERS}, obtained from the enhanced electric fields in plasmonic hotspots, can lead to an enhancement proportional to the fourth power of the incident field strength:

$$g_{SERS} \propto I_{inc} \times I_{Raman} \propto E_{inc}^2 \times E_{Raman}^2 \approx E_{inc}^4 \tag{3.2}$$

where I_{inc}, E_{inc}, I_{Raman}, E_{Raman} are the light intensities and field strengths of the incident light and Raman scattered light, respectively. This rule of thumb is valid when a sufficient overlap exists between the plasmon resonance and Raman excitation wavelength (Figure 3.4). The enhancement could reach up to 10 orders of magnitude, but in practice, 6-9 orders of magnitudes are commonly achieved [82, 86].

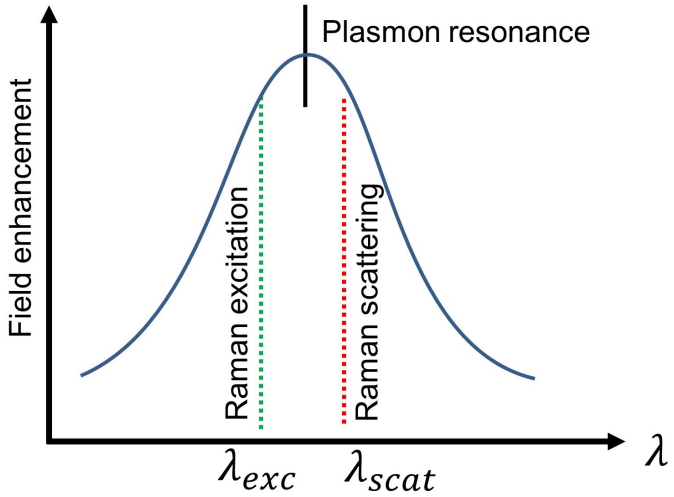

Fig. 3.4 Electromagnetic SERS enhancement. Optimal spectral configuration is achieved when excitation as well as the Raman shift overlaps with a plasmonic resonance.

The Raman scattering intensity can also be dramatically enhanced when $h\upsilon_0$ matches the energy gap between initial and a vibrational state in a higher real electronic band (Figure 3.3 A). The transition probability is strongly increased and up to several orders of magnitude higher Raman scattering intensity can be observed [87], which is referred to as resonant Raman scattering [88]. The combination of resonant Raman scattering and plasmonic enhancement can lead to surprisingly intense spectra, providing rich information of detected molecules.

The same BX51 microscope is used for the SERS spectra measurement (Figure 3.2), integrated with a 633 nm continuous-wave diode laser (MatchBox series, Integrated Optics) for excitation. The spectra are recorded by an Andor camera coupled to a Triax 550 spectrometer.

3.2 Numerical Simulations

Numerical simulations offer a valuable toolbox to provide insights in optical response of plasmonic nanostructures and disentangle the different contributions to the spectra, especially for those perhaps not easily accessible experimentally. Commercial Finite Difference Time Domain (FDTD) software (Lumerical Solutions) are mainly used for modelling in this thesis. In FDTD, structures are discretised into small elements, and time-dependent Maxwell's equations are solved numerically for each element. It is advantageous in simulating the full spectral response of structures with broadband

incident waves but can be computationally expensive for structures with sub-nanometre fine features.

Here, FDTD is mainly used to calculate the scattering and field enhancement of the NPoM structures. Plasmonic nanoparticles are modelled as specific shapes (usually nanospheres) on top of a gold rectangular layer (typically 100 nm thick) with a gap (Figure 3.5). The gap sizes are set to match the corresponding experiments. The dielectric properties of materials are taken from literature (*e.g.* gold from Johnson and Christy [7]). The light is illuminated as a broadband plane wave with required polarisation and incident angle. The refractive index of the surrounding environment can be set as air ($n = 1$) or as required.

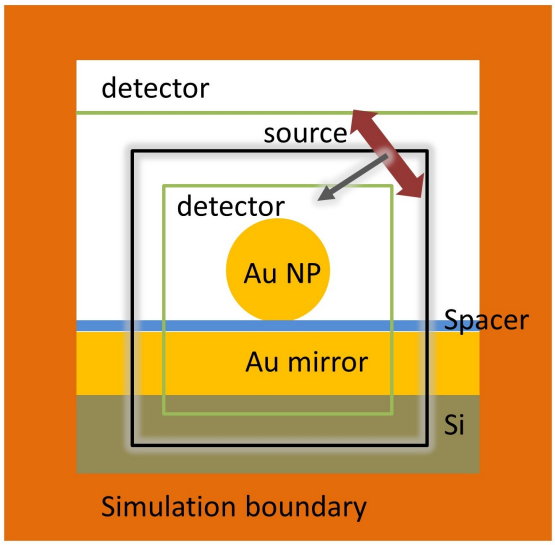

Fig. 3.5 Schematic of Lumerical FDTD simulation setup (not to scale). Au NP is sitting on Au mirror with a spacer.

3.3 Summary

This chapter introduces the experimental methods for characterising and simulating plasmonic nanostructures. Experimental set-ups including bright-field, dark-field and Raman spectroscopy are demonstrated, together with the FDTD simulation details.

4. Electrochromic Nanoparticle on Mirror (*e*NPoM)

This chapter introduces the basic structure investigated throughout this thesis - the Electrochromic Nanoparticle on Mirror (*e*NPoM), which is the functional unit of the nano-pixel. The structure is fabricated by positioning a conductive polymer (here polyaniline, PANI) coated plasmonic nanoparticle (here gold nanoparticles, Au NPs) onto a metal mirror. The scheme works by switching the charge state of the entire polymer shell, thus rapidly shifting the resonant scattering colour of the *e*NPoM across >100 nm wavelength ranges. Remarkably, this active nano-pixel shows vivid colour dynamics and can achieve commercial video rates, not possible with any existing plasmonic colour system.

First, the concept of *e*NPoM is introduced, with FDTD simulations to show the plausibility. Then, the fabrication and the reversible optical switchings of single *e*NPoMs are demonstrated, followed by the comparison of different gap thickness. Finally, the correlation of electrical and optical switching dynamics is discussed, with an evaluation of the temporal response ability.[1]

4.1 Concept of *e*NPoM

As described in section 2.1.2, by changing the refractive index of the medium surrounding the plasmonic nanomaterial, the local surface plasmon resonance (LSPR) peak position can be shifted [43], leading to the change of the colour appearance. The

[1] Experimental work was undertaken in collaboration with Dr Hyeon-Ho Jeong. Part of this chapter has been published in Ref. [89].

corresponding colour tuning can be estimated from the LSPR sensitivity [90],

$$S_n = \frac{\Delta\lambda^*}{\Delta n} = \frac{-2\chi n}{(d\varepsilon_m/d\lambda)_{\lambda^*}} \tag{4.1}$$

where λ^* is the resonant wavelength, χ is a shape factor of the metal nanoparticle ($\chi = 2$ for spheres), ε_m is the dielectric permittivity of the metal nanoparticle, and n is the refractive index of the medium surrounding the nanoparticle. Ideally, in order to achieve colour dynamics in the visible region (requiring $\Delta\lambda^*$ to tune over the whole visible spectrum), Δn should be large while ensuring $n \sim 1$ to keep the LSPR resonance in the middle of the visible region.

A rational approach to get rid of nanolithographies is to use plasmonic nanoparticles directly for colourations. A straightforward way to achieve tunable colourations for nanoparticles is to incorporate plasmonic nanoparticles into active surroundings that change their optical properties Δn depending on external stimuli [63]. One promising set of candidates are phase-change inorganic materials that possess large Δn [91], but since most have $n > 2$ their LSPR resonances are in the near infrared (NIR) and thus inappropriate for plasmonic colour applications. In contrast, responsive polymers offer LSPR modes in the visible as typically $n < 1.7$ [92] but show weak tuning ($\Delta n < 1$). Typical strategies employed to achieve full-colour dynamics have thus combined responsive polymers with increased shape factors of the nanoparticles ($\chi > 2$) to increase S_n (Eq. 4.1). Elongated particles such as nanorods and bipyramids have higher χ, indeed yielding higher $\Delta\lambda^*$ [93]. However, such systems not only require large effective volumes (reducing the resolution), but also develop strong polarization-dependent resonances tuned beyond the visible regime into the NIR.

Here I instead utilize electrochromic nanoparticle-on-mirror constructs (*e*NPoMs) composed of a Au NP encapsulated in a continuous PANI shell sitting just above a metallic mirror (Figure 4.1). This NPoM geometry behaves similarly to a dimer pair of near-touching plasmonic nanoparticles, giving rise to strong optical field coupling in the gap, known as a 'hot spot' (Figure 4.2 B, C) [94]. This hot-spot leads to a strong additional coupled resonance (here mode *c*), together with a transverse mode around 550 nm supported by the Au NP alone [14]. This coupled resonance tunes when the surrounding optical environment changes while the transverse mode is only weakly affected. Furthermore, the coupled mode is insensitive to incident light polarization and angle, making this ideal for an extremely localized nano-pixel [95]. Here this coupled resonance is tuned by changing the redox state of the ultrasmall volume of PANI shell surrounding each nanoparticle ($\sim 3 \times 10^{-4}\mu\text{m}^3$/NP), altering the PANI

molecular polarizability and thus its effective refractive index as much as $\Delta n = 0.6$ during redox [96].

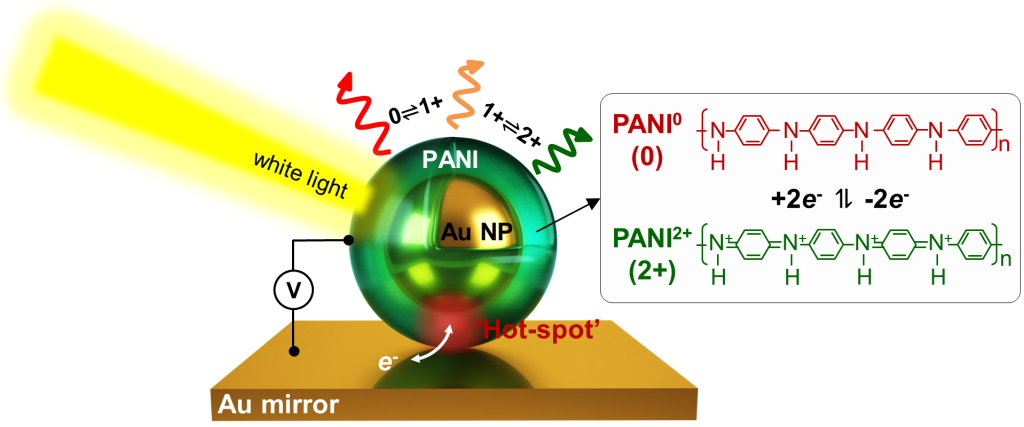

Fig. 4.1 Schematic of an *e*NPoM, which changes colour as a function of redox state of the polyaniline (PANI) shell surrounding each Au NP on Au mirror substrate. The right panel shows redox reaction of PANI in the gap ($PANI^0$: fully reduced, $PANI^{1+}$: half oxidized, $PANI^{2+}$: fully oxidized).

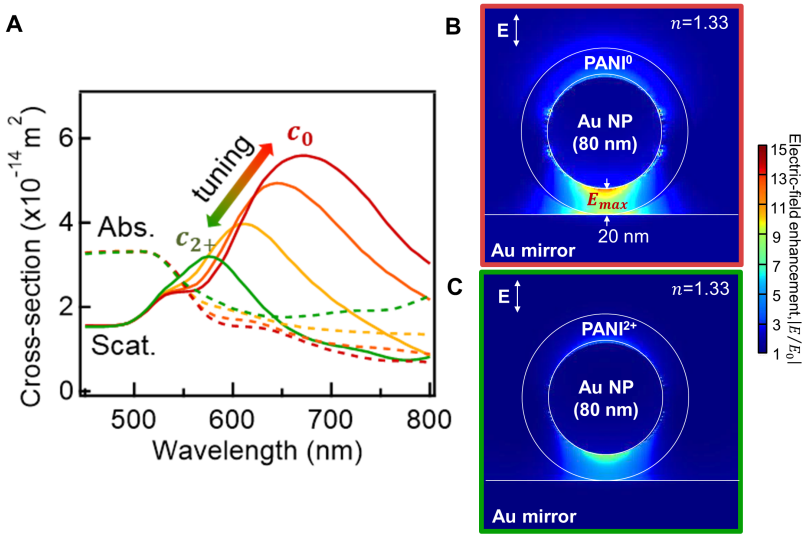

Fig. 4.2 FDTD Simulation results of *e*NPoM. (A) Simulated optical scattering (solid lines) and absorption spectra (dashed lines) for different redox states of the PANI shell (red to green: $PANI^0$ to $PANI^{2+}$). (B-C) Optical near-field enhancement of the *e*NPoM for reduced ($PANI^0$) and oxidised ($PANI^{2+}$) state of PANI shell, showing 'hot spot' in the gap.

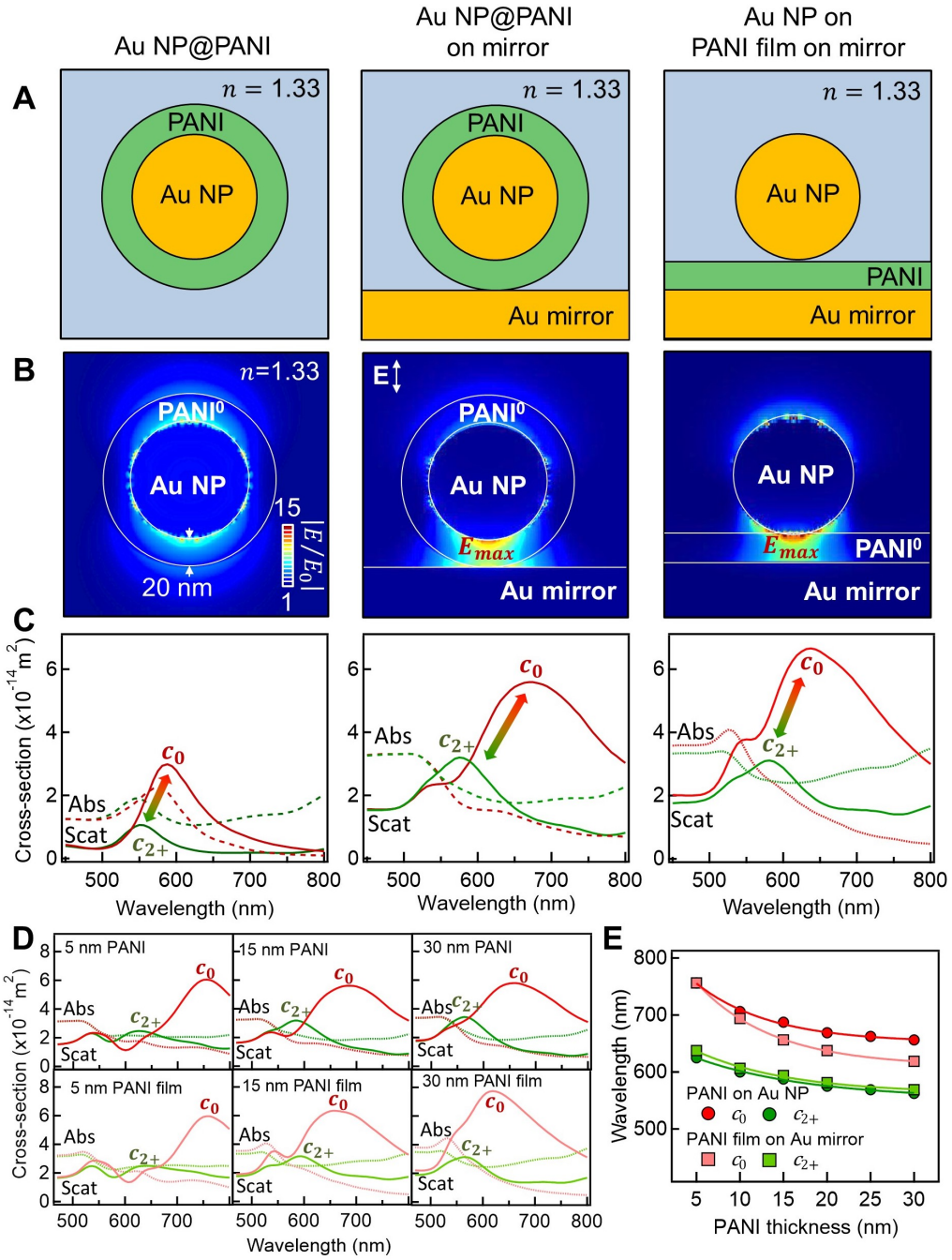

Fig. 4.3 Comparison of different configurations from simulations. (A) Schematics and (B) optical near-field enhancements of Au NPs coated with a 20 nm PANI shell layer (left panel) and two different *e*NPoM geometries (middle: PANI shell surrounding Au NP, right: flat PANI layer on Au mirror). (C) Corresponding simulated optical scattering (solid lines) and absorption spectra (dotted lines) with reduced (red) and oxidized (green) PANI. (D) Simulated optical scattering (solid lines) and absorption spectra (dotted lines) of the two *e*NPoMs *vs* wavelength for different PANI thicknesses (5 nm to 30 nm from left to right). (E) Corresponding coupled plasmon mode peaks as a function of PANI thickness.

The electromagnetic response of the *e*NPoM is simulated by finite-difference time-domain (FDTD) calculation software. An 80 nm diameter Au nanosphere surrounded with a 20 nm thick spherical PANI shell is placed on top of a 100 nm thick gold rectangular mirror. The light is illuminated as a broadband plane wave polarized perpendicular to and propagating along the mirror, to effectively excite the coupled plasmonic resonance. The optical properties of gold and PANI are taken from literature [7, 96]. To simplify the computation, the refractive index of the whole surrounding environment is set to $n = 1.33$ assuming water. The simulations (Figure 4.2 A) suggest that full redox of the PANI in the *e*NPoM can result in visible scattering wavelength shifts of >100 nm, 300% larger than those supported by nanoparticles alone (Figure 4.3) [93]. In the reduced state of $PANI^0$, the *e*NPoM coupled resonance is at $c_0 = 675$ nm, which would blue-shift to $c_{2+} = 575$ nm when oxidized to $PANI^{2+}$. A helpful feature here is that *e*NPoMs with relatively large gaps (20 nm thick PANI layer here) still present useful colour properties, compared to previous NPoMs with ultrathin dielectric spacers on a mirror [14, 95, 97]. Contributions from the enhanced optical fields on top of each *e*NPoM double the $\Delta\lambda^*$ compared to NPoMs depending only on changes in their gap (Figure 4.3, right column). Scattering supported by the optimal *e*NPoM predicts a 100 nm colour range with 43% switching contrast at resonance (Figure 4.2), as well as $> 400\%$ stronger scattering than absorption at resonance. This therefore promises a switchable colour appearance with low optical loss as well as high spatial definition, confirmed in the experiments on single nano-pixel devices (details in following sections).

4.2 Fabrication of *e*NPoM

Fabrication consists of two bottom-up steps:

(1) PANI coating around colloidal Au NPs in solution:

The colloidal Au NPs are encapsulated by a continuous thin PANI shell using surfactant-assisted chemical oxidative polymerisation as previously reported (Figure 4.4) [93, 98]. 1.6 mL of a citrate-stabilised colloidal solution of 80 nm Au NPs (from BBI Solutions) is concentrated and mixed with a mixture of aniline (2 mM, 0.6 mL) and sodium dodecyl sulfate (SDS, 40 mM, 0.12 mL). Due to electrostatic forces, the aniline coats the entire surface of the Au NPs, acting as a seed layer for further polymer growth (Figure 4.4 A). Then, 0.6 mL of 2 mM ammonium persulfate (APS) in 10 mM hydrochloric acid (HCl) is added into the solution. This leads to polymerisation of the monomers (Figure 4.4 B). For the complete polymerisation, the solution is incubated at room temperature

overnight, and then washed and re-dispersed in 4 mM SDS solution afterwards. The thickness of the PANI layer can be readily controlled by adjusting the amount of monomer in each coating procedure or by repeating the whole process. These core-shell nanoparticle constructs constitute the key nano building block controlling the optical resonance and its electron dynamics for redox chemistry. The shell thickness defines the critical gap spacing to the underlying mirror while also spacing wide enough between the neighbouring Au NPs, reducing their optical coupling and inhibiting their aggregation.

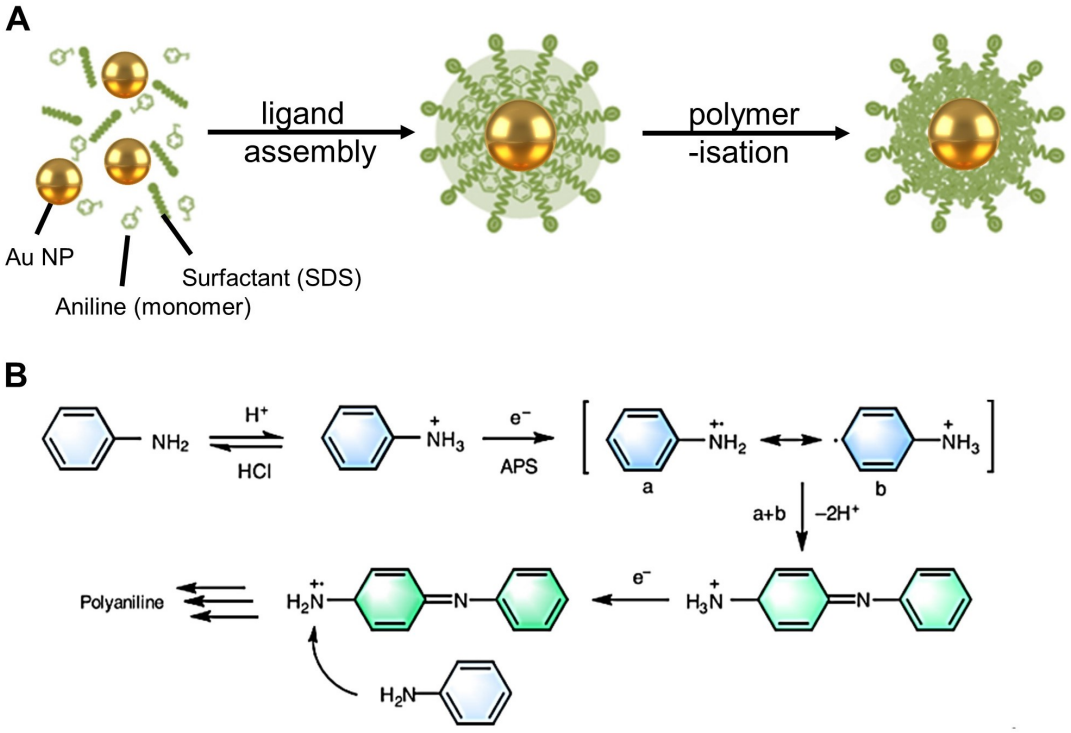

Fig. 4.4 PANI coating around colloidal Au NPs. (A) Illustration of surfactant-assisted chemical oxidative polymerisation. Figure adapted from [99]. (B) PANI polymerisation process. Figure adapted from [100].

(2) Preparation of *e*NPoM:

The electrochromic nanoparticles can simply be drop-cast onto planar Au substrates, resulting in randomly-distributed *e*NPoMs but with extremely precise gap sizes. Planar Au substrates are made by a template-stripping method, which provides atomically smooth gold layers [22, 101]. Briefly, 100-nm-thick Au is evaporated onto a silicon wafer at a growth rate of 0.1 nm/s without any adhesion layer using an e-beam evaporator (Lesker LEV). After this, small pieces (*ca.* 1 cm^2) of the bare Si wafer are glued on

with epoxy (*ca.* 3 μL, Epo-Tek 377). The epoxy is cured at 150 °C for 2 hours and then slowly cooled down to room temperature in 10 °C/h to avoid heat-induced stress. The pieces are peeled off together with the Au film prior to use. This method also functions as an ideal way to store clean Au films for months before the stripping off process.

4.3 Optical Switching of Single *e*NPoMs

Electrochemical control is achieved by a custom-built three-electrode electrochemical cell (Figure 4.5). The Au mirror substrate of the *e*NPoM is used as a working electrode [102]. A stack of square double-sided tape with the centres removed is adhered on a clean glass coverslip to create a fluid chamber. Half of the sample is sandwiched between two coverslips, and the other half is electrically connected to a potentiostat (CompactStat, Ivium Technologies). A Ag/AgCl reference electrode (Green-leaf Scientific) and Pt counter electrode (Alfa Aesar) are inserted into the electrochemical cell, and the chamber is filled with the electrolyte solution (0.5 M sodium chloride, NaCl in 10 mM HCl). The electrochemical cell is integrated with dark-field (DF) scattering spectroscopy, optimized to track both optical and electrical dynamics simultaneously.

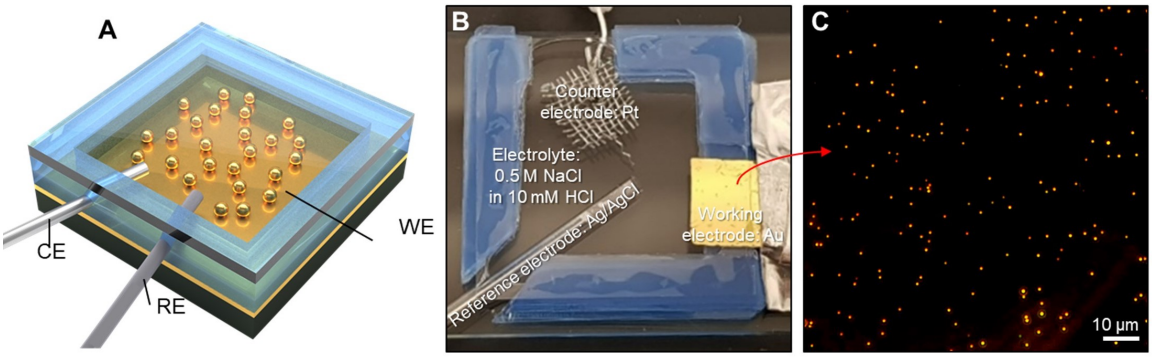

Fig. 4.5 Electrochemical cell. (A) Schematic of electrochemical cell used. The reference electrode (RE) is Ag/AgCl, the counter electrode (CE) is Pt, and Au layer is working electrode (WE). (B) Image of electrochemical cell with *e*NPoMs on mirror. (C) Large-area DF scattering image of sparse *e*NPoMs.

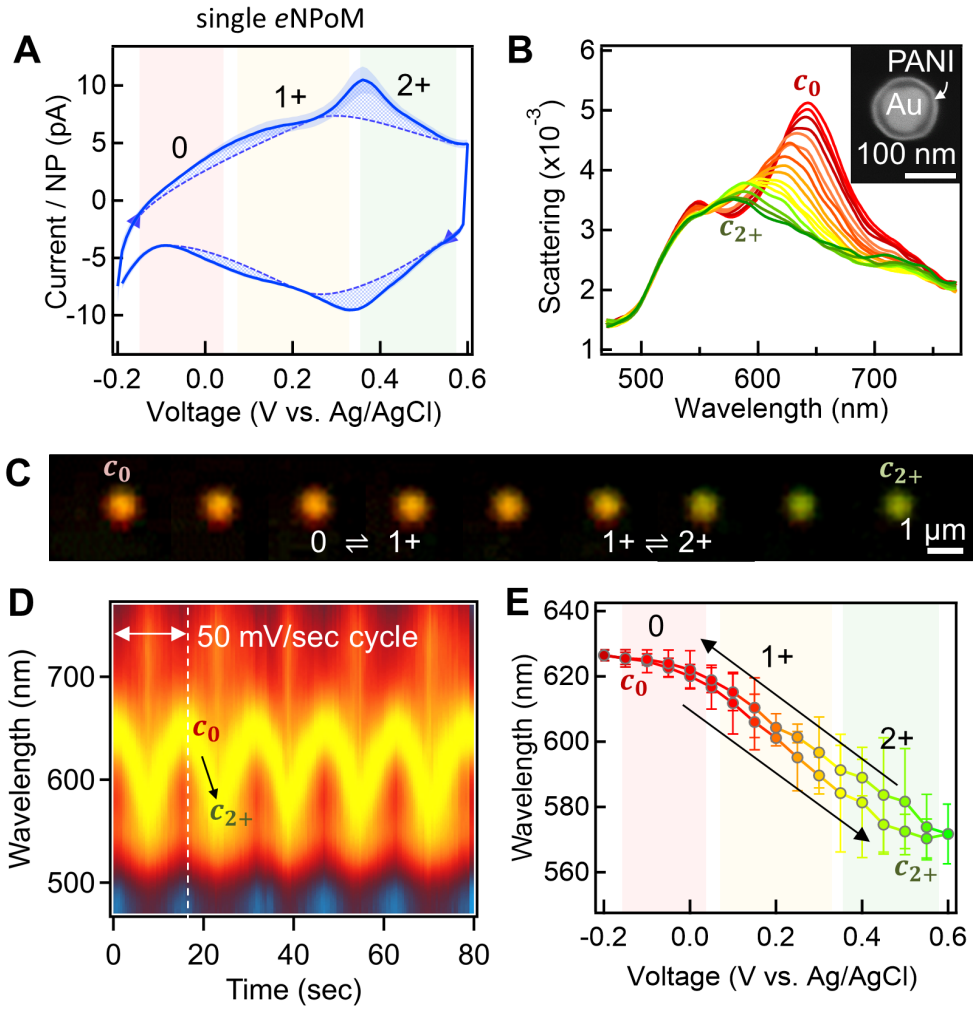

Fig. 4.6 Electrically-driven optical switching of single *e*NPoMs. (A) Cyclic voltammetry (CV) of *e*NPoMs, with current calibrated per *e*NPoM (around 5×10^7 *e*NPoMs are measured). (0: $PANI^0$, 1+: $PANI^{1+}$, 2+: $PANI^{2+}$, dashed background curve highlights redox peaks). (B) Dark-field (DF) scattering spectra of single *e*NPoM *vs* voltage applied as in (A) (c_0: $PANI^0$, c_{2+}: $PANI^{2+}$). Inset shows SEM image of a representative *e*NPoM (80 nm Au NP coated with 20 nm PANI shell on Au substrate). (C) Experimental DF scattering images of a single *e*NPoM nano-pixel for different redox states of the PANI shell (left to right: $PANI^0$ to $PANI^{2+}$). (D) Time scan of normalized DF scattering spectra from a single *e*NPoM for 5 cycles of ramped voltage -0.2 ↔ 0.6V with scan rate 50 mV/sec. (E) Reversible switching of coupled plasmon mode *vs* applied voltage.

The redox state of the PANI shells is controlled by sweeping the voltage from -0.2 to 0.6 V (*vs* Ag/AgCl) with a scan rate of 50 mV/sec. Cyclic voltammetry (CV) curves averaged over 90 cycles (Figure 4.6 A) show two sets of oxidized (upper) and

reduced peaks (lower) from the three different redox forms of PANI ($PANI^0$: fully reduced, $PANI^{1+}$: half oxidized, $PANI^{2+}$: fully oxidized). These *e*NPoMs are thus fully oxidized and reduced within only $\Delta V < 1$ V potential range. Simultaneously, DF scattering spectra of a single *e*NPoM are measured (Figure 4.6 B, Figure 4.6 C shows corresponding DF images). Application of negative potential causes the reduction of the PANI shell ($PANI^0$), which gives rise to the scattering peak at $c_0 = 642$ nm. Reversing the potential clearly reveals the resonance shift to $c_{2+} = 578$ nm, with $\Delta\lambda^* = 64$ nm consistent with our numerical simulations (Figure 4.2 A). Further observations of the DF scattering spectra while undergoing CV cycling shows highly stable and reversible optical switching (Figure 4.6 D) with fully reproducible dynamics (Figure 4.6 E). The optical dynamics of each *e*NPoM are found to be identical under the same conditions (Figure 4.7), a crucial basis for large-scale uniform colour-switching metafilms based on this concept (see next chapter).

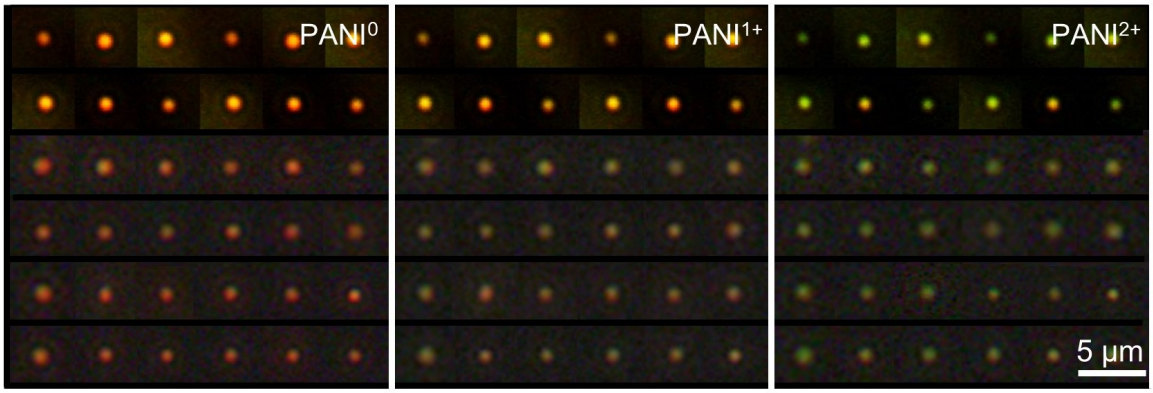

Fig. 4.7 DF scattering images of many *e*NPoMs at $PANI^0$, $PANI^{1+}$, and $PANI^{2+}$ state (left to right), showing identical colour dynamics for different *e*NPoMs.

4.4 *e*NPoMs with Varying Gaps

To examine how *e*NPoM colour switching is sensitive to structural parameters, I fabricate a series of *e*NPoMs with various gaps, set by the thicknesses of the PANI shell coated onto each Au NP. This is increased from 10 to 20 nm thickness with nanometer accuracy by controlling the monomer concentration used in the polymerisation process. The diameters are cross-checked (Figure 4.8) by scanning electron microscopy (SEM, accelerating voltage 10 kV, LEO 1530VP, Zeiss) and dynamic light scattering (DLS, Zetasizer Nano ZS, Malvern).

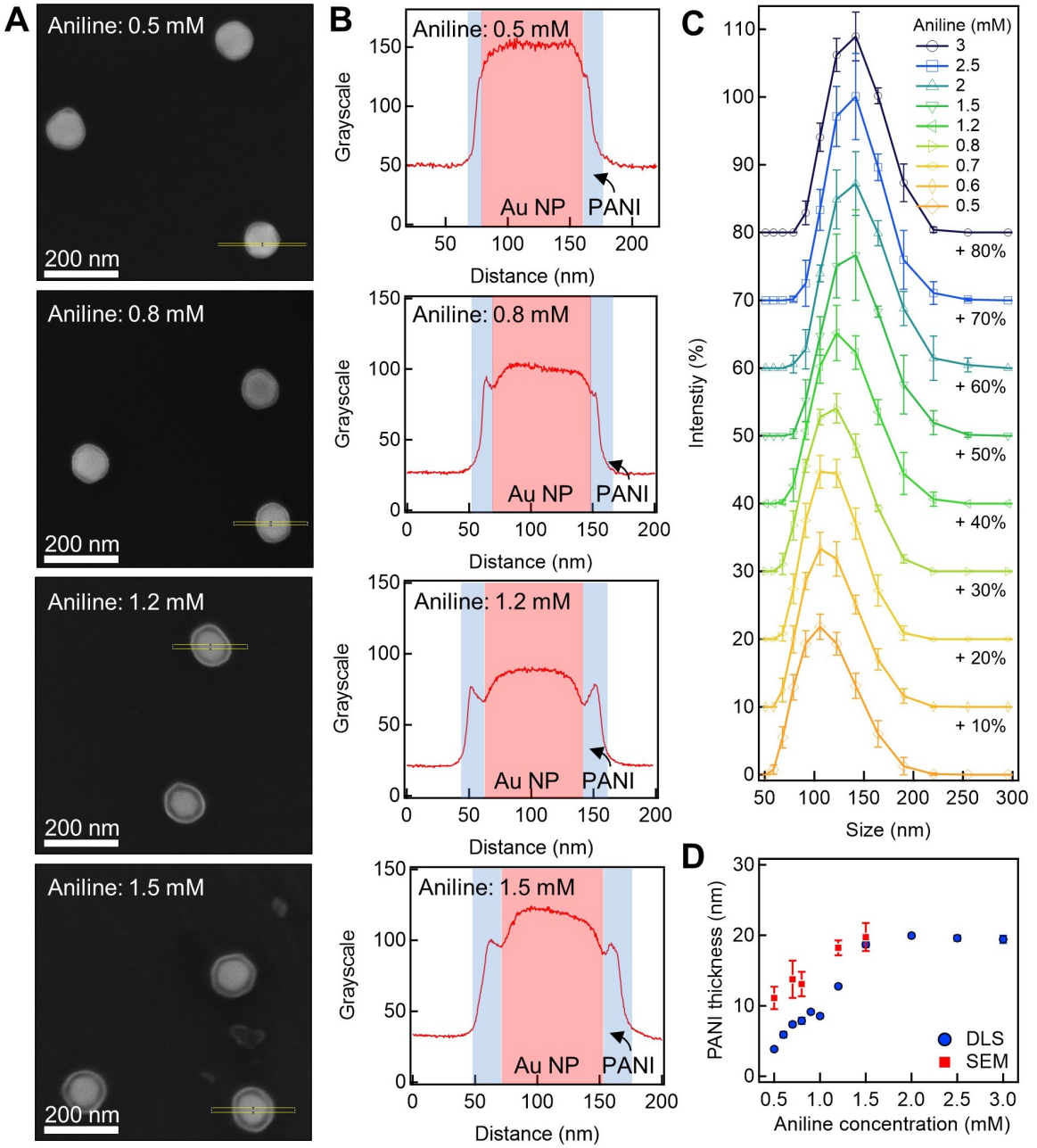

Fig. 4.8 PANI coating on Au NPs with thickness control. (A) Scanning electron microscope (SEM) images of 80 nm Au NPs coated with different PANI thickness. (B) Corresponding cross-sections and (C) dynamic light scattering (DLS) spectra, showing increasing hydrodynamic diameter of the NPs for increasing monomer concentration in the coating process. (D) PANI thickness measured by SEM (red squares) and DLS (blue circles) as a function of aniline monomer concentration.

I then fabricate *e*NPoM nano-pixels from four different PANI thicknesses of 11, 13, 18, and 20 nm (Figure 4.9 A) and evaluate their electrical (Figure 4.9 B) and optical dynamics (Figure 4.9 D, E). The spectral tuning is highly reversible and reproducible for each PANI thickness.

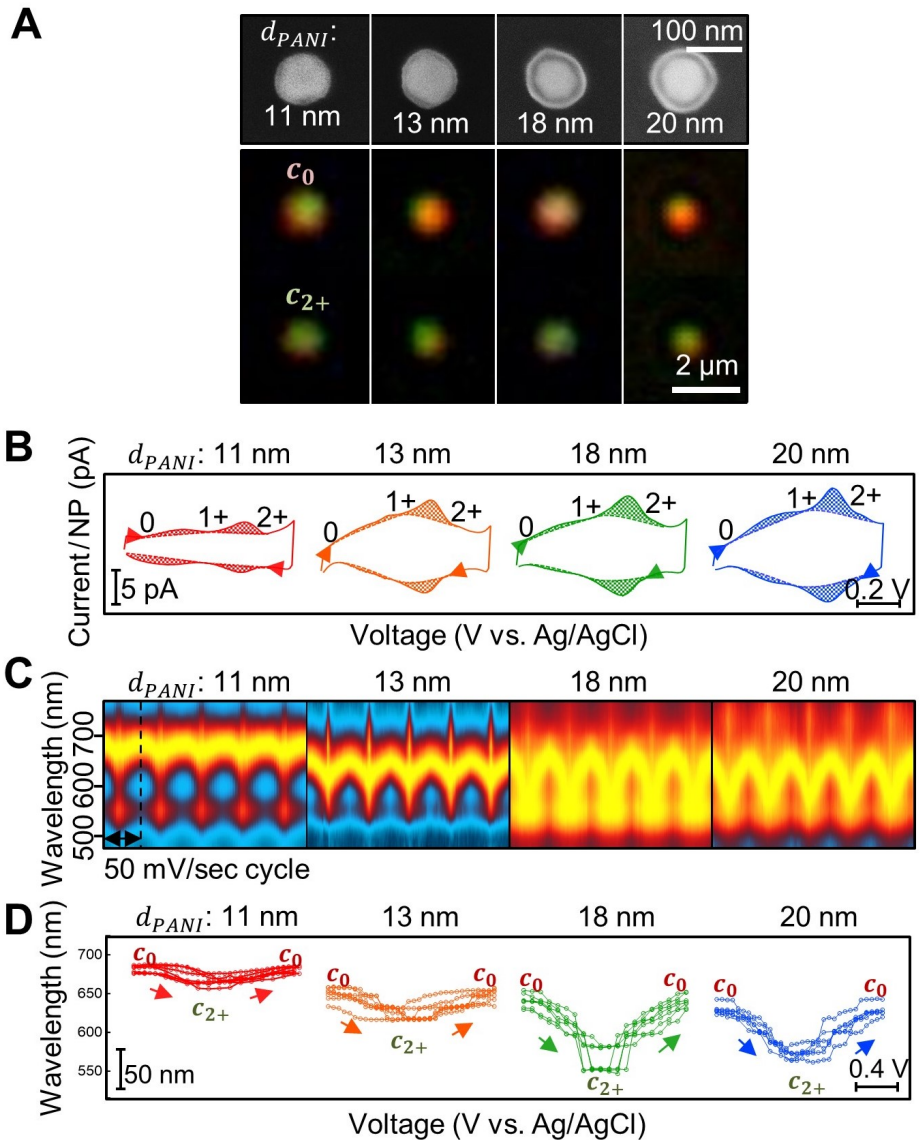

Fig. 4.9 *e*NPoMs with varying gaps. (A) Top panel shows SEM images of Au NPs coated with different thickness of surrounding PANI shell layer (11, 13, 18, and 20 nm from left to right). Bottom panel shows their corresponding DF images (top: $PANI^0$, bottom: $PANI^{2+}$). (B) CV curves of four different *e*NPoMs composed of 11 (red), 13 (orange), 18 (green), and 20 nm PANI shells (blue) *vs* applied voltage (from left to right). (C) Dynamic response in DF scattering of each NPoM nano-pixel *vs* gap size and (D) corresponding optical tuning range *vs* applied voltage.

Both simulated and experimental results for the spectral tuning as a function of the PANI shell thickness show characteristic reversible blue-shifts (Figure 4.10 A) and ∼50% intensity decay (Figure 4.10 B) upon oxidation. In theory, the resonant wavelength and the range of its spectral tuning both increase for smaller gaps (shells). However, the experimental results show that thinner PANI shells result in a smaller colour range upon redox cycling, which also can be seen in the associated colour gamut plots (Figure 4.10 C).

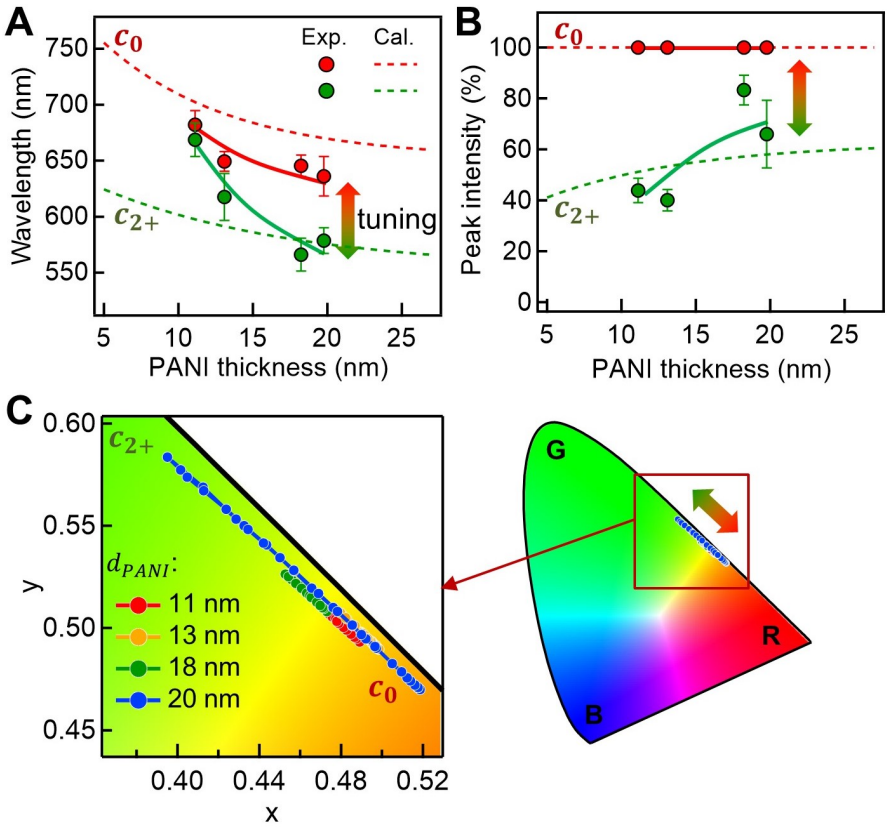

Fig. 4.10 Colour dynamics of *e*NPoMs with varying gaps. Simulated and experimental dynamic response in DF scattering of each NPoM nano-pixel *vs* gap size in (A) spectral tuning range and (B) peak intensity change. (C) Associated colour gamut plots (CIE 1931 chromaticity).

This may be due to a number of additional geometrical factors not included in the simulations (which are extremely sensitive to the nanostructure) including:

(i) imperfect spherical shapes and sizes of the synthesized Au NPs [25],

(ii) differences in optical properties of PANI of different thickness from additional effects of their ligands [98] and metal proximity,

(iii) non-uniform coatings of thinner PANI shells (<15 nm, Figure 4.9 A),

(iv) the ∼ 30% PANI thickness change during redox [96],

(v) possible non-uniform redox of PANI molecules within the gap, limiting the change of effective refractive index and thus the colour dynamic range (Figure 4.11).

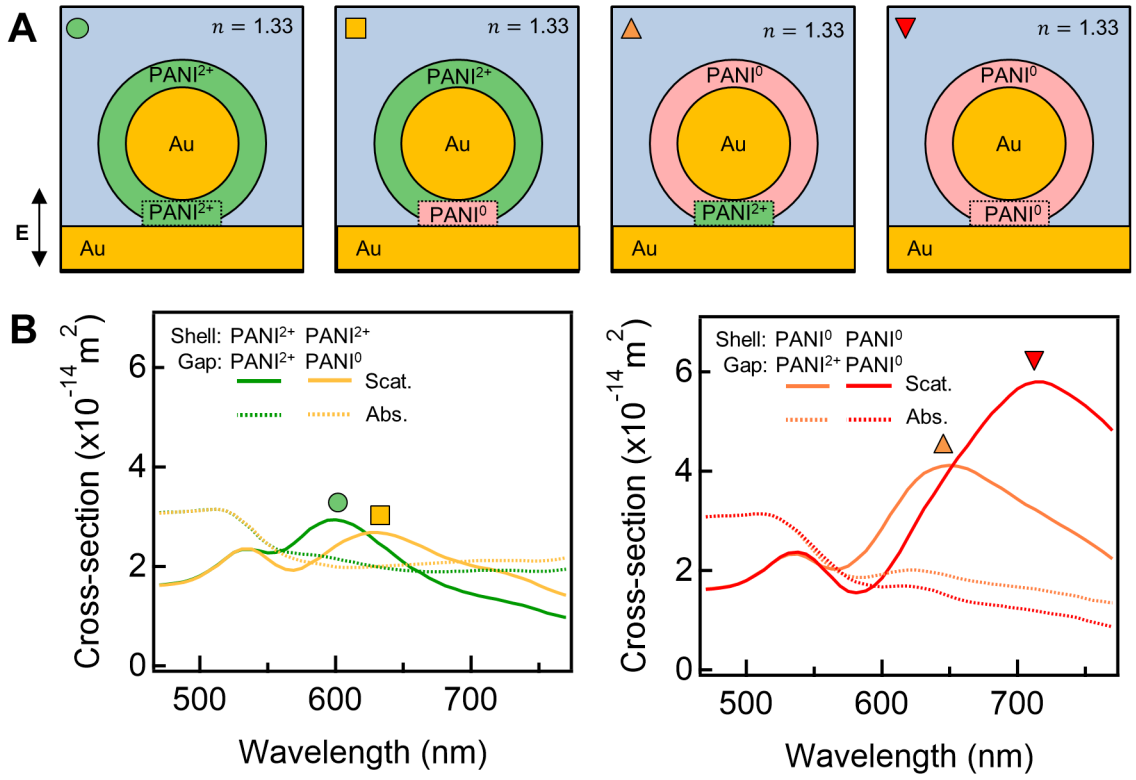

Fig. 4.11 FDTD numerical simulation of *e*NPoM for different redox states in the gap. (A) Schematic NPoMs for different situations of redox within the PANI shell (green circle: $PANI^{2+}$ shell with $PANI^{2+}$ gap, yellow square: $PANI^{2+}$ shell with $PANI^{0+}$ gap, orange upper triangle: $PANI^{0+}$ shell with $PANI^{2+}$ gap, red lower triangle: $PANI^{0+}$ shell with $PANI^{0+}$ gap). (B) Corresponding scattering (solid line) and absorption spectra (dotted line) *vs* wavelength. Partial changes in the PANI redox switching through the shell volume will lead to smaller changes in the effective refractive index surrounding the nanoparticle, so reducing the corresponding colour dynamic range.

Trying to develop additional nano-structural control is of interest for electrical switching of extremely small gap plasmonic systems [102–104], but beyond the scope of this thesis. In summary, the NPoMs made of thicker PANI shells (>15 nm) provide excellent colour performance with high fidelity, in reasonable agreement with the optimal predictions of the numerical simulation.

4.5 Correlation of Electrical and Optical Switching

The observed colour change while switching the redox state of the conductive polymer opens up the ability to track the associated electron dynamics within the tiny channel underneath individual single nanoparticles in the *e*NPoM construct. This allows further insight into how many, and how fast, electrons can be transferred through the gap of an *e*NPoM. This is important for various applications, in particular fast and energy-efficient display devices [49], as well as for fundamental nano(electro-)chemistry [105, 106].

With the *e*NPoM construct here, the redox species (PANI) are adsorbed onto the working electrode (*i.e.* the underlying Au mirror). The electron transfer between PANI and Au mirror is fast, as it occurs solely through the nanogap with negligible mass transport involved (Figure 4.12), ensuring the redox system is electrochemically reversible [107].

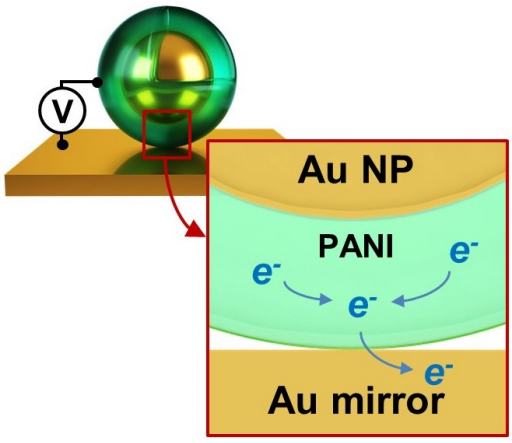

Fig. 4.12 Schematic of electron transfer from PANI to Au mirror through the gap.

The peak current i_P in the CV curve at the oxidized (or reduced) state of the *e*NPoMs is linearly proportional to the potential scan rate ν (V/s), with limited peak shift (Figure 4.13 A). In this case,

$$i_P = \nu F^2 f A / RT \tag{4.2}$$

with 2 electrons involved, and where F is the Faraday constant (C/mol), R is the ideal gas constant (J/K· mol), T is the temperature of the system (K), A is the working electrode area (m^2), and f is the surface coverage of the species on the electrode (mol/m^2) [107]. Since our experiments follow this linear dependence with ν, it shows f is constant and gives the number of PANI molecules undergoing electron transfer [108].

As f is set by the number of eNPoMs on the electrode, I am able to extract the nanoparticle density from the gradient fit (line). This then allows calibration of the number of electrons injected/collected from each NPoM (Figure 4.13 B), directly showing the electron dynamics in the gaps of single NPoMs associated with the three different redox states of the PANI (here roughly 30,000 e^- are transferred per NP for each individual redox step). On the other hand, the volume of the PANI shell (thickness t) per NP (diameter D) is given by

$$V_{\text{PANI}} = \frac{4}{3}\pi \left[(\frac{D}{2} + t)^3 - (\frac{D}{2})^3 \right] \tag{4.3}$$

Given the density of PANI ρ=1.25 g/cm^3 and molecular weight of each unit M_w=30 mg/mol [108], this implies about 2×10^4 electrons per NP are needed for each redox step (Figure 4.13 C). This corresponds well with the experimental CV data.

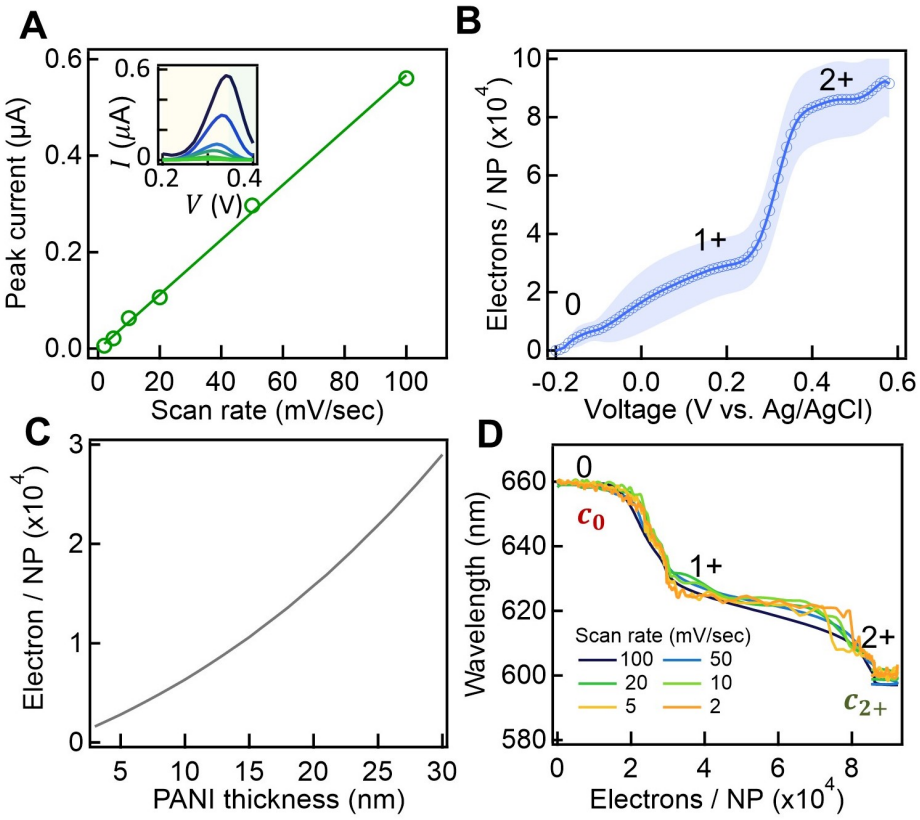

Fig. 4.13 Correlation of electrical and optical switching. (A) Peak current in CV *vs* scan rate from 2 to 100 mV/sec. Inset shows the CV peaks in oxidation. (B) Calibrated charge flow per NP in the gap of each eNPoM *vs* applied potential. (C) Estimated electron transfer per eNPoM *vs* PANI thickness. (D) Optical dynamics of coupled plasmon mode *vs* number of electrons transferred at the gap.

Remarkably, the corresponding optical dynamics measured at the same time also show two clear transitions perfectly correlated to the electron dynamics (Figure 4.13 D, Figure 4.14 shows detailed DF spectra). The correlation here provides a simple optical method for in-situ and real-time monitoring of the redox state of nanosized PANI.

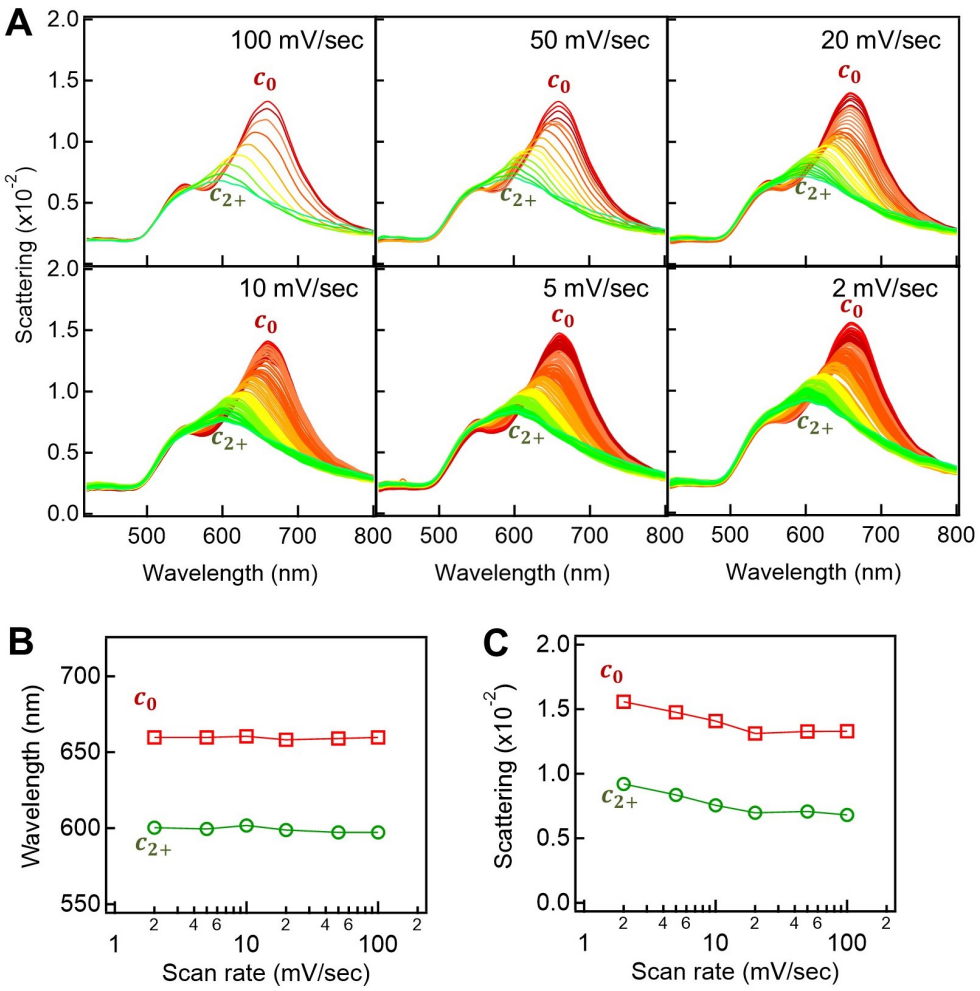

Fig. 4.14 Optical analysis for scan rate of *e*NPoMs. (A) DF scattering spectra of a single *e*NPoM for different scan rates as shown, and (B) their corresponding peak wavelengths and (C) intensities as a function of scan rate.

4.6 Temporal Response of *e*NPoM

To understand the temporal response, the optical switching of single *e*NPoMs is studied under faster square-wave electrical modulation (Figure 4.15). An abrupt redox transition of the polymer is seen when a step in voltage from 0.6 ↔ -0.2V is applied

(*vs* Ag/AgCl), causing rapid shifts in the coupled mode from $c_0 \leftrightarrow c_{2+}$, and resulting in switching of the DF scattering measured at c_0 = 640 nm (Figure 4.15 A). The switching time is 32 ms (oxidation) and 143 ms (reduction) with intensity changes of 47%. This matches the intrinsic dynamics of ultrathin planar PANI films on Au substrates [49], with >200% improved switching contrast in the enhanced scattering of the *e*NPoMs.

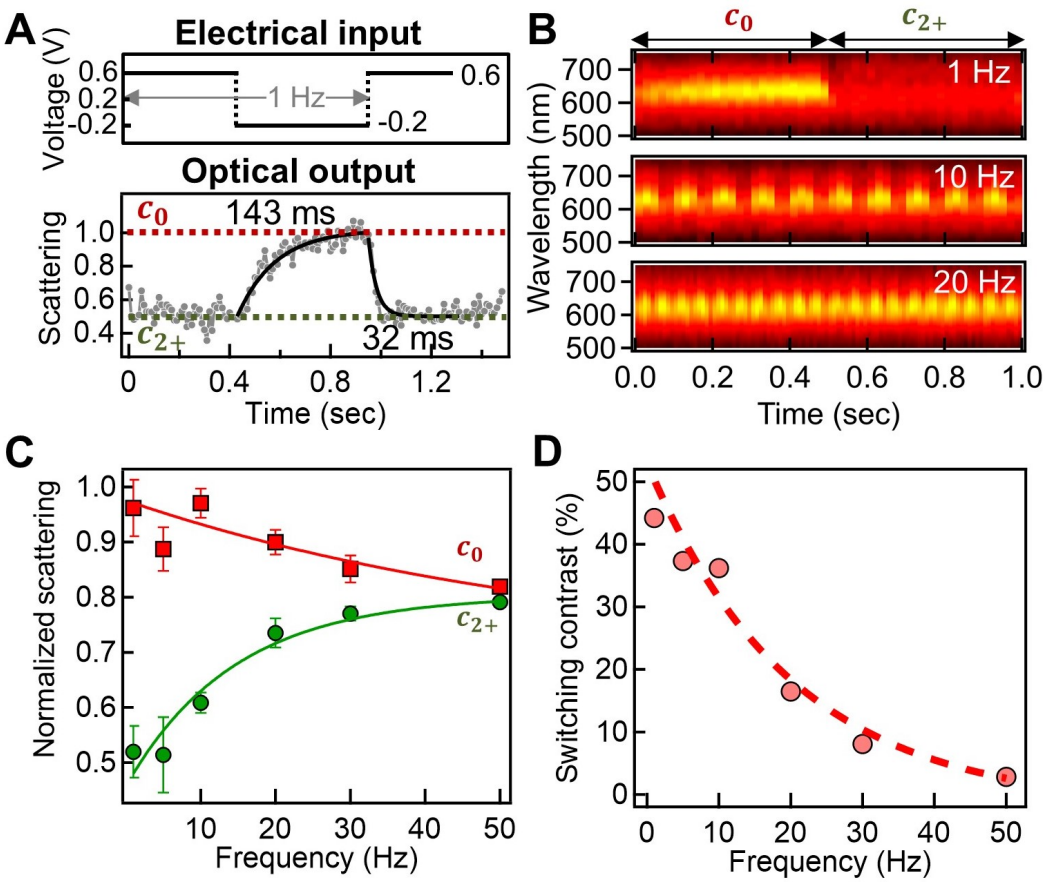

Fig. 4.15 Temporal Response of *e*NPoM. (A) Square wave modulation of the applied potential at 1 Hz (top panel) and associated normalized scattering intensity (bottom panel) of single *e*NPoM at wavelength of c_0 peak, showing dynamics for reduction (143 ms) and oxidation (32 ms). (B) Reversible optical switching of an *e*NPoM under square wave modulation at 1, 10, and 20 Hz. (C) Normalised scattering intensities and (D) switching contrast of *e*NPoM *vs* applied modulation frequency.

Reversible colour switching at the single nanoparticle level is seen in response to square wave potentials of increasing frequency up to commercial video rates of 50 Hz (Figure 4.15 B-D, with Figure 4.16 showing detailed performance) [109], providing switching performance that is already comparable to the state-of-the-art in plasmonics [43]. The

exponential decay in switching contrast for higher frequencies currently comes from the RC time-constant set by the capacitance of the cell geometry used.

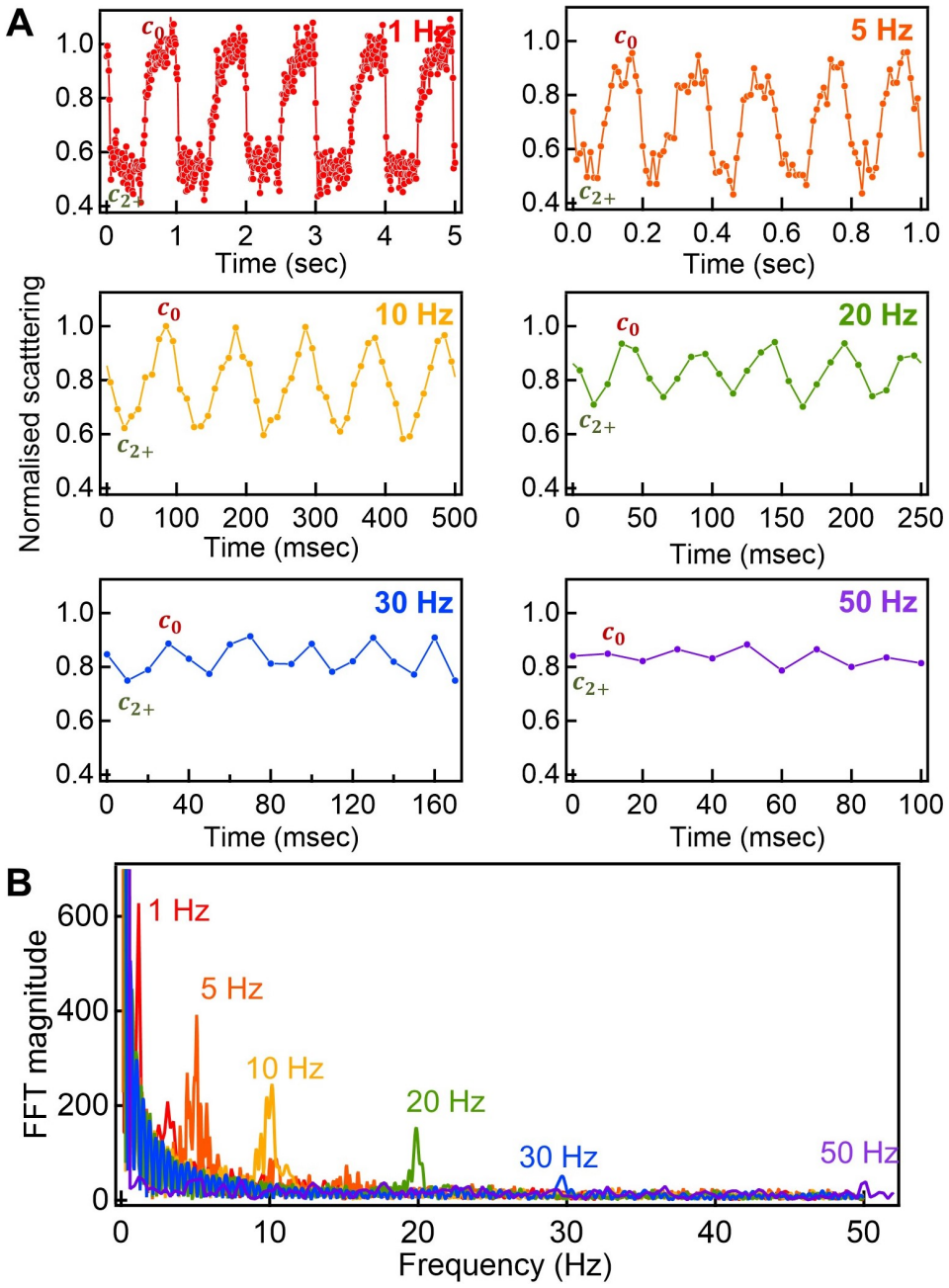

Fig. 4.16 Reversible optical switching of *e*NPoMs. (A) DF scattering intensities of an *e*NPoM at the peak wavelength c_0 in response to square waves at 1 (red), 5 (orange), 10 (yellow), 20 (green), 30 (blue), and 50 Hz (violet). (B) Corresponding FFT analysis.

Since PANI has stable charge states, I observe bistable characteristics for *e*NPoMs with the resonant modes at c_{2+} and c_0 being retained for >10 minutes (decay time constant, Figure 4.17). This therefore significantly reduces energy consumption for device applications. The retention time is currently limited by scavenger redox molecules and encapsulation that is not optimized in current devices but can be considerably extended. I emphasize that this is already 3×10^4 times extended compared to typical video-rate refresh requirements.

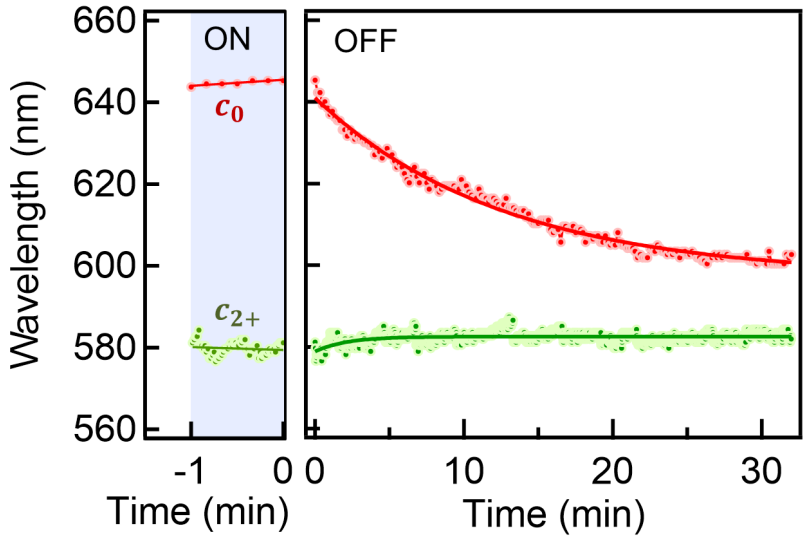

Fig. 4.17 Retention of *e*NPoM redox state. Left panel shows initial wavelength positions of c_0 and c_{2+} for the *e*NPoM at -0.2 and 0.6 V. Right panel shows corresponding peak shifts after switching off the external potential.

4.7 Summary

In this chapter, the concept of *e*NPoMs is introduced, confirmed by both FDTD simulations and experiments. Reversible optical switching of single *e*NPoM structures has been measured by dark-field scattering spectroscopy. The influence of different gap sizes set by the PANI thickness has been discussed, revealing that *e*NPoMs of thicker gap (> 15 nm) provide broader ranges of colour dynamics. In addition, the ability to use the *e*NPoM structure to track the electron dynamics by correlating electrical and optical dynamics demonstrates a useful method for monitoring the redox states of PANI, which can also be explored for other material systems. Furthermore, the switching speed and retention time have been evaluated, suggesting the potential for making video-rate displays and long-retention-time bistable optical switches.

5. Scalable *e*NPoM Metafilm

This chapter presents scalable electrically-driven colour-changing metafilms constructed using *e*NPoMs. The fabrication is based on two lithography-free methods: meniscus-guided nanoparticle assembly and aerosol jet printing. The colour dynamics now scale from the single nanoparticle level to multi-centimetre scale films on both solid and flexible substrates, with customisable patterning ability. Furthermore, intriguing directional optical effects and dynamics are experimentally demonstrated in *e*NPoMs with ultra-thin metal films. The metafilms can be used for colour-changing wallpapers, smart windows, traffic management systems, electrical signage, and many types of printed wearable plasmonic devices.

5.1 Concept of *e*NPoM Metafilm

Active plasmonic colouration describes the tunable structural pigmentation generated by metallic nanostructures and has emerged as a critical application space for plasmonics [43, 60]. As reviewed in section 2.2, plasmonic metafilms based on intricate scattering elements have been widely utilized to generate vivid colours, but a great challenge remains in how to make them:

- large-scale
- active
- flexible
- patternable.

Here I demonstrate active plasmonic metafilms by addressing these four challenges above together. Large-scale active plasmonic metafilms are formed by transferring

[1]Experimental work was undertaken in collaboration with Dr Hyeon-Ho Jeong and Dr Mike Smith. Dr Mike Smith conducted all the printing process. Part of this chapter has been published in Ref. [89, 110].

*e*NPoM constructs onto metal mirrors (Figure 5.1) by coating or printing, which is robust and readily allows for scalable manufacturing. The active colour dynamics are based on the same mechanism presented in Chapter 4, and tuned in a controlled manner by switching the redox state of the PANI shell electrically, through the adjacent mirror substrate. By replacing the solid metal mirror with flexible metallised films, deformable devices are demonstrated. In conjunction with commercially available printing techniques, metafilms can be patterned using lithography-free approaches, opening up potential for fully-printed displays (see below).

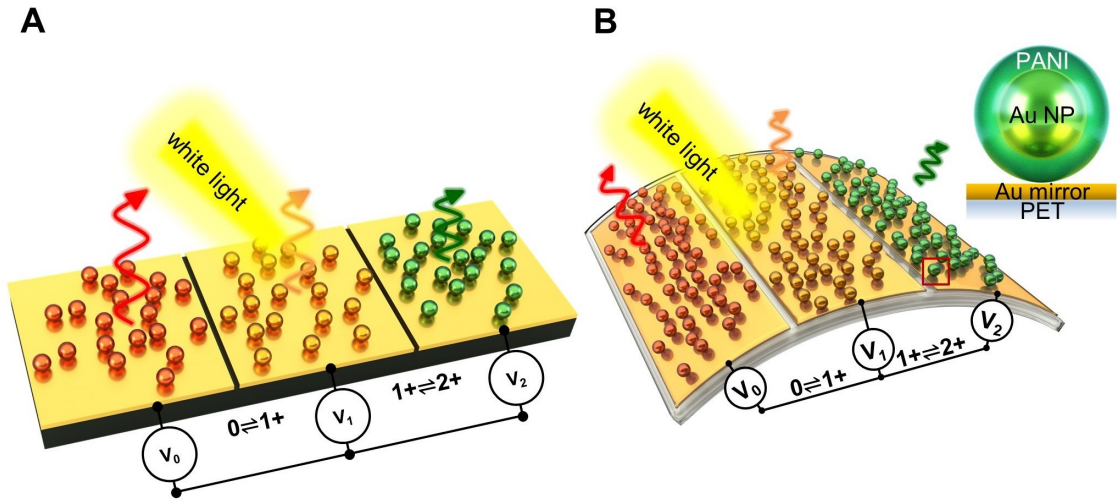

Fig. 5.1 *e*NPoM Metafilms. Schematic of *e*NPoM metafilms on (A) solid and (B) flexible substrates, whose colour changes depend on the redox state of the polyaniline (PANI) (V_0: fully reduced, V_1: half oxidised, V_2: fully oxidised). Right panel shows individual *e*NPoM.

5.2 *e*NPoM Metafilm Fabrication

In considering active plasmonics for industrial applications, one of the major challenges is the scalable cost-effective fabrication of the functional metafilms, ideally based on lithography-free methods [43]. To scale up in a controllable manner, two fabrication methods have been utilised here: one is meniscus-guided nanoparticle assembly, to produce centimetre-scale metafilms with uniform colour dynamics; another is aerosol jet printing, to make customisable patterns across tens of centimetres. It is notable that here fabricated samples' sizes are only limited by the scales of coating/printing set-ups/devices.

5.2.1 Meniscus-guided Nanoparticle Assembly

Meniscus-guided nanoparticle assembly is used here for fabricating small areas (∼1 cm^2) of uniformly-coloured *e*NPoM metafilms (Figure 5.2) [111]. The Au mirror substrate is cleaned with oxygen plasma and fixed onto a motorized translation stage (ProScan II). A volume (ca. 20-40 μL) of the colloidal PANI-coated Au NPs is dropped onto the Au substrate. A fixed fluoro-silanized hydrophobic glass plate is positioned ∼300 μm above the liquid to precisely confine the liquid during the coating process. By moving the translation stage supporting the Au substrate at a constant speed of 1 μm/s, a liquid meniscus is formed on one edge and subsequently dragged across the substrate, accumulating and coating nanoparticles. The nanoparticles are transported by evaporation-induced convection flow.

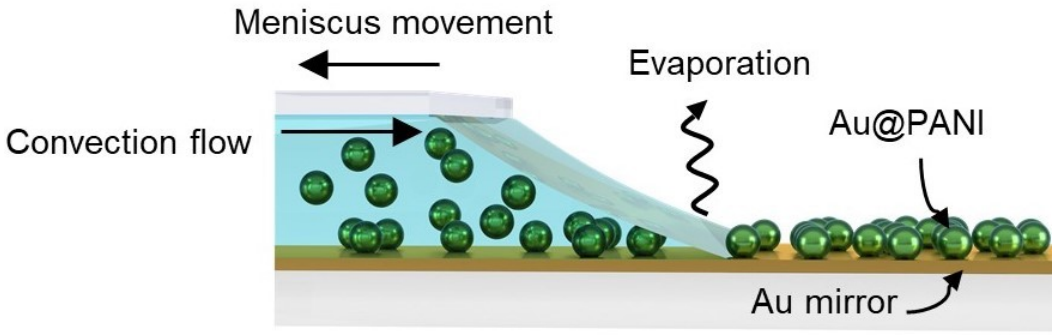

Fig. 5.2 Schematic of meniscus-guided nanoparticle assembly (not to scale).

The *e*NPoMs on the resulting metal films are randomly distributed (Figure 5.3 A). The fill fractions (the areal number density of NPs) of the final metafilms are tuned by controlling the coating parameters such as particle concentration in suspension (Figure 5.3 B) [111]. Generally, colloidal suspensions with higher volume fractions lead to higher fill fractions, showing stronger colour appearance as shown in insets of Figure 5.3 A. Other parameters like the coating speed (1 μm/s) and temperature (room temperature) are fixed here. Meniscus-guided nanoparticle assembly has been a well-established nanoparticle coating method [112]. By engineering other parameters such as solvent type, evaporation temperature, coating speed, and pretreatment of the substrate, faster coating could be achieved [111, 113], but beyond the scope of this chapter.

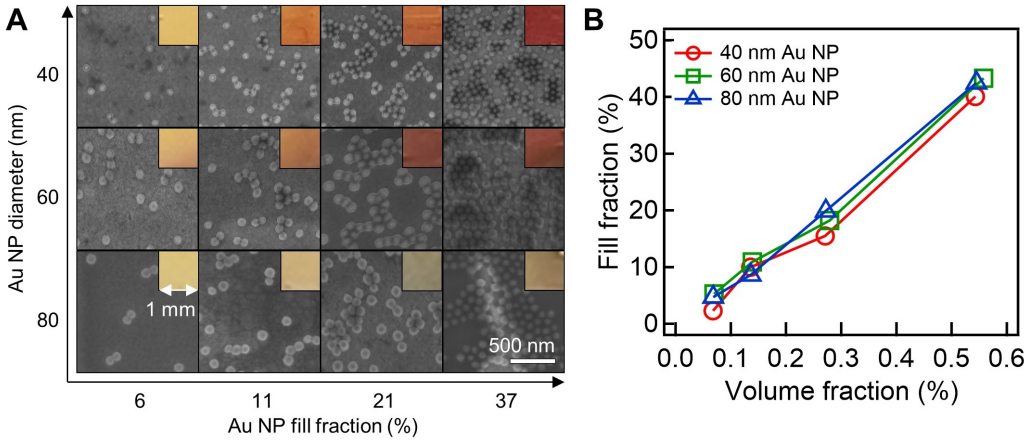

Fig. 5.3 Meniscus-guided nanoparticle assembly. (A) Meniscus-guided coating with various parameters (on evaporated Au film). SEM images and optical images (insets) of coated *e*NPoM metafilms with different particle sizes (40, 60, 80 nm Au NPs) and fill fractions. (B) Relationships between colloidal suspension volume fractions and final coating fill fractions for different particle sizes.

5.2.2 Aerosol Jet Printing

Large-area nanopatterning is one of the challenges confronting the fabrication of flexible plasmonic systems. Heavy reliance on complex lithographic processes is often needed, especially in designs requiring nanoscale precision at the wafer scale [5]. Rastering techniques including electron- and focused-ion beam lithographies [49, 114] are the preferred choice for patterning nanostructures with high precision, but they are generally expensive, time-consuming, and less compatible with flexible plastics. In contrast, imprinting and transfer approaches [115, 116] could pattern target structures on large-area substrates repeatedly. However their required predetermined master templates still rely on rastering techniques, which are expensive and vulnerable to defects (or contamination) [117]. A plausible solution to tackle such limitations is using nozzle-based nanoparticle printing techniques including 3D, inkjet, and aerosol-jet printing. Such methods have emerged as key for flexible and wearable electronics [118]. In particular, with inks containing functional nanoparticles, very thin and uniform nanostructured electronic films can be directly deposited on large-area or flexible substrates, and even 3D objects [119]. While there are a few examples of printed static plasmonics, such as surface-enhanced Raman scattering substrates [120], or thermo-plasmonic interfaces [121, 122], there have been no demonstrations for flexible electrochromic plasmonic systems.

An aerosol jet printing technique is mainly used here, which is a versatile printing technique enabling large-area fine-feature nanoparticle patterning on both rigid and flexible substrates using a broad choice of functional inks [119]. The printing ink is prepared by concentrating as-prepared PANI-coated Au NP solution to $\sim 5 \times 10^{11}$ NP/mL via centrifuging. 1 mL the PANI-coated Au NP ink is then placed in the ultrasonic atomiser reservoir of the aerosol jet printer (AJ200, Optomec). The ultrasonic atomiser creates an ink aerosol by exciting the ink with ultrasonic pressure waves. This ink aerosol is then carried by nitrogen gas, and fed towards the printing nozzle tip, where a second 'sheath' nitrogen gas flow is introduced to focus the aerosol jet (Figure 5.4).

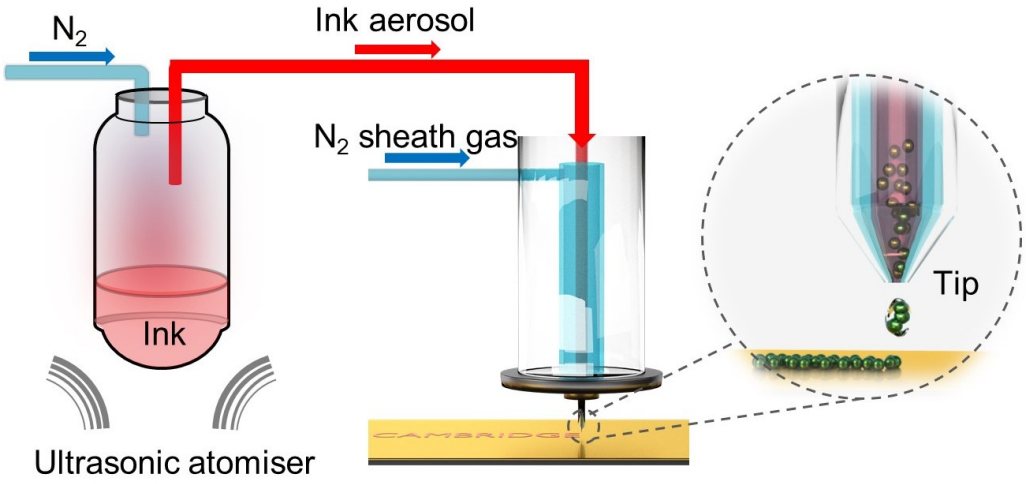

Fig. 5.4 Schematics of aerosol jet printing process.

The atomizer and sheath flow rates are adjusted independently to find optimal printing conditions and to control the width of the printed line. When using a 150 μm diameter tip, typical flow rates are around 20-50 standard cubic centimetres per minute (SCCM) and 30-90 SCCM for the atomizer and sheath flows, respectively [119]. The printed line width is $\sim$ 12.5 μm at $\sim$ 30 SCCM carrier gas flow and $\sim$ 40 SCCM sheath flow (Figure 5.5 A). A sparsely distributed fractional monolayer of *e*NPoMs is formed within the printing line. Sparse aggregates form because of capillary forces during drying of the ink droplets or overcoats via multiple printing, but this does not influence the colour appearance as the optical coupling between neighbouring nanoparticles is minimized by their $>$ 40 nm thick polymer separation.

The printing substrate is fixed on a translational stage which moves beneath the print head at a speed of 1 mm/s. A square loop test pattern (1 mm^2) is first used to explore

the optimal printing conditions in order to get uniform colour appearance across the patterned area with minimal printing time (here 78 s/mm^2, Figure 5.5 B, while the coating speed for meniscus-guided nanoparticle assembly is ∼16 mins/mm^2). The *e*NPoM fill fraction in the printed area can be tuned by simply overprinting the layer multiple times. Alternatively, controlling the nanoparticle concentration in the printing ink can enhance the printing speed but can lead to creation of more *e*NPoM aggregates in the film.

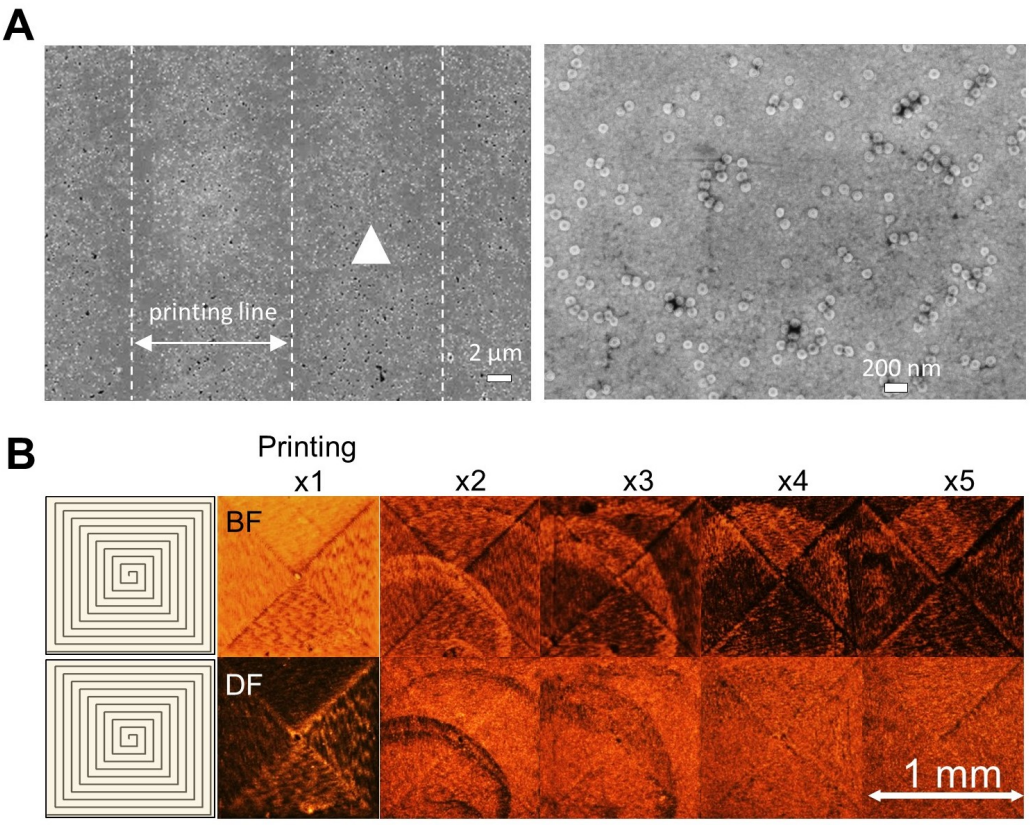

Fig. 5.5 Aerosol jet printing test. (A) SEM images of printed lines, the right panel is zoomed-in image area indicated by the white triangle. (B) Bright field (BF, upper panel) and dark field (DF, lower panel) images of the printed *e*NPoM metafilms using aerosol jet printing. From left to right shows increasing overwriting series from 1-5 times. The left panel is a schematic of the square loop test pattern.

5.3 Metafilm with Solid Substrates

Metafilms with fill fractions of ∼ 20% are fabricated via meniscus-guided nanoparticle assembly by using 0.3% volume fraction of the initial colloid (as-fabricated sample

images built from 20-, 40-, and 60-nm-diameter Au NPs see Figure 5.6 A). Higher fill fraction leads to stronger scattering intensity, but with negligible changes in the colour tuning range (scattering intensity increases by around 50% when fill fraction changes from 6% to 21%, Figure 5.6 B). So optimal colour appearance can be tuned by controlling the fill fraction.

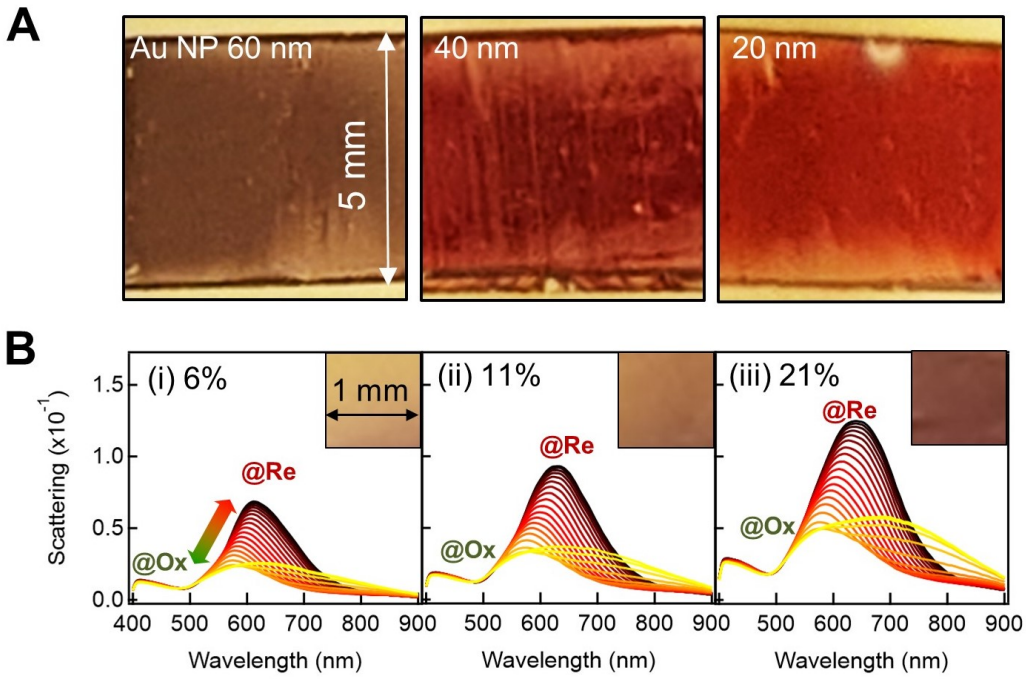

Fig. 5.6 *e*NPoM metafilms with solid substrate (template stripped Au film), fabricated by meniscus-guided nanoparticle assembly. (A) Images of *e*NPoM metafilms composed of 60, 40, and 20 nm Au NPs (from left to right) as fabricated. (B) DF scattering spectra of *e*NPoM metafilms composed of 60 nm Au NPs with different fill fraction from 6 to 21% (from left to right), *vs* voltage applied from -0.3 ↔ 0.8 V. Insets are corresponding optical images of samples as fabricated.

The metafilms are composed of randomly-distributed *e*NPoMs. As the PANI thickness is around 20 nm, so the lateral separation of two neighbouring Au NP cores is over 40 nm. Simulations show that optical near-field coupling between the *e*NPoMs has negligible influence on the colour tuning range (Figure 5.7). The near-field coupling almost disappears when the lateral separation of two neighbouring *e*NPoM is over 10 nm, matching the saturation of coupled plasmon mode peak tuning ranges (Figure 5.7 C). This means the *e*NPoM colours are controlled solely by the active gap under each *e*NPoM instead of the near-field coupling of neighbouring *e*NPoMs, which is essential for this easily scalable fabrication.

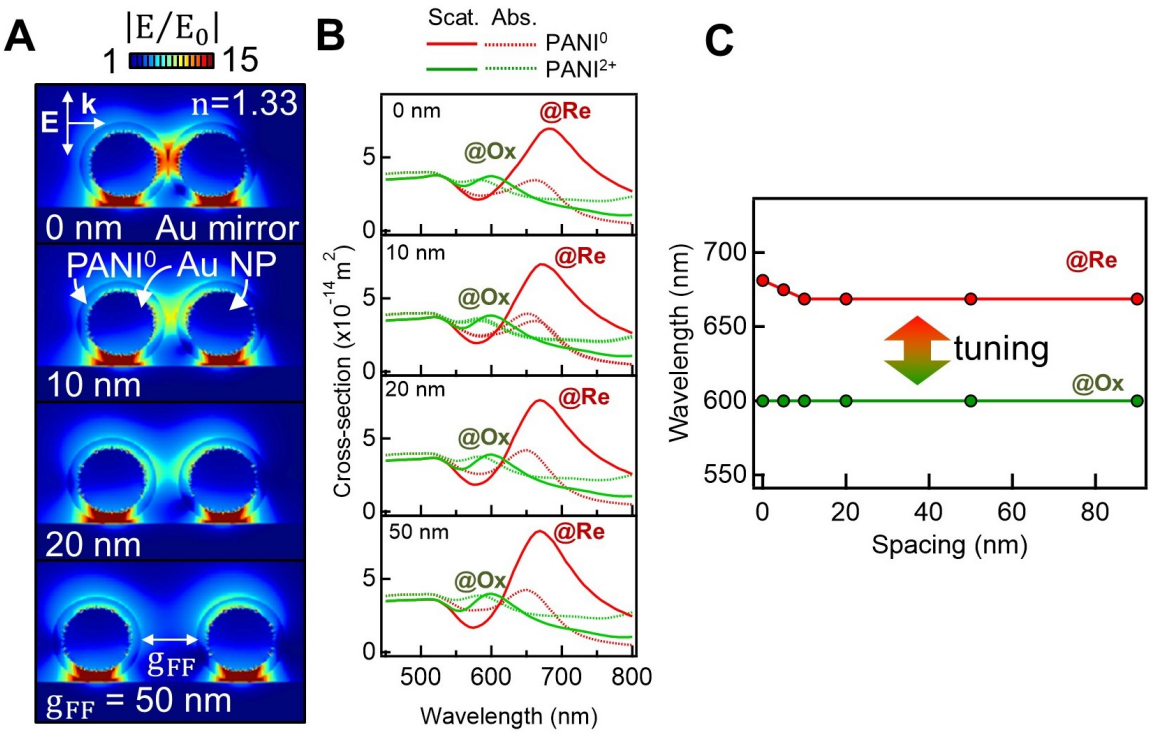

Fig. 5.7 Simulations of two *e*NPoMs with different lateral separation. (A) Optical near-field enhancements of two *e*NPoMs *vs* lateral separation. (B) Corresponding simulated optical scattering (solid lines) and absorption spectra (dotted lines) with reduced (red) and oxidized (green) PANI. (C) Corresponding coupled plasmon mode peaks *vs* lateral separation.

Remarkably, this scaled-up *e*NPoM metafilm reveals vivid uniform colour switching over the entire surface, controlled by the same electrochemical set-up as described in Chapter 4 (*e*NPoM metafilms built from different sizes Au NPs, Figure 5.8 A). For samples with 60-nm-diameter Au NPs, 79 nm peak wavelength tuning and 57% switching contrast are observed (DF spectra see Figure 5.6 B). The switching ranges are identical to the single *e*NPoM behaviour, confirming the lack of any effects from the disordered configuration for fill fractions $< 20\%$. A simple university logo is printed on Au film as a demonstration for patterned devices (Figure 5.8 B). The pattern changes colour both in BF and DF illumination when voltage is applied, proving the possibility for active plasmonic display type of devices. This metafilm already operates for over three months (Figure 5.8 C). The colour ranges and dynamics supported by *e*NPoM metafilms can potentially be further extended by mixing different nanoparticles or using UV plasmonic nanoparticles.

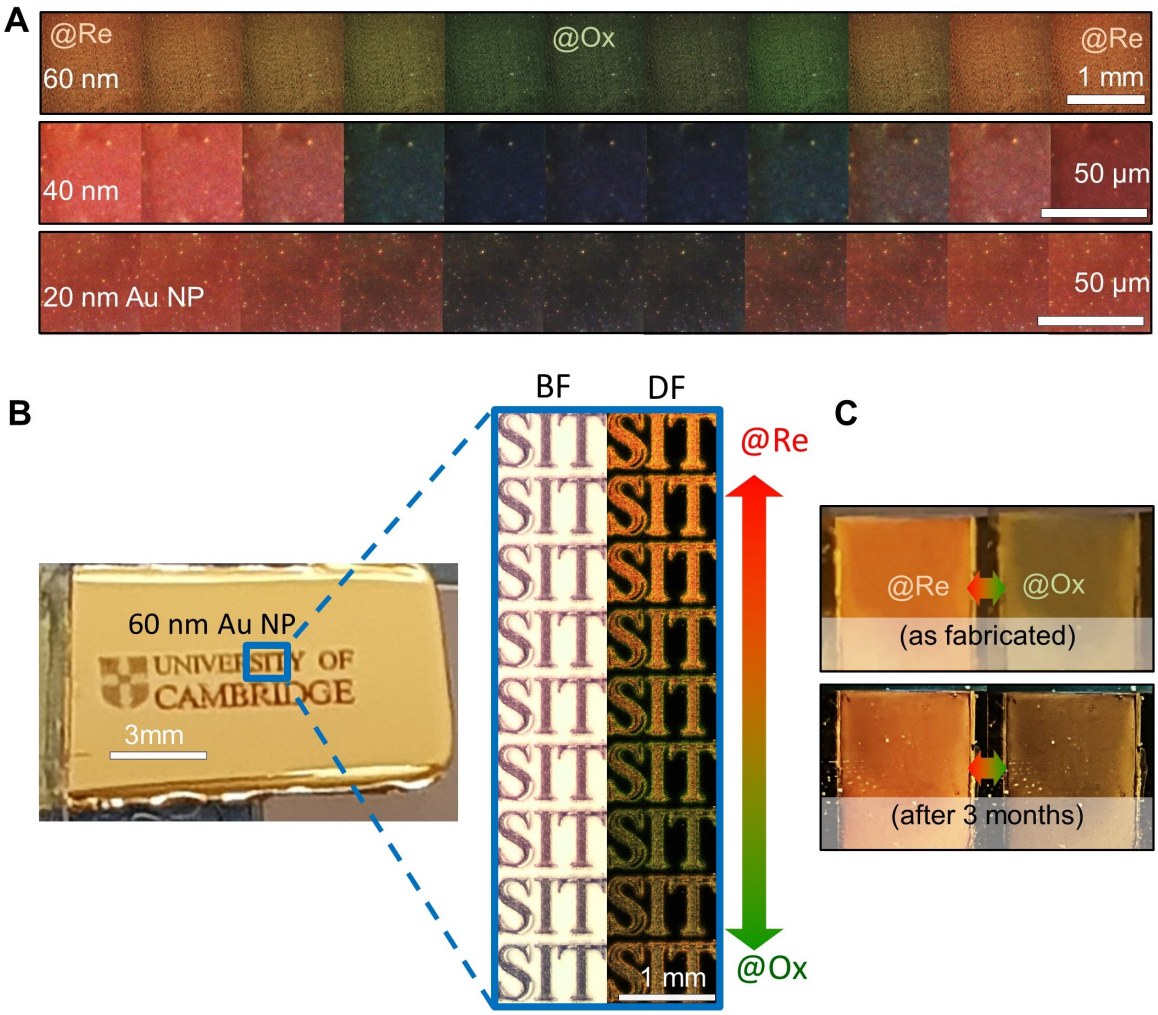

Fig. 5.8 Scalable colour generation of *e*NPoM metafilms with solid substrates. (A) DF images of the *e*NPoM metafilms built from 20-, 40-, and 60-nm-diameter Au NPs during PANI redox. (B) Printed patterns of *e*NPoMs on evaporated Au film. The right panel shows corresponding BF and DF optical images when the voltage is applied from -0.15 ↔ 0.65 V. (C) Optical images of the 60-nm-diameter Au NPs sample under ambient light before and after 3 months.

The active plasmonic metasurface demonstrated here appears highly competitive with current and suggested technologies (Figure 5.9) [123]. In particular, it has visible wavelength tuning, ultrasmall pixel size and near-video-rate switching that has been hard to achieve before and matches requirements for display need (green box), with high pixel densities ($> 10^9$ pixels per inch, PPI). This method is scalable and highly compatible with flexible systems, so is ideal for large-scale roll-to-roll manufacturing

on deformable polymer substrates and suggests useful industrial applications for active plasmonic colours [124].

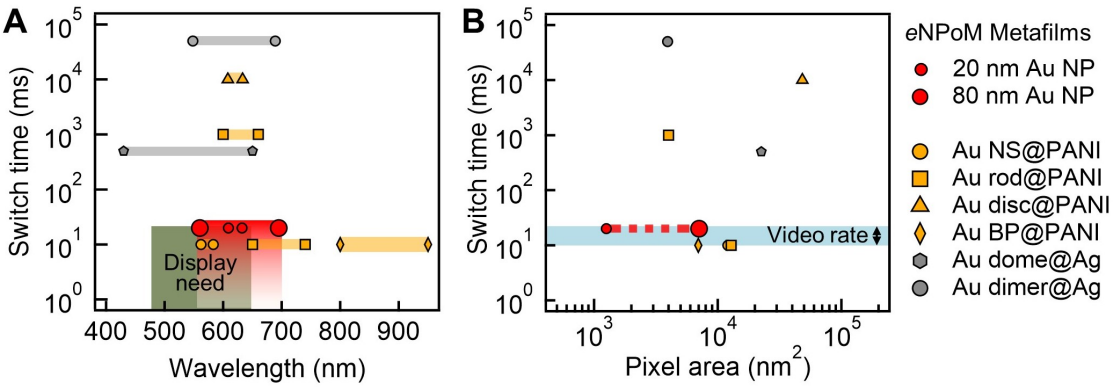

Fig. 5.9 Optical dynamics of electrochromic plasmonic nanoparticles. Switching times of various electrochromic plasmonic nanomaterials *vs* their associated (A) optical dynamic ranges and (B) pixel areas: *e*NPoMs (red circle), Au nanospheres (NSs) coated with PANI (yellow circle), Au rods coated with PANI (yellow square), Au bipyramids (BPs) coated with PANI (yellow bipyramid) [93], Au discs coated with PANI (yellow triangle) [125], Au domes coated with Ag (grey hexagon) [56], Au dimers coated with Ag (grey circle) [57]. Green box indicates needs for commercial displays, matching what can be achieved with *e*NPoMs (red box).

5.4 Metafilm with Flexible Substrates

One highly-desired feature for device configuration is large-area flexibility, spanning from wearable devices [126–128] to architectural films. Flexible static plasmonics can be formed via plasmonic nanostructures on plastic films [129], but it has been challenging to make these colours controllable electrically. One popular approach is to position plasmonic elements onto deformable flexible materials, typically elastomeric polymers [130–134]. Mechanical deformation of these stretchable/bendable substrates modifies the inter-element spacing, providing active optical tuning. However this limits their adoption since tuneability is limited and creating the forces required is nontrivial, particularly electrically. By contrast, combining plasmonic systems such as gratings [49] or thin-film cavities [50] with stimulus-responsive materials [135] such as electrochromic [43, 49–51, 136] or phase change materials [52, 56, 137, 138], promises electrically-tunable colour switching. However these devices are typically rigid and suffer

from limited optical switching (solely 'on-off' function) [43, 49–51, 136], long response times (multi-second) [56] and/or poor long-term reproducibility (< 1 month) [58].

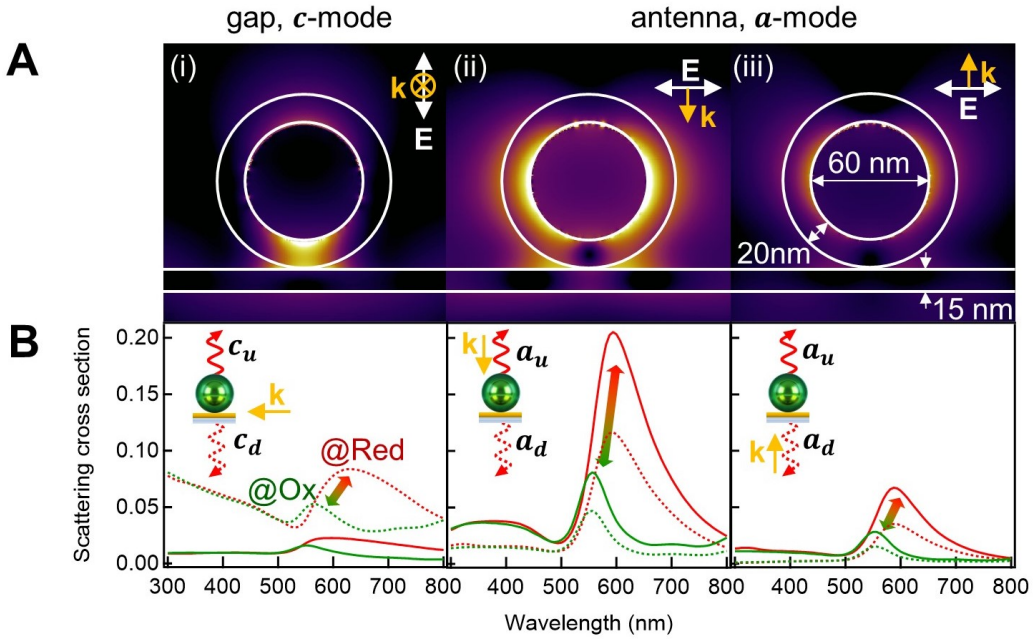

Fig. 5.10 Simulated optical dynamics of *e*NPoM metafilms with an ultra thin metal mirror. (A) Optical near-field enhancement of the *e*NPoM for reduced state of PANI, with different polarized light illumination (i, gap mode, ii,iii, antenna modes, upper panel), and (B) their corresponding upward (solid lines) and downward scattering (dashed lines, bottom panel). The refractive index of the PET film is set as n=1.65 [139], and the whole surrounding environment is set as water (n = 1.33), to simplify the simulations.

A rational approach to make the *e*NPoM metafilm flexible is through an ultrathin metal mirror configuration, using very thin and continuous metal films, such as a flexible gold-coated polyethylene terephthalate (Au-PET) film. Initial theoretical investigations explore how metal layers thin enough to be bendable can still act as mirrors to plasmonically confine light inside the gap. In simulations, when illuminated from (i) side-on, (ii) above, or (iii) the underside of the *e*NPoM, different plasmonic modes are excited which present similar spectral dynamics in all cases (red to green according to the change in the redox state of the PANI shell upon cycling $V_0 \leftrightarrow V_2$, Figure 5.10). For *e*NPoMs with Au mirror thickness h= 15 nm, the case (i) where incident light is polarized perpendicular to and propagating along the Au-PET film shows the optical field is strongly confined in the gap between the Au NP and the

Au-PET film [17, 140]. This results in a strong coupled gap resonance (*c*-mode ∼631 nm peak wavelength at V_0) which redshifts by ∼50 nm for $V_0 \rightarrow V_2$ in both upward (c_u) and downward (c_d) scattering with maximum c_d >200% higher than c_u (Figure 5.10 i). This is because the *c*-mode is almost independent of mirror thickness (even when below the skin depth of gold, ∼40 nm) [141], but the light penetrates through the thin mirror and scatters downwards, rather than entirely up-scattering as for thick Au mirrors (>45 nm) [13, 141, 142]. On the other hand when illuminated from above (Figure 5.10 ii) or below (Figure 5.10 iii), its transverse antenna α-mode is excited, appearing weaker from below since the incident light suffers absorption in the mirror. No matter which illumination direction [141], the upward scattering intensity a_u is almost double the downward direction a_d, due to the radiation pattern of this mode. In all three cases, no matter which modes are excited, identical colouration and dynamics in scattering are predicted. This shows that the valuable properties of *e*NPoMs are preserved in the thin-metal film version required for flexible devices, and that the scattering is independent of direction, as required for ambient-light reflective devices.

5.4.1 Printed Flexible Metafilms

A simple university logo is printed on 15 nm thick Au layer PET films (Eastman Flexvue) with 60 nm diameter Au NPs coated with 20 nm thick PANI, for proof-of-concept flexible devices (Figure 5.11, 5.12). The nanogap between the Au NP and the thin-mirror is precisely controlled by the thickness of the PANI shell via the wet chemistry growth (inset of Figure 5.11 C). Since these nanogaps critically determine the colour of the film and are extremely monodisperse (19.4 ± 3 nm), their colouration is not only vivid under ambient light (only 7% fill fraction of the NPs), but also remains uniform over multi-centimeter lengthscales while bending the film, never previously possible with any plasmonic system (Figure 5.11 B). When the redox state of PANI is changed electrochemically ($V_0 \leftrightarrow V_2$) using the bottom ultrathin metal, vivid uniform colour dynamics can be observed under both dark-field (DF) and bright-field (BF) illumination (Figure 5.11 D). With further engineering of the ink rheological properties, this printing method can be suited for commercial large-scale industrial printing rigs, or consumer household printers (in progress), leading to widespread customized flexible and wearable plasmonic display devices.

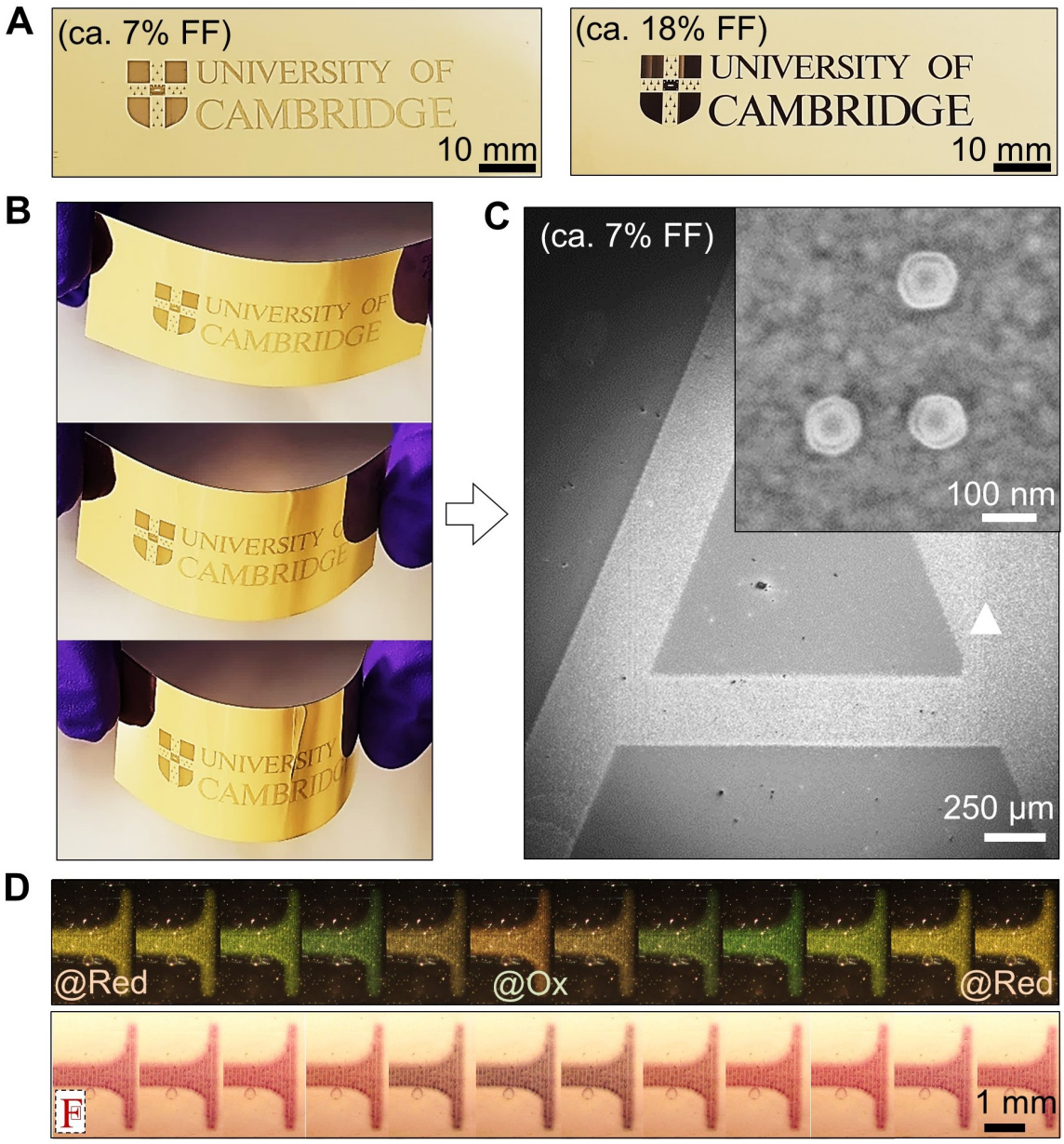

Fig. 5.11 Printed flexible *e*NPoM metafilms. (A) Exemplary printing samples with 7% and 18% fill fraction. (B) A series of photos of a printed flexible plasmonic film while bending. (C) SEM image of printed character 'A', inset shows the core-shell structure of PANI-coated Au nanoparticles. (D) DF and BF optical images of printed partial character 'F' *vs* voltage applied from -0.15 ↔ 0.65 V (sample with 7% fill fraction).

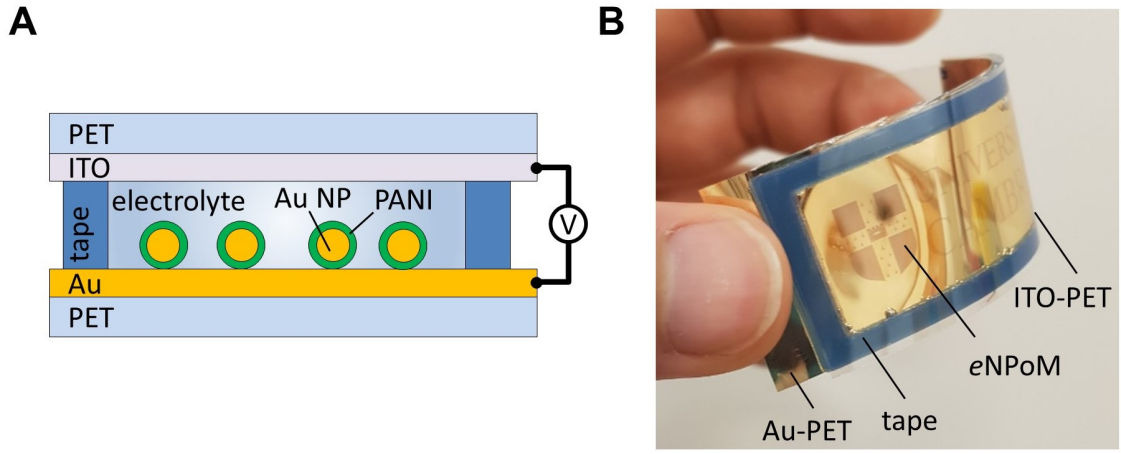

Fig. 5.12 Large area flexible active plasmonic devices. (A) A schematic front view of the device configuration. (B) Image of a demonstration device.

5.4.2 Directional Optical Effects

Colour differences between DF and BF scattering (apparent in Figure 5.11 D) are due to the contributions of light absorption and reflection from the *e*NPoM. I thus now systematically investigate the directional colouring effects in plasmonic metafilms while reducing the Au mirror thickness. Centimetre-scale *e*NPoM metafilms with different thickness of Au mirror (h=5, 10, 15 nm, from Eastman Flexvue) are first fabricated via meniscus-guided nanoparticle assembly. When large-area patterning is secondary, meniscus-guided nanoparticle assembly is used since only ~20-40 μL of the ink is required for small areas (~1 cm^2) of uniformly-coloured *e*NPoM metafilms [113, 143].

Omnidirectional Colouration in *e*NPoM Metafilms

The scattering of the *e*NPoMs display distinct chromatic directionality, changing with incident direction and Au mirror thickness (Figure 5.13). I first examine back-illumination where the *e*NPoM colour appearance hinges on the wavelength and intensity of the light coming through the mirror (Figure 5.13 A). For comparison, the calculated scattering and absorption of *e*NPoMs with different Au mirror thickness at different redox states of the PANI shell is evaluated (Figure 5.13 C). When PANI is oxidized (V_2), the absorption overwhelms the scattering (over two-fold), thus removing the colour appearance for all mirror thicknesses. In the reduced state of PANI (V_0), the scattering increases and overcomes the absorption for Au mirror thickness below 10 nm.

Omnidirectional scattered colours and tuning are thus predicted in the *e*NPoM metafilm with thin Au mirrors (here 5 nm), with the capability for dimming (or blocking) the downward scattering by controlling the mirror thickness.

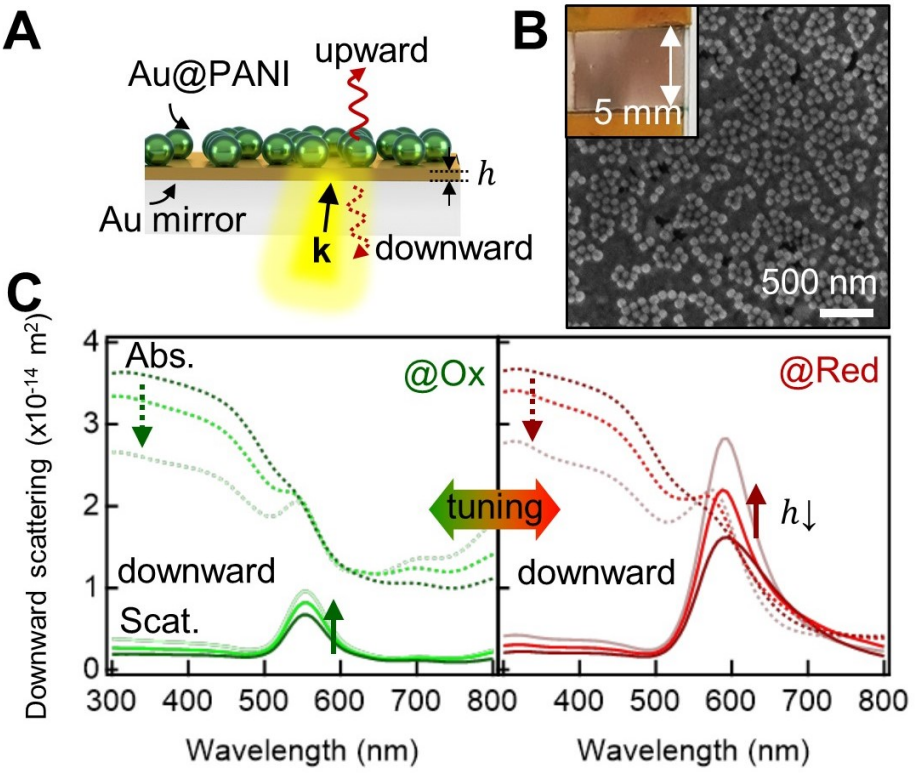

Fig. 5.13 Omnidirectional colouration in scattering. (A) Schematic of *e*NPoM metafilm and (B) SEM image of film coated using meniscus-guided nanoparticle assembly. Inset shows corresponding optical image. (C) Simulated downward scattering (solid line) and absorption (dashed line) spectra for oxidation (green) and reduction (red) states of PANI with different Au thickness (15 nm, 10 nm, 5 nm from dark to faint lines).

Experimentally, reversible colour dynamics and optical switching are indeed observed in the *e*NPoM metafilm with 5 nm Au thickness (Figure 5.14). The upward scattering peak shifts from 633 nm to 572 nm when $V_0 \rightarrow V_2$, losing ~100% intensity. The downward scattering gives similar trends but with reduced tuning range, shifting from 616 nm to 565 nm with ~46% intensity loss (Figure 5.14 B). The film is thus omnidirectionally coloured in the oxidized state.

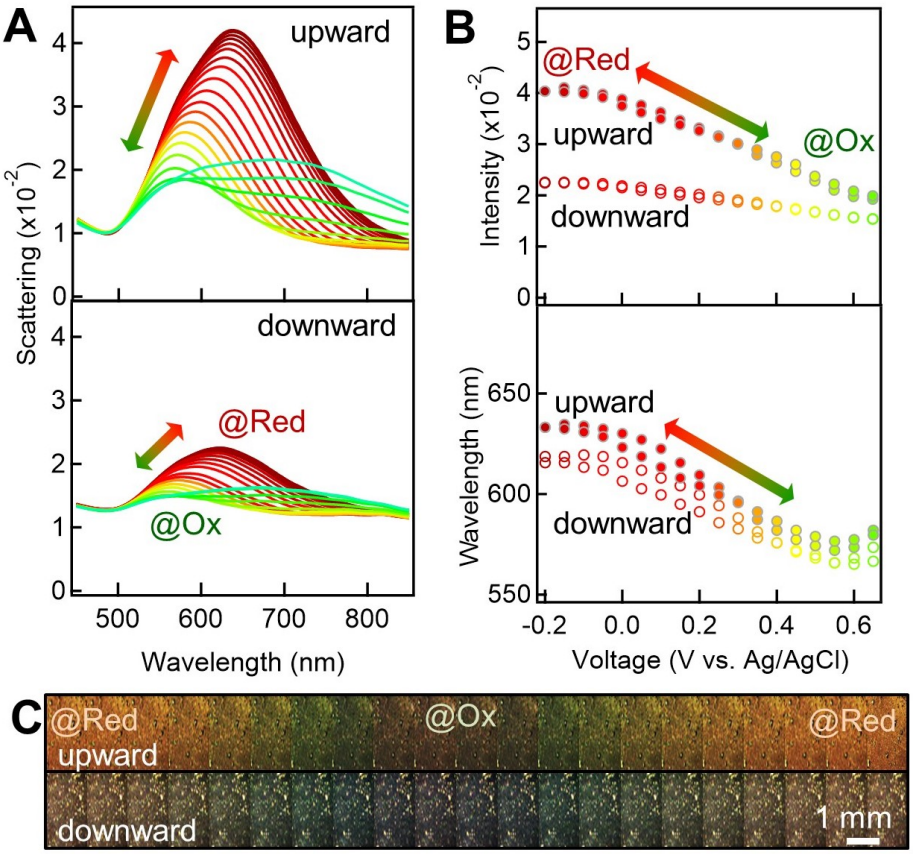

Fig. 5.14 Experimental omnidirectional colouration in scattering of the *e*NPoM metafilm with 5 nm Au thickness. (A) Scattering spectra, (B) corresponding coupled mode peak intensity and wavelength change and (C) experimental DF upward- (top) and downward-scattering images (bottom) *vs* applied voltage -0.2 ↔ 0.65 V.

The comparison of colour dynamics of *e*NPoM metafilm made with different Au thickness is shown in Figure 5.15. As expected from simulations, both upward- and downward-scattering are seen for h= 5, 10 nm Au thickness while only upward scattering can be measured for h= 15 nm Au thickness. This shows the capability to tune from omnidirectional colouration (for thin mirrors) to single-sided colouration (for thick mirrors), solely using the Au mirror thickness.

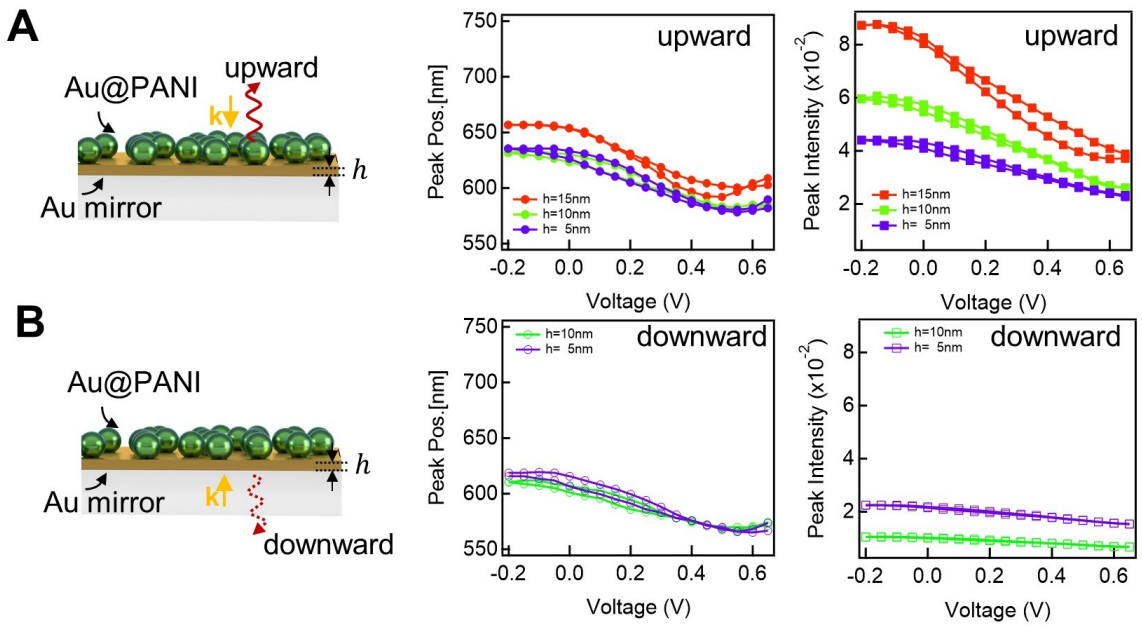

Fig. 5.15 Experimental scattering of the *e*NPoM metafilm with 5, 10, 15 nm Au thickness. (A) Upward- and (B) downward- scattering coupled mode peak wavelength and intensity change *vs* applied voltage -0.2 ↔ 0.65 V. The downward scattering for h = 15 nm Au thickness is not detectable so not shown.

Bidirectional Colouration in *e*NPoM Metafilms

The omnidirectional plasmonic colouring in scattering from the thin-mirror configuration can be transformed into bidirectional colour dynamics by incorporating reflection effects (Figure 5.16). Samples are now observed in bright-field (BF) to quantify how additional surface light reflection from the surrounding mirror changes the colour appearance of the *e*NPoM metafilms. Metafilms with both h=15 nm (left panel Figure 5.16 A) and h=5 nm thick Au mirrors (right panel) show vivid uniform colour modulation in the upward reflection from ∼580 nm to ∼620 nm when the external voltage is switched between $V_0 \leftrightarrow V_2$ (Figure 5.16 B for reflection spectra). By contrast, the downward reflection of the metafilm depends on mirror thickness: 15 nm thick Au acts as a near-complete mirror, reflecting all light and appearing golden with negligible electrochromic tuning. For the 5 nm thick Au, a stronger colour dynamic is observed from 545 nm to 557 nm that differs from the up-reflected tuning (Figure 5.16 C, D show colour gamut plots). This dynamic tuning is highly reproducible over $>$ 100 cycles of $V_0 \leftrightarrow V_2$. A fully reversible bidirectional colour dynamic tuning is thus achieved in a plasmonic system.

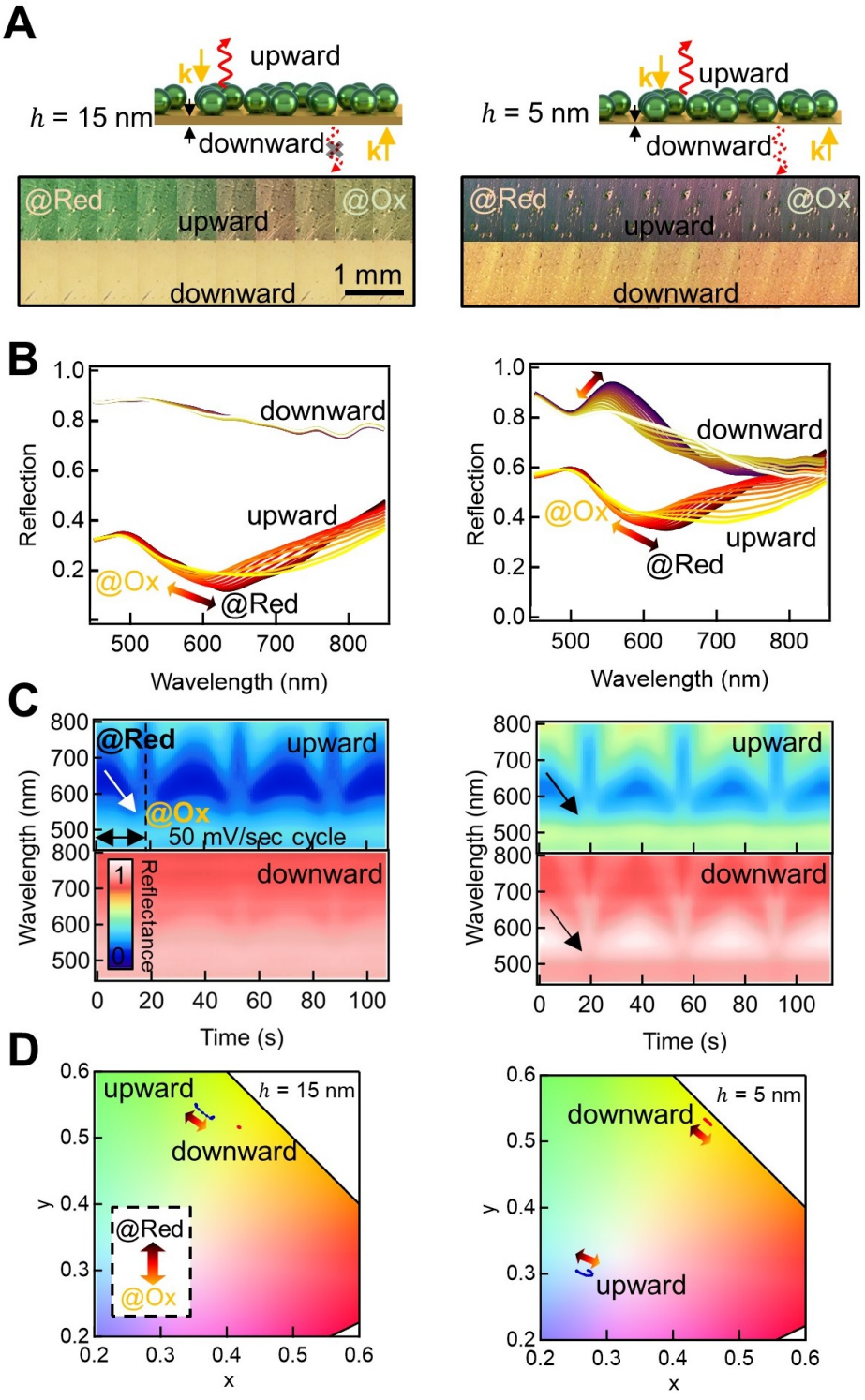

Fig. 5.16 Bidirectional colouration in reflection. (A) Schematic of the *e*NPoM metafilms with thick (15 nm, left panel) and thin Au layers (5 nm, right panel) and their corresponding bright field (BF) optical images in up- and down-ward reflection. (B) Normalized reflection spectra *vs* voltage change. (C) Time scans of normalized reflection spectra for 3 cycles of voltage -0.2 ↔ 0.65 V at scan rate 50 mV/sec, and (D) corresponding colour gamut dynamics (CIE 1964).

While commercial applications of dichroism such as dichroic glass are generally based on thin-film interference [144] whose structures are static and rigid [145–148], these *e*NPoM metafilms are flexible and electrically-tunable. They thus compare favourably with the original 4th century demonstration seen in the 'Lycurgus Cup'. This bidirectional tunable colour dichroism could thus be developed for flexible active dichroic devices.

5.5 Summary

In summary, this chapter demonstrates the ability to use *e*NPoM structures to make scalable active plasmonic metafilms with dynamic colouration. Large-area active plasmonic metafilms are fabricated on both solid and flexible substrates. In conjunction with commercially-available printing techniques, metafilms comprising a monolayer of electrochromic nanoparticles (< 100 nm) can be laid-down uniformly and patterned precisely, offering possibilities to make all-printed wearable plasmonic devices including displays, electronic textiles, or biochemical sensors [149, 150]. The whole process is lithography-free and thus readily extends to large scale processing tools, for instance roll-to-roll manufacturing [151]. In addition, using directional optical effects that can be controlled with this ultrathin mirror configuration, such flexible active plasmonic metafilms can generate electrically controllable omni- or bi-directional colour dynamics, which could be used for 'magic-mirror' displays, colour-tunable glass, and architectural decoration. Although the presented colours are currently limited, they can be further extended by engineering the gap materials (for instance with alternative or blended conducting polymers or other responsive organic/inorganic/hybrid materials) or the plasmonic materials (utilizing other metals such as Ag, Al, or dielectric scatters).

6. *e*NPoM for Nanoelectrochemistry

This chapter explores the redox dynamics of nanosized conjugated conductive polymer within the nanopixels. Optical dynamics of *e*NPoMs made with different conjugated conductive polymers are investigated with dark-field and Raman spectroscopy in real-time while voltage is applied. The modulation of the optical response reveals the redox dynamics inside the tiny gap.

First, the reversible optical switching with colour dynamics is demonstrated for *e*NPoMs made from polypyrrole-coated Au NPs (Au@PPY) and poly-3,4-ethylenedioxythiophene-coated Au NPs (Au@PEDOT), followed by a comparison with polyaniline-coated Au NPs (Au@PANI) as introduced in Chapter 4. Then, in-situ Raman spectroscopy is used to probe the conformational and structural changes of the nanosized conjugated conductive polymer within the individual plasmonic cavities, which provides molecular-level information of the redox mechanisms.[1]

6.1 Optical Dynamics of Different Conductive Polymers

In Chapter 4, *e*NPoMs with Au@PANI are demonstrated with electrochemically-modulated optical switching, which also allows for visualization of PANI's redox states by the colour dynamics at the single nanoparticle level. The colour change is determined by the charge state of the polymer within the plasmonic nanogap. The concept of *e*NPoMs can be demonstrated with not only PANI, but also other common conjugated conductive polymers like polypyrrole (PPY) or poly-3,4-ethylenedioxythiophene (PEDOT), as shown in Figure 6.1.

[1] Experimental work was undertaken in collaboration with Dr Qianqi Lin and Dr Hyeon-Ho Jeong.

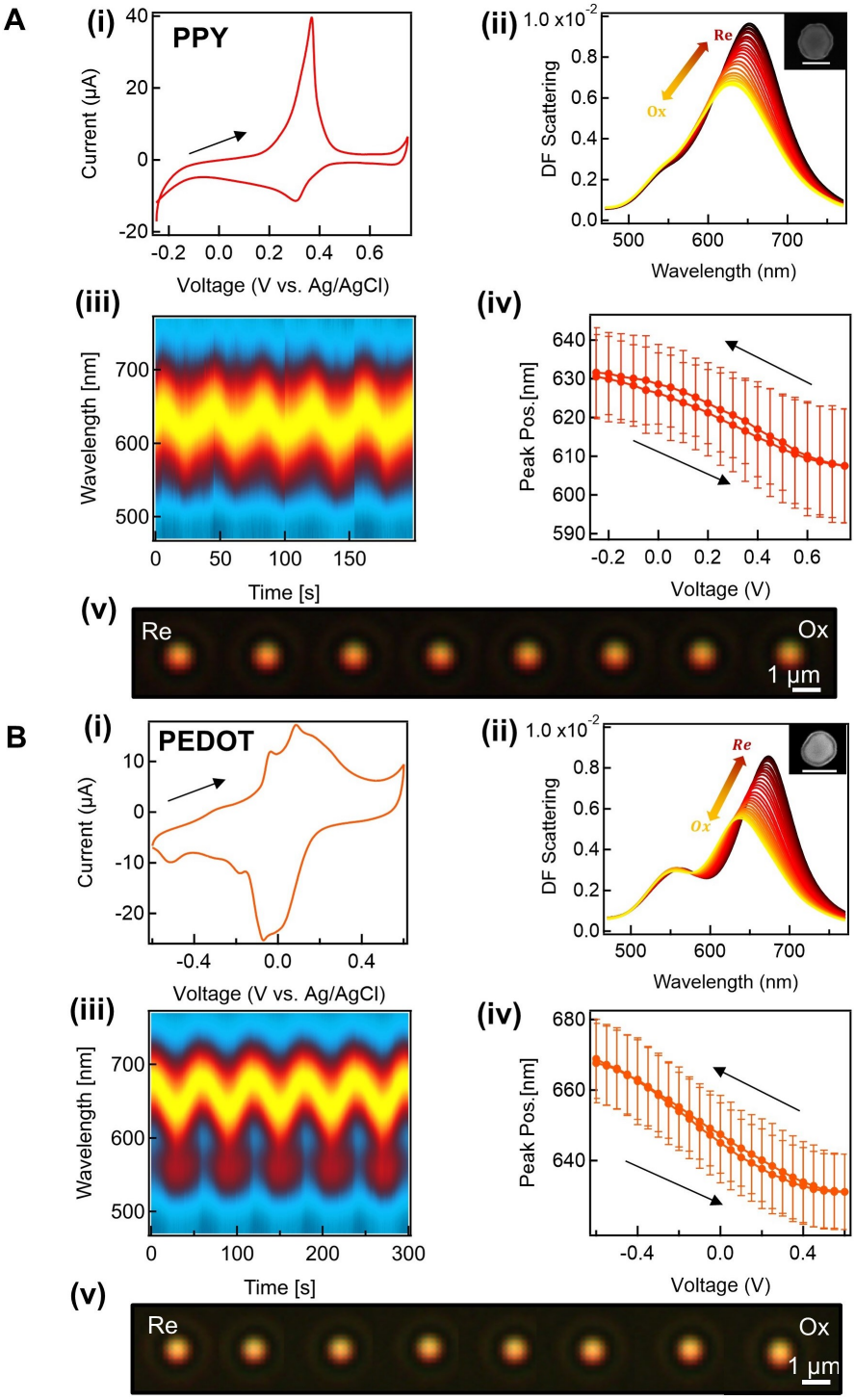

Fig. 6.1 Electrically-driven optical switching of *e*NPoMs made from (A) Au@PPY for ramped voltages -0.25 ↔ 0.75 V and (B) Au@PEDOT for ramped voltages -0.6 ↔ 0.6 V, with corresponding (i) cyclic voltammetry (CV), and (ii) dark-field (DF) scattering spectra of single *e*NPoMs *vs* voltage applied. Inset shows SEM image of a representative *e*NPoM (80 nm Au NP coated with 20 nm polymer shell on Au substrate, scale bar is 100 nm). (iii) Time scan of normalized DF scattering spectra from a single *e*NPoM for 5 cycles. (iv) Reversible switching of coupled plasmon mode *vs* applied voltage. (v) Experimental DF scattering images of a single *e*NPoM nano-pixel for different redox states.

These core-shell NPs are fabricated by the same surfactant-assisted chemical oxidative polymerisation method as described in section 4.2 [80, 93, 98, 99]. 1.6 mL of a citrate-stabilised Au NPs (BBI Solutions) solution is concentrated, followed by the removal of the supernatant, and then mixed with the monomer (0.78 mL of 10 mM pyrrole or 14.5 mM 3,4-ethylenedioxythiophene) and surfactant (0.145 mL of 40 mM sodium dodecyl sulfate) solutions, and finally oxidant (0.69 mL of 19.1 mM ammonium persulfate) and 8.25 μL of 20 mM iron chloride (catalyst) solutions. The resulting polymer thickness is around 20 nm after incubation at room temperature overnight, and can be controlled by adjusting the amount of monomers in each coating procedure or by repeating the whole process.

Similar three-electrode electrochemical cells as Au@PANI are used for electrochemical control. The electrolyte is 0.5 M NaCl in 10 mM HCl for Au@PPY and 0.5 M NaCl aqueous solution for Au@PEDOT. Low pH environment helps PPY mitigate the occurrence of irreversible overoxidation [152, 153]. The redox state of the polymer shells is controlled by sweeping the voltage from -0.25 to 0.75 V for Au@PPY and from -0.6 to 0.6 V for Au@PEDOT (*vs* Ag/AgCl), with a scan rate of 50 mV/sec. Different from PANI, the cyclic voltammetry (CV) curves only show one set of oxidised (upper) and reduced peaks (lower) (Figure 6.1 i), which means only the fully oxidised and fully reduced states are resolved by electrochemical means. For Au@PEDOT, there is a set of small pre-peaks before the redox peaks, coming from the strongly trapped/released dopant ions [68, 154].

DF scattering spectra of single *e*NPoMs are simultaneously measured, and highly stable and reversible optical switchings are observed (Figure 6.1 ii-iv). The redox change of PPY gives a coupled-mode peak wavelength tuning from around 610 nm to 630 nm, and PEDOT changes from around 635 nm to 670 nm. These wavelength tuning ranges lie in longer wavelength region than PANI, making the colour dynamics hard to recognise by eye from their experimental DF images (Figure 6.1 v). A comparison of colour dynamics of *e*NPoMs made from these three polymers is shown in Figure 6.2. The colour dynamics of Au@PPY mainly reside in the reddish region and Au@PEDOT lies in the yellowish region. Although not as good as Au@PANI in colour dynamics so not ideal for display type of applications, Au@PPY and Au@PEDOT can function as switching-type devices [50, 51], such as single nanoparticle switches, from their absorption in the oxidised state.

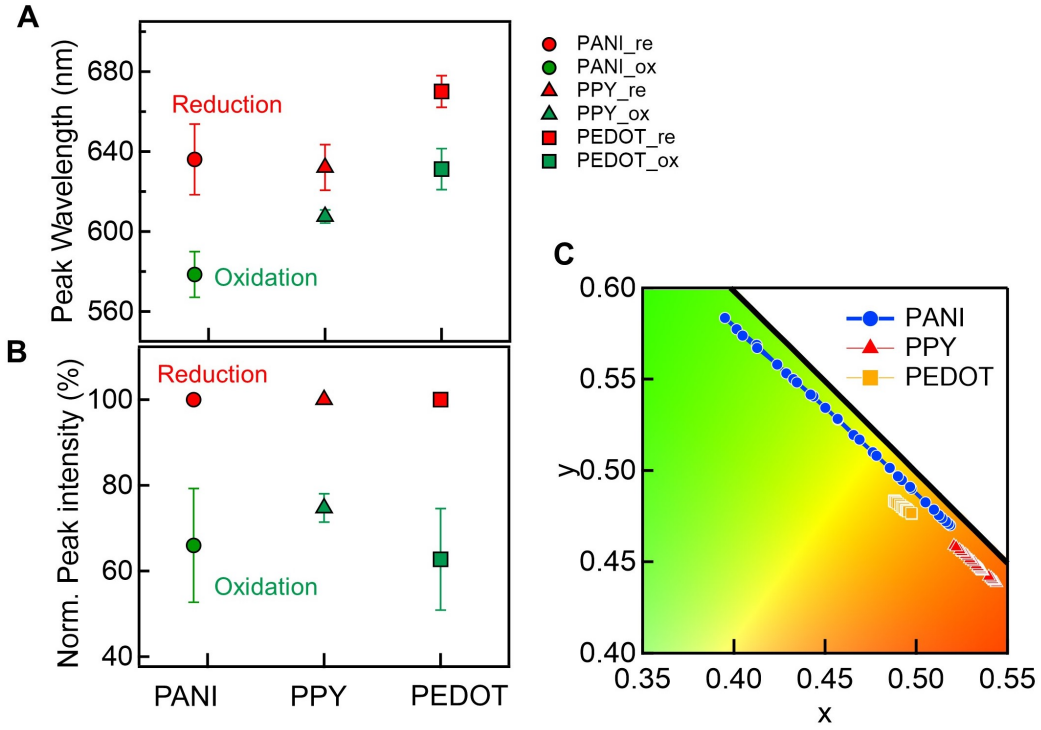

Fig. 6.2 Colour dynamics comparison of *e*NPoMs made from Au@PANI, Au@PPY and Au@PEDOT. (A) Optical tuning and (B) corresponding intensity switching of *e*NPoMs. (C) Associated colour gamut plots (CIE 1931 chromaticity).

In summary, Au@PPY and Au@PEDOT are successfully demonstrated with the *e*NPoM concept, although with less distinct colour dynamics than Au@PANI. Real-time in-situ monitoring of the polymer redox states still can be achieved by tracking the DF scattering changes at the single nanoparticle level, but it is not enough to track the two-step oxidative doping process because the CV curves cannot resolve two sets of redox peaks clearly. This is why Raman scattering is also a useful tool.

6.2 Tracking Redox State with SERS

Vibrational techniques such as Raman spectroscopy are useful for probing the conformational and structural changes at the molecular level, which can help monitor the variation of polymer redox states. The high field enhancement from the NPoM construct can enhance the Raman scattering, offering a possibility for resolving information not accessible by bulk CV measurements.

Table 6.1 Vibrational assignments of characteristic Raman bands for PPY, PEDOT and PANI

Polymers	Assignments	Wavenumbers/cm^{-1}
PPY [155–157]	Ring deformation associated with oxidation	930
	Ring deformation associated with reduction	970
	C-H in-plane deformation	1040
	C=C backbone stretching	1545-1585
PEDOT [158–160]	C–O–C deformation	1085
	C_β-$C_{\beta'}$ stretching	1340
	Symmetric C_α=C_β stretching	1403-1427
	Asymmetric C_α=C_β stretching	1490
PANI [161–163]	C-H in-plane bending	1180
	C∼$N^{+\bullet}$ stretching	1340
	C=N stretching	1480
	C=C stretching in quinone rings	1580
	C-C stretching in benzene rings	1620

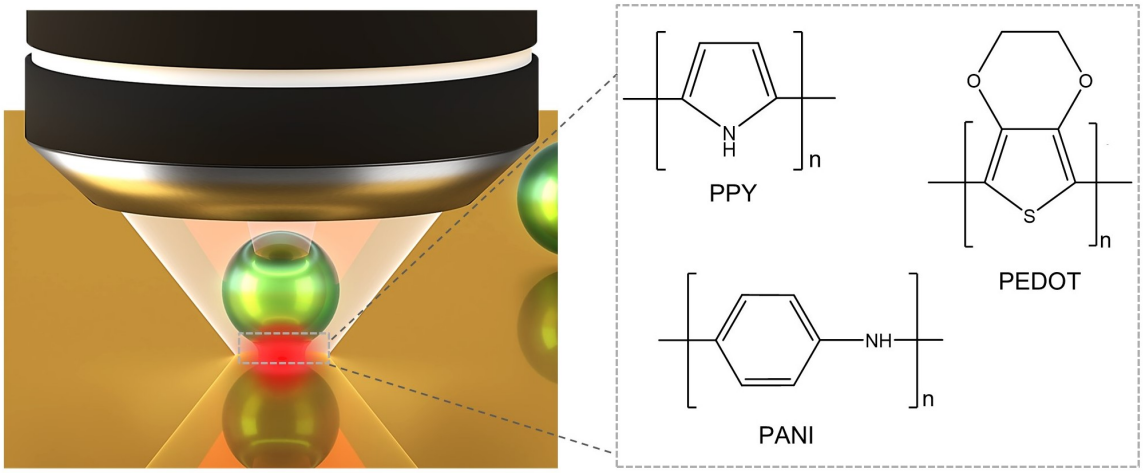

Fig. 6.3 Schematic of tracking redox states of different conductive polymers by *e*NPoM structure with surface-enhanced Raman spectroscopy (SERS).

In-situ SERS spectra are measured in real-time with the three different *e*NPoMs as introduced above (Figure 6.3). The measuring set-up is as discussed in section 3.1.2, and a 633 nm laser is used of power 100 μW. The changes of SERS spectra give detailed

insights into the conformational changes of polymer structure within the nanosized gaps during each redox cycle. Distinct vibrational assignments of the polymer bands during redox are summarised in Table 6.1. Compared to reference literature, the main peaks observed only have a slight downward shift, possibly indicating that the polymers are more crystallised or have longer conjugation length than their bulk counterparts [164–166].

Au@PEDOT

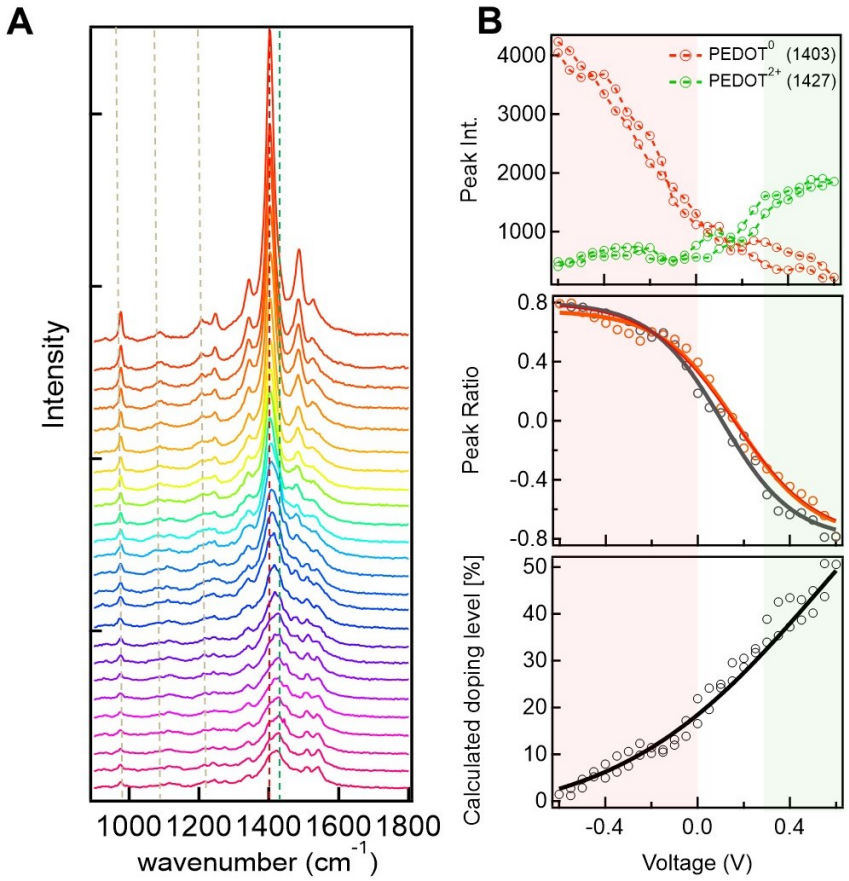

Fig. 6.4 SERS dynamics of *e*NPoMs made from Au@PEDOT. (A) SERS spectra when voltage is applied from -0.6 V → 0.6 V (top to bottom). (B) Decomposed peak dynamics of symmetric C_α=C_β stretching for reduced PEDOT segments ($PEDOT^0$, at 1403 cm^{-1}) and oxidised PEDOT segments ($PEDOT^{2+}$, at 1427 cm^{-1}) *vs* voltage applied. Top panel: corresponding peak intensities. Middle panel: the fractional difference of these two components. Bottom panel: calculated doping level. The red/green shaded regions indicate the dominance of $PEDOT^0$/$PEDOT^{2+}$ states. The solid lines are fitting by sigmoid functions.

The SERS spectra of PEDOT during oxidative doping are recorded in the 900-1800 cm^{-1} range, as shown in Figure 6.4. The most intense change of the PEDOT SERS spectra is clearly the peak around 1403-1427 cm^{-1}, assignable to symmetric C_α=C_β stretch vibrations of the PEDOT backbone. This peak continuously broadens and shifts from around 1403 cm^{-1} to 1427 cm^{-1} when voltage is applied from -0.6 V $\rightarrow$ 0.6 V.

Two separate bands can be decomposed from the peak[1]: one is the symmetric C_α=C_β stretch vibrations from the reduced (neutral) state of PEDOT segments ($PEDOT^0$) centred at 1403 cm^{-1}, while another one is due to the oxidised PEDOT segments ($PEDOT^{2+}$) centred at 1427 cm^{-1} [167]. The corresponding peak dynamics is shown in Figure 6.4 B. The peak ascribed to the $PEDOT^0$ (red curve) decreases by 95%±5% upon oxidation, while the peak due to $PEDOT^{2+}$ (green curve) increases by 74%±16% simultaneously, meaning an increase in the proportion of $PEDOT^{2+}$ to $PEDOT^0$ and explaining the broadening and shifting of the overlapped main peak. The two peaks overlap in 0.01 - 0.35 V, indicating the coexistence of reduced and oxidised forms of PEDOT (for fractional intensity difference of these two peaks, defined as $(I_{re} - I_{ox})/(I_{re} + I_{ox})$, see middle panel of Figure 6.4 B). This intermediate phase can be viewed as a feature of the $PEDOT^{1+}$ state (polarons) [155, 157, 168].

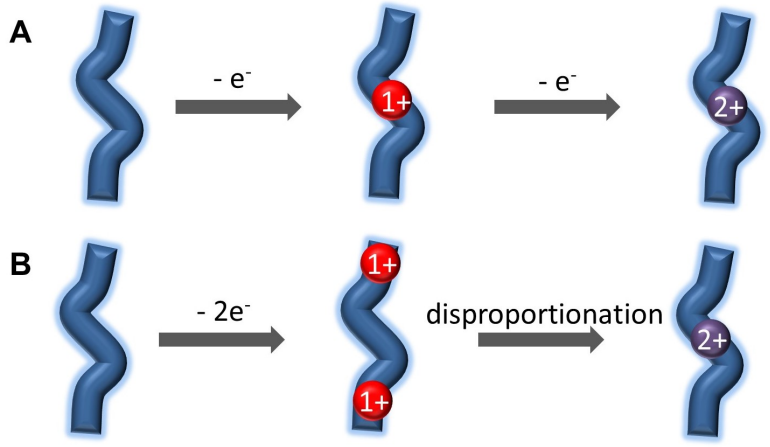

Fig. 6.5 Illustrations of two possible mechanisms for charge transport of conjugated conductive polymers upon oxidative doping. (A) Consecutive two-step charge transfer. The polymer strand goes from 0 $\rightarrow$ 1+ $\rightarrow$ 2+ state by losing electrons consecutively. (B) Disproportionation-type charge transfer. The polymer strand goes from 0 $\rightarrow$ 1+ by losing electrons, and two 1+ states quickly combine to form a 2+ state without extra charge transfer.

[1]Gaussian fitting is used with the multi-peak fitting module of Igor Pro 8 (WaveMetrics).

As described by the polaron-bipolaron model introduced in section 2.3.1, an electron is removed from the main chain of PEDOT in the early oxidation stage, with benzenoid-to-quinoid lattice deformation and diffusion of an anion ion from the electrolyte to stabilize the charge, termed a polaron or $PEDOT^{1+}$ state, which is followed by another electron removal to form the bipolaron or $PEDOT^{2+}$ state. This consecutive two-step oxidative doping process is illustrated in Figure 6.5 A. However, the corresponding CV cannot provide exact information about the $PEDOT^{1+} \rightarrow PEDOT^{2+}$ transformation, as only the $PEDOT^{0} \rightarrow PEDOT^{2+}$ transformation can be identified. This is possibly because $PEDOT^{2+}$ quickly forms directly by disproportionation of two $PEDOT^{1+}$ and does not require extra charge transfer [68, 156] (Figure 6.5 B). The formation of $PEDOT^{2+}$ is also more energically favourable than the transformation of $PEDOT^{1+} - e^{-} \rightarrow PEDOT^{2+}$ [66]. Here, the coexistence of reduced and oxidised features can be used to deduce the voltage range of $PEDOT^{1+}$. Other noticeable changes in the SERS spectra include splitting of the asymmetric C_{α}=C_{β} stretch band at 1490-1550 cm^{-1}, which happens at 0.01 V and coincides with the onset of the $PEDOT^{1+}$ state [158–160].

The shift of the symmetric C_{α}=C_{β} directly indicates the oxidation level of PEDOT. In addition, the doping levels during the redox cycle can be approximately estimated by the ratio of the intensities of decomposed $PEDOT^{0}$ and $PEDOT^{2+}$ peaks, through a correlation equation according to previous study [167]:

$$D = 11.49 \times (ln(I_{ox}/I_{re}) + 2.28) \tag{6.1}$$

where D is the percentage doping level, and I_{ox} and I_{re} are peak intensities of the oxidised and reduced structures, respectively. The doping level of PEDOT is thus observed to increase to up to 50% by electrochemical doping (bottom panel, Figure 6.4 B). This value is very high, possibly because the 20 nm thin polymer coating facilitates dopant diffusion.

Au@PPY

A similar analysis can be done with Au@PPY. The SERS spectra for Au@PPY from -0.25 V $\rightarrow$ 0.75V are shown in Figure 6.6, covering the 800–1750 cm^{-1} region.

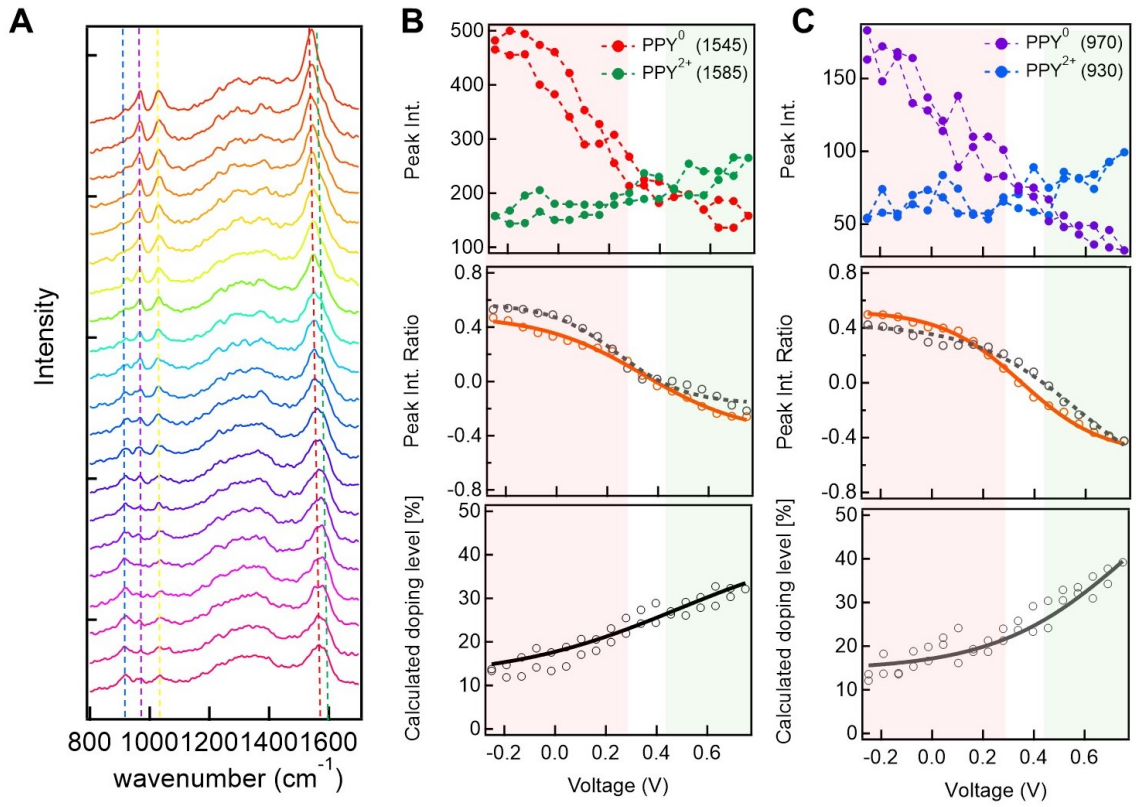

Fig. 6.6 SERS dynamics of *e*NPoMs made from Au@PPY. (A) SERS spectra when voltage is applied from -0.25 V → 0.75 V (top to bottom). Peak dynamics of (B) decomposed C=C stretching, and (C) ring deformation associated with reduced PPY segments (PPY^0) and oxidised PPY segments (PPY^{2+}), *vs* voltage applied. Top panel: corresponding peak intensities. Middle panel: the fractional difference of the two decomposed components. Bottom panel: calculated doping level. The red/green shaded regions indicate the dominance of PPY^0/PPY^{2+} states. The solid lines are fitting by sigmoid functions.

Clearly, the most intense peak for PPY is located at around 1500-1600 cm^{-1}, assigned to the C=C stretch vibrations of the PPY backbone. Similar to the symmetric C_α=C_β stretch vibrations of the PEDOT, C=C stretch vibrations of the PPY also broaden and shift to higher wavenumbers upon oxidation. In the reduced state (-0.25V), it displays a characteristic vibrational band at 1545 cm^{-1}, due to C=C backbone stretching of reduced PPY segments (PPY^0). This band shifts to around 1575 cm^{-1} when approaching oxidation (PPY^{2+}, 0.75 V). For a quantitative estimation, the overlapped double peaks are resolved into two component peaks located at 1545 cm^{-1} and 1575 cm^{-1}, respectively. The intensity changes *vs* applied voltage of these two component peaks are shown in Figure 6.6 B. In the reduced state, the 1545 cm^{-1} peak clearly

dominates. Its intensity starts to decrease upon oxidation, and 67%±15% switching is observed at 0.75 V. The 1575 cm^{-1} peak presents a reversed trend, which increases by 40%±22%, meaning that the PPY transforms gradually from PPY^0 to PPY^{2+}. These two peaks overlap in voltage region 0.27 - 0.41 V, implying that the reduced and oxidised forms of PPY coexist at this intermediate phase, which can be viewed as a feature of the PPY^{1+} state (polarons) [155, 157, 168]. The doping level of PPY can be estimated, assuming the same correlation equation as for PEDOT (bottom panel, Figure 6.6 B) [169]. Different from PEDOT, initially 13% PPY doping (oxidised) state is seen at -0.25 V, while 33%±2% doping level is observed at 0.75 V. Possible explanations could be the oxidative degradation of PPY by oxygen from the ambient environment [170, 171]. In contrast, PEDOT has excellent air stability and is more conductive [172], allowing for better switching ability.

The same trend can be observed in another pair of peaks located at 970 and 930 cm^{-1}, which are assigned to ring deformation modes associated with reduced state and oxidised states of PPY, respectively (Figure 6.6 C). These two bands also overlap in the same voltage range 0.27 - 0.41 V. Around 13% polymer is still in the oxidised state at -0.25 V and 39%±4% doping level is reached at 0.75 V, giving similar doping levels as calculated from the C=C peaks.

In summary, for PEDOT and PPY, the peak intensities and shifts of the main C=C backbone stretch vibrational bands in SERS spectra help to recognise the voltage region of the two-step oxidative doping process, which cannot be easily resolved from their corresponding CV curves. The polaron-bipolaron transformation ($1+ \leftrightarrow 2+$) can be tracked with the coexistence of reduced and oxidised vibrational spectral signatures. Both polymers exhibit clear switching of the SERS signals, which can be used to estimate quantitatively the doping level during their redox cycles. PEDOT presents better switching ability, higher doping level at oxidation than PPY, which is consistent with the extensive applications of PEDOT as a conductive material in commercial products [172].

Au@PANI

The two sets of redox peaks in the CV of Au@PANI clearly show a two-step oxidation process, facilitating the correlation between colour dynamics of *e*NPoMs and the charge states of PANI (see section 4.5). The SERS dynamics of Au@PANI is also measured as voltage is applied, covering the 1100-1700 cm^{-1} range (Figure 6.7).

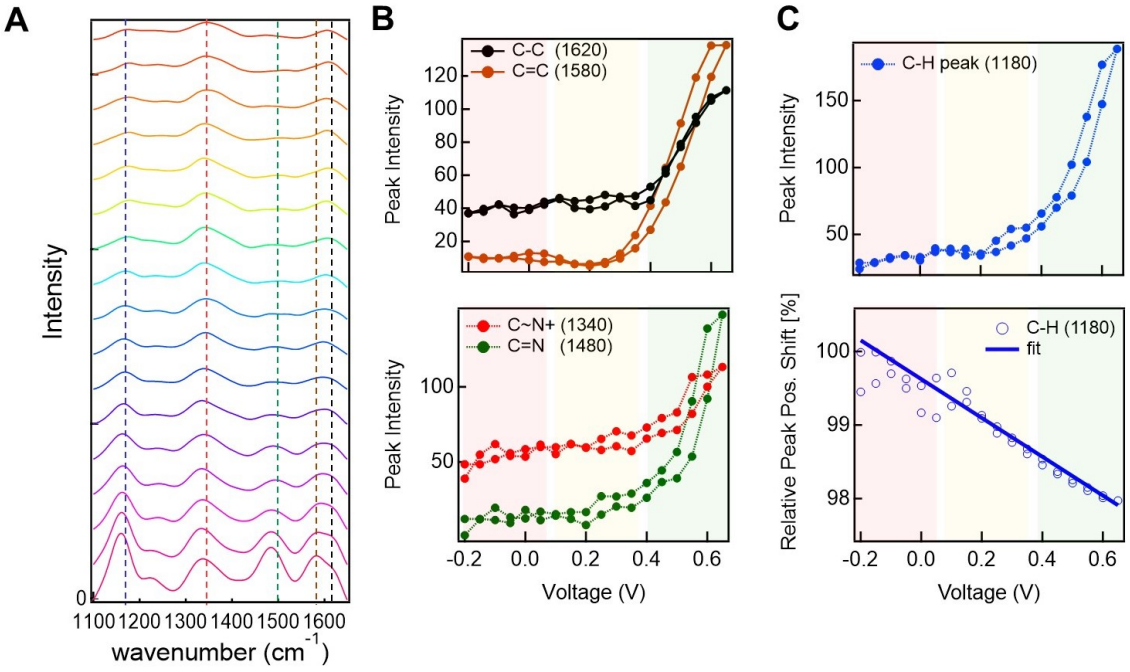

Fig. 6.7 SERS dynamics of *e*NPoMs made from Au@PANI. (A) SERS spectra when voltage is applied from -0.2 V → 0.6 V (top to bottom). (B) Peak intensities of C-C stretching at 1620 cm^{-1} and C=C stretching at 1580 cm^{-1} (top panel), and C∼$N^{+\bullet}$ stretching at 1340 cm^{-1} and C=N stretching at 1480 cm^{-1} (bottom panel) *vs* applied voltage. (C) Peak intensity of C-H in-plane bending and its relative peak shift from 1180 cm^{-1} (at -0.2 V), *vs* applied voltage. The solid line is a linear fit. The red/yellow/green shaded regions indicate $PANI^0$/$PANI^{1+}$/$PANI^{2+}$ states.

Three sets of bond changes are distinct during the redox cycle of PANI. The C-C and C=C bond stretch vibrations are most prominent, located at 1620 and 1580 cm^{-1}, respectively. They directly relate to the presence of benzene and quinone type rings. Another characteristic set of bands is at 1480 cm^{-1} for C=N stretching and 1340 cm^{-1} for C∼$N^{+\bullet}$ stretching. C=N bond stretch vibration is characteristic for oxidized PANI, while C∼$N^{+\bullet}$ stretching is an intermediate bond (between a single and a double) stretch vibration linked with protonated nitrogens [162, 163]. Different from PPY and PEDOT, the peak intensities of these bands all increase upon oxidation (Figure 6.7 B). This is because the laser excitation wavelength 633 nm comes into resonance with the oxidised forms due to the light absorption spectrum of PANI [161, 173], enhancing the Raman features, while also making the change of the reduced PANI during cycling less distinct. Use of shorter wavelength lasers such as 488 nm or 532 nm light will help detect the reduced form, but in practice, the plasmonic heating from interband absorption of gold might make the tiny amount of polymer in the gap easy to damage

during continuous measurement [174, 175]. However, the band at 1180 cm^{-1}, which is assignable to C-H in-plane bending associated with ring deformation can directly show the actual redox states of PANI, because it is a pendant mode away from the polymer chain and less influenced by charges on the nitrogens than the CC or CN backbone stretchings [163]. Although the peak intensity of the C-H bending vibrations is still resonantly enhanced upon oxidation, its peak shift presents a linear dependence on applied voltage (Figure 6.7 C), thus straightforwardly recording the oxidation states of PANI.

6.3 Summary

The concept of *e*NPoMs is demonstrated with different conjugated conductive polymers PPY and PEDOT. Highly reproducible optical switchings are also observed with dark-field spectroscopy in real-time, although their colour dynamics are not as extensive as PANI. In-situ Raman spectroscopy is used to explore the redox dynamics of nanosized conjugated conductive polymers in the gap. The conformational and structural changes of the C=C backbone stretch vibrations not only give insights into the 1+ state which is not easy to resolve from bulk CV measurements, but also allows for monitoring and quantitatively estimating the corresponding doping levels. For PANI, the strong resonant features of oxidation tuned to the 633 nm laser hinder the exploring of doping level, but the peak positions of external C-H vibrations can function as a marker for the overall oxidation state.

7. Conclusions and Outlook

Plasmonic colouration has been a hot research area in active plasmonics, but the heavy reliance on expensive lithographic techniques to fabricate complicated scattering nanostructures means it often remains in academia. The main goal of this thesis is trying to develop plasmonic nanostructures capable of active colouration without relying on high-cost nanofabrication.

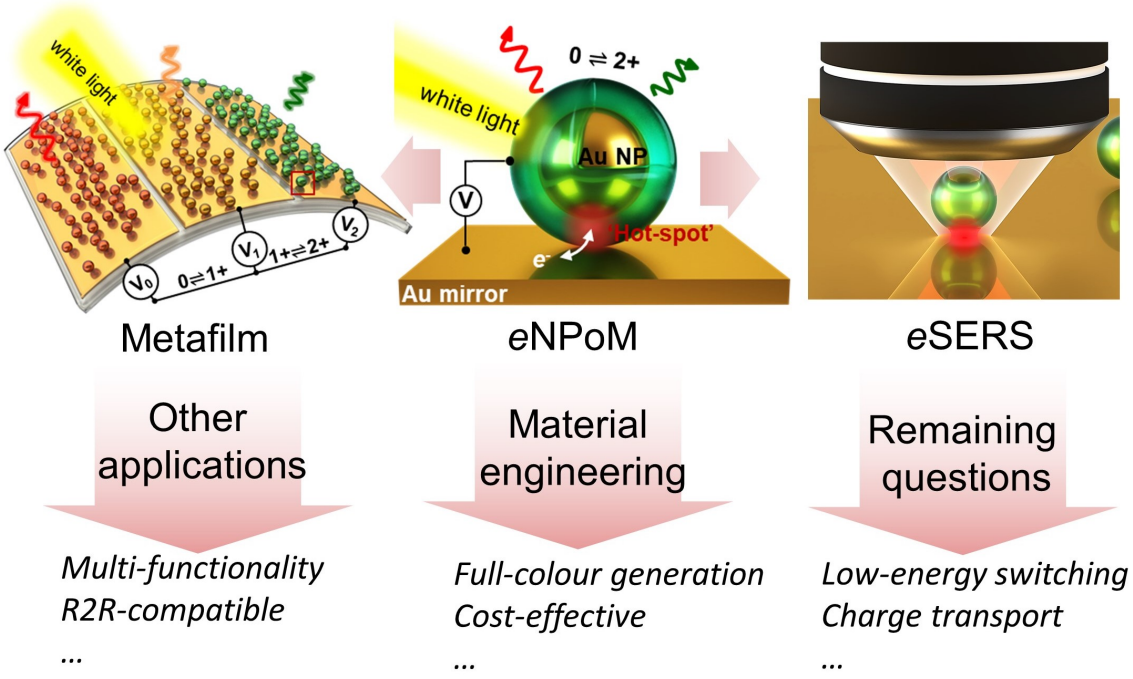

Fig. 7.1 Summary and possible future directions.

A new concept of plasmonic nanopixel is proposed in this thesis (Figure 7.1). It consists of positioning conductive polymer coated nanoparticles (gold in this work) onto a metal mirror, called an electrochromic nanoparticle on mirror (*e*NPoM). Light is confined inside the tiny gap between the nanoparticle and mirror, allowing for independent

tuning of the scattering, which delivers the concept of active nanopixels. By switching the charge state of the polymer shell electrically, the resonant scattering colour of the *e*NPoM can shift from red, yellow to green, in response to less than 1 V.

Scalable colour-changing plasmonic metafilms are further constructed with *e*NPoMs via 'lithography-free' methods such as meniscus-guided nanoparticle assembly and aerosol jet printing, taking active plasmonic colourations into the crucial domain capable of realistic scaling to roll-to-roll (R2R) for building-scale displays. Flexible patterned films are demonstrated with thin metal-coated plastic substrates, unlocking the potential of plasmonics for flexible/wearable displays. The directional optical effects coming from the *e*NPoMs with ultra-thin metal films are also presented and discussed, which are for the first time actively-controlled and create unusual new colour effects in different directions.

Surface-enhanced Raman spectroscopy with *e*NPoM constructs provide a powerful platform for tracking in-situ redox reactions of conductive polymers within individual plasmonic cavities. Optical dynamics of *e*NPoMs made with different conductive polymers are probed in real-time during redox cycling. The conformational changes of the polymers reveal the redox dynamics inside the tiny gap, providing rich information about the possible charge transport processes and doping levels.

Future Directions

More work can be done in the future on the following aspects:

⇒ **Material engineering**:

The current work of *e*NPoMs is based on gold nanoparticle cores and gold mirrors, which limits the possible colour ranges (gold nanoparticles cannot scatter blue light) and remains a barrier for large-scale production due to expense. Other plasmonic metals like silver or aluminium should be able to solve these two problems, which supports plasmonic resonance in shorter wavelength region and are much cheaper (Figure 7.2). The main challenge to use silver or aluminium is that they are less stable than gold electrochemically and tend to be oxidised. A possible solution is to have a protection layer such as SiO_2 on the nanoparticle core [136], and a polymer protection layer such as insulating poly-para-xylylene [176] on the mirror.

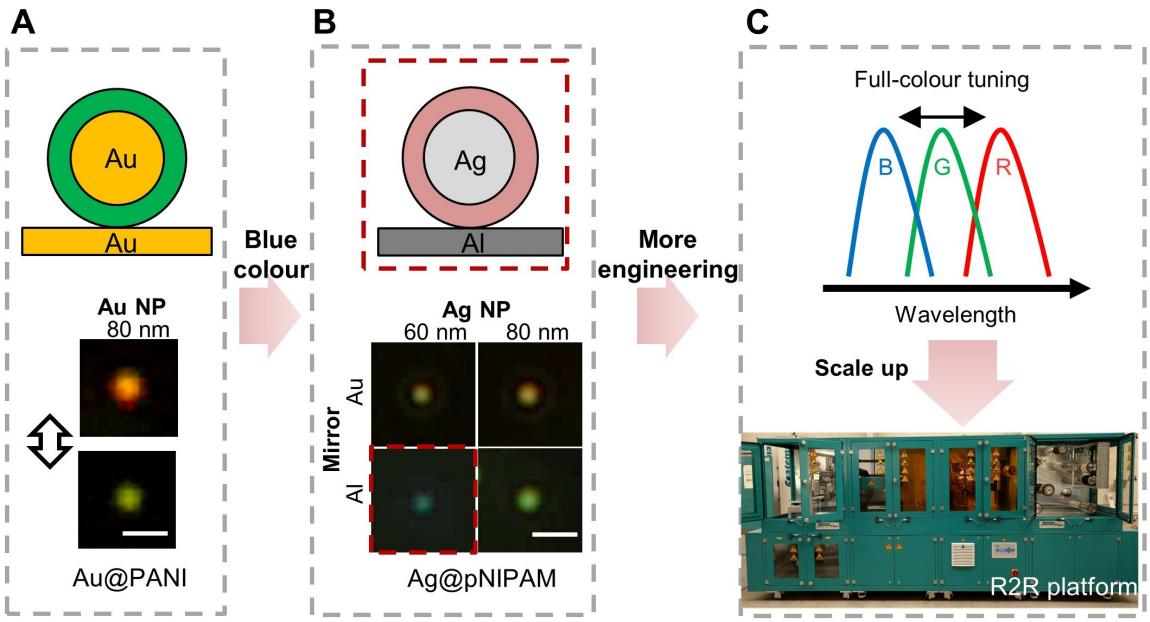

Fig. 7.2 Material engineering. (A) *e*NPoMs made from Au@PANI show red-to-green colour change. Bottom panel shows exemplary DF images of 80 nm Au@PANIs on Au mirror. (B) Possible material combination (Ag NPs on Al mirror) to get blue colour. Bottom panel shows exemplary DF images of 60 and 80 nm poly(N-isopropylacrylamide)-coated Ag NPs (Ag@pNIPAM) on Au/Al mirrors. Scale bar is 2 μm. (C) Further polymer engineering enables possible full-colour tuning, which can be extended with scale-up tool such as R2R platform. Photo of R2R platform courtesy of Dr Hsin-ling Liang.

Modifications of the polymers used is another plausible approach towards full-colour dynamics [177]. By blending/mixing different electrochromic polymers or modifying their chemical structures, extended colour dynamics can be achieved, with possibly better switching ability [53, 77].

⇒ **Other applications**:

In this work, I have demonstrated scalable patterned display applications of *e*NPoMs. The ease of fabrication makes other applications possible (Figure 7.3). Straightforward future examples can be such as flexible active matrix-pixelated devices, or electrochromic textiles made by *e*NPoM with conductive wires. Multifunctional devices are also possible, for example, PANI is pH-sensitive, so could function as pH sensors. Combination with other stimuli-responsive materials such as thermal-responsive poly(N-isopropylacrylamide) [178] or light-sensitive spiropyran [179], to make hybrid 'smart' materials, could be another possible route.

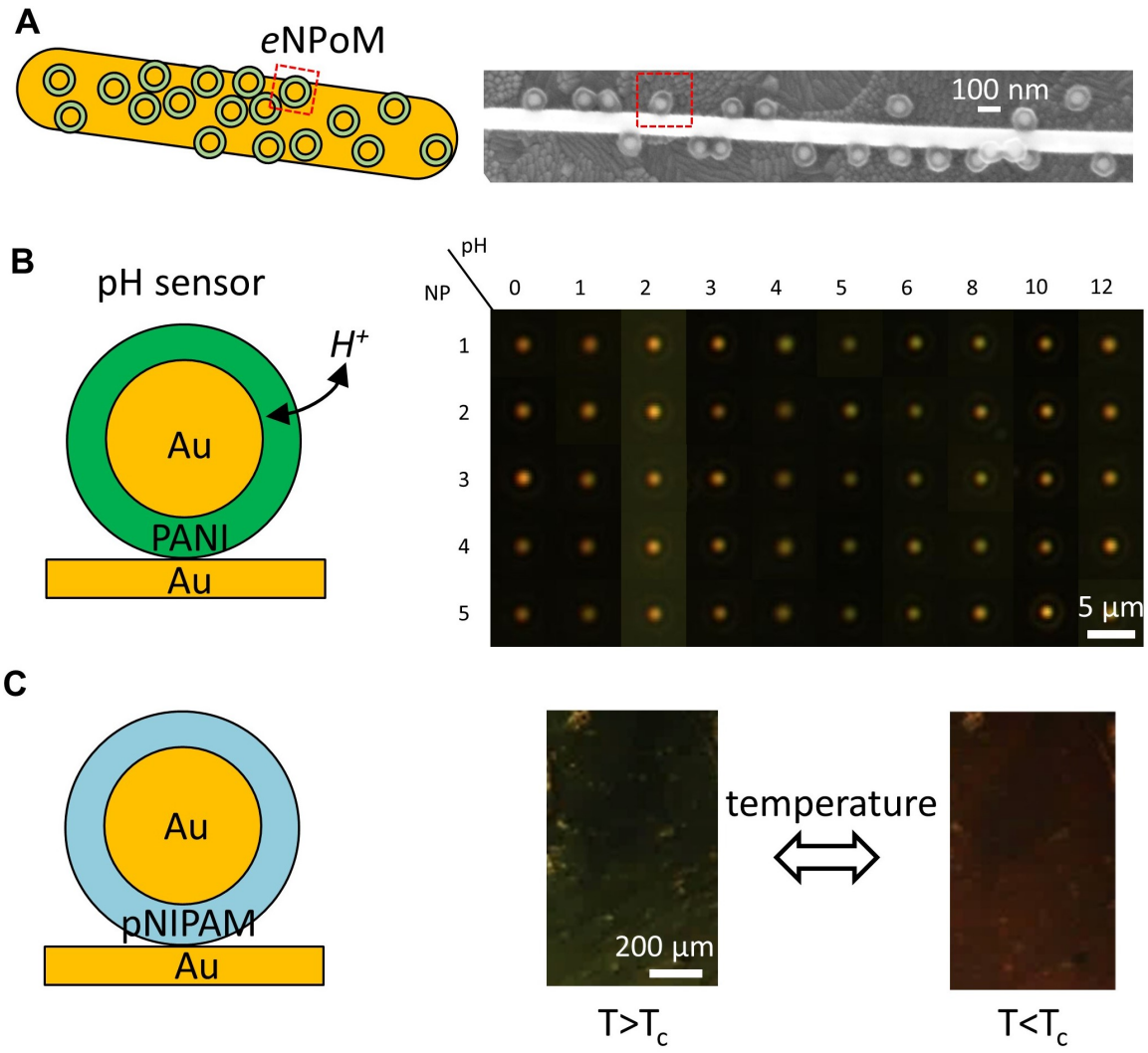

Fig. 7.3 Other possible applications. (A) Electrochromic textiles made by Au@PANIs on a metal wire, where the metal wire functions as a 'mirror'. The right panel shows an SEM image of Au@PANI NPs on Au nanowire from a tentative experiment. (B) *e*NPoM for pH sensing. The right panel shows DF images of 80 nm Au@PANI NPs at different pH levels. (C) Thermo-responsive metafilms made from 60 nm Au@pNIPAM NPs on Au mirror by meniscus-guided nanoparticle assembly. Thermally-induced gap distance change leads to the colour switching. Right panel shows BF images of this metafilm when heated to 42°C and cooled to 22°C, where the lower critical solution temperature $T_C = 32°C$.

⇒ **Remaining questions**:

Many questions encountered during my PhD are remained to be answered and worthwhile for further exploring, such as

→ what determines the intrinsic switching speed of conjugated conductive polymers and can we observe this optically in real-time with *e*NPoMs?
→ can we watch charge transport on a single polymer chain and measure the lowest energy needed for its switching?
→ can hot electrons from nanoparticles be transferred into the polymer and affect the polymer charge state?
Understanding these fundamental questions will be challenging, but definitely will reveal intriguing underlying physics and guide the research and development of new functional devices.

References

[1] Hiroshi Fudouzi. Tunable structural color in organisms and photonic materials for design of bioinspired materials. *Science and Technology of Advanced Materials*, 12(6):064704, 2011.

[2] Yuanjin Zhao, Zhuoying Xie, Hongcheng Gu, Cun Zhu, and Zhongze Gu. Bio-inspired variable structural color materials. *Chemical Society Reviews*, 41(8):3297–3317, 2012.

[3] J.D. Joannopoulos, R.D. Meade, and J.N Winn. *Photonic Crystals: Molding the Flow of Light*. Princeton University Press, 1995.

[4] Stefan A. Maier. *Plasmonics : fundamentals and applications*. Springer US, 2007.

[5] Anders Kristensen, Joel K.W. Yang, Sergey I. Bozhevolnyi, Stephan Link, Peter Nordlander, Naomi J. Halas, and N. Asger Mortensen. Plasmonic colour generation. *Nature Reviews Materials*, 2(1), 2016.

[6] Harald Ibach and Hans Lüth. *Solid-state physics: An introduction to principles of materials science*. Springer, 2009.

[7] P B Johnson and R W Christy. Optical constants of the noble metals. *Physical Review B*, 6(12):4370–4379, 1972.

[8] Sean Cormier. *Dynamic plasmonic systems with actuating nanotransducers*. PhD thesis, University of Cambridge, 2019.

[9] Craig F. Bohren and Donald R. Huffman. *Absorption and Scattering of Light by Small Particles*. John Wiley & Sons, Ltd, 1998.

[10] Emil Prodan, Corey Radloff, Naomi J Halas, and Peter Nordlander. A hybridization model for the plasmon response of complex nanostructures. *Science*, 302(5644):419–422, 2003.

[11] Peter Nordlander, Chris Oubre, Emil Prodan, K Li, and Mark I Stockman. Plasmon hybridization in nanoparticle dimers. *Nano Letters*, 4(5):899–903, 2004.

[12] Yu Huang, Qin Zhou, Mengjing Hou, Lingwei Ma, and Zhengjun Zhang. Nanogap effects on near- and far-field plasmonic behaviors of metallic nanoparticle dimers. *Physical Chemistry Chemical Physics*, 17(43):29293–29298, 2015.

[13] Jeremy J Baumberg, Javier Aizpurua, Maiken H Mikkelsen, and David R Smith. Extreme nanophotonics from ultrathin metallic gaps. *Nature Materials*, 18(7):668–678, 2019.

[14] Rohit Chikkaraddy, Bart De Nijs, Felix Benz, Steven J Barrow, Oren A Scherman, Edina Rosta, Angela Demetriadou, Peter Fox, Ortwin Hess, and Jeremy J Baumberg. Single-molecule strong coupling at room temperature in plasmonic nanocavities. *Nature*, 535(7610):127–130, 2016.

[15] Jan Mertens, Anna L. Eiden, Daniel O. Sigle, Fumin Huang, Antonio Lombardo, Zhipei Sun, Ravi S. Sundaram, Alan Colli, Christos Tserkezis, Javier Aizpurua, Silvia Milana, Andrea C. Ferrari, and Jeremy J. Baumberg. Controlling subnanometer gaps in plasmonic dimers using graphene. *Nano Letters*, 13(11):5033–5038, 2013.

[16] Quan Xiang, Zhiqin Li, Mengjie Zheng, Qing Liu, Yiqin Chen, Lan Yang, Tian Jiang, and Huigao Duan. Sensitive sers detection at the single-particle level based on nanometer-separated mushroom-shaped plasmonic dimers. *Nanotechnology*, 29(10):105301–105301, 2018.

[17] Kevin J Savage, Matthew M Hawkeye, Ruben Esteban, Andrei G Borisov, Javier Aizpurua, and Jeremy J Baumberg. Revealing the quantum regime in tunnelling plasmonics. *Nature*, 491(7425):574–577, 2012.

[18] Weiyang Li, Pedro H C Camargo, Xianmao Lu, and Younan Xia. Dimers of silver nanospheres: facile synthesis and their use as hot spots for surface-enhanced raman scattering. *Nano Letters*, 9(1):485–490, 2009.

[19] Rongchao Jin. Nanoparticle clusters light up in sers. *Angewandte Chemie*, 49(16):2826–2829, 2010.

[20] Deep Punj, Raju Regmi, Alexis Devilez, Robin Plauchu, Satish Babu Moparthi, Brian Stout, Nicolas Bonod, Herve Rigneault, and Jerome Wenger. Self-assembled nanoparticle dimer antennas for plasmonic-enhanced single-molecule fluorescence detection at micromolar concentrations. *ACS Photonics*, 2(8):1099–1107, 2015.

[21] Jan Mertens. *Image-coupled sub-nanometre plasmonic cavities*. PhD thesis, University of Cambridge, 2015.

[22] Felix Benz, Rohit Chikkaraddy, Andrew R Salmon, Hamid Ohadi, Bart De Nijs, Jan Mertens, Cloudy Carnegie, Richard Bowman, and Jeremy J Baumberg. Sers of individual nanoparticles on a mirror: Size does matter, but so does shape. *Journal of Physical Chemistry Letters*, 7(12):2264–2269, 2016.

[23] Bart De Nijs, Richard W Bowman, Lars O Herrmann, Felix Benz, Steve J Barrow, Jan Mertens, Daniel O Sigle, Rohit Chikkaraddy, Anna Eiden, Andrea Ferrari, A Scherman, and Jeremy J Baumberg. Unfolding the contents of sub-nm plasmonic gaps using normalising plasmon resonance spectroscopy †. *Faraday Discussions*, 00:1–9, 2015.

[24] Felix Benz, Christos Tserkezis, Lars O Herrmann, Bart De Nijs, Alan Sanders, Daniel O Sigle, Laurynas Pukenas, Stephen D Evans, Javier Aizpurua, and Jeremy J Baumberg. Nanooptics of molecular-shunted plasmonic nanojunctions. *Nano Letters*, 15(1):669–674, 2015.

[25] Felix Benz, Mikolaj K Schmidt, Alexander Dreismann, Rohit Chikkaraddy, Yao Zhang, Angela Demetriadou, Cloudy Carnegie, Hamid Ohadi, Bart De Nijs, Ruben Esteban, Javier Aizpurua, and Jeremy J Baumberg. Single-molecule optomechanics in "picocavities". *Science*, 354(6313):726–729, nov 2016.

[26] Jack J Mock, Ryan T Hill, Aloyse Degiron, Stefan Zauscher, Ashutosh Chilkoti, and David R Smith. Distance-dependent plasmon resonant coupling between a gold nanoparticle and gold film. *Nano Letters*, 8(8):2245–2252, 2008.

[27] Sean Cormier, Tao Ding, Vladimir Turek, and Jeremy J. Baumberg. Actuating Single Nano-Oscillators with Light. *Advanced Optical Materials*, 6(6):1–5, 2018.

[28] Tao Ding, Jan Mertens, Anna Lombardi, Oren A. Scherman, and Jeremy J. Baumberg. Light-Directed Tuning of Plasmon Resonances via Plasmon-Induced Polymerization Using Hot Electrons. *ACS Photonics*, 4(6):1453–1458, 2017.

[29] Felix Benz, Mikolaj K Schmidt, A Dreismann, Rohit Chikkaraddy, Yao Zhang, Angela Demetriadou, Cloudy Carnegie, Hamid Ohadi, Bart De Nijs, Ruben Esteban, et al. Single-molecule optomechanics in "picocavities". *Science*, 354(6313):726–729, 2016.

[30] Rohit Chikkaraddy, Bart De Nijs, Felix Benz, Steven J Barrow, Oren A Scherman, Edina Rosta, Angela Demetriadou, Peter Fox, Ortwin Hess, and Jeremy J Baumberg. Single-molecule strong coupling at room temperature in plasmonic nanocavities. *Nature*, 535(7610):127–130, 2016.

[31] Charlie Readman, Bart De Nijs, István Szabó, Angela Demetriadou, Ryan Greenhalgh, Colm Durkan, Edina Rosta, Oren A Scherman, and Jeremy J Baumberg. Anomalously large spectral shifts near the quantum tunnelling limit in plasmonic rulers with subatomic resolution. *Nano letters*, 19(3):2051–2058, 2019.

[32] Vladimir A. Turek, Rohit Chikkaraddy, Sean Cormier, Bill Stockham, Tao Ding, Ulrich F. Keyser, and Jeremy J. Baumberg. Thermo-Responsive Actuation of a DNA Origami Flexor. *Advanced Functional Materials*, 1706410:1–7, 2018.

[33] Tao Ding, Ventsislav K. Valev, Andrew R. Salmon, Chris J. Forman, Stoyan K. Smoukov, Oren A. Scherman, Daan Frenkel, and Jeremy J. Baumberg. Light-induced actuating nanotransducers. *Proceedings of the National Academy of Sciences*, 113(20):5503–5507, 2016.

[34] Tao Ding, Jan Mertens, Anna Lombardi, Oren A. Scherman, and Jeremy J. Baumberg. Light-Directed Tuning of Plasmon Resonances via Plasmon-Induced Polymerization Using Hot Electrons. *ACS Photonics*, 4(6):1453–1458, 2017.

[35] Cloudy Carnegie, Jack Griffiths, Bart De Nijs, Charlie Readman, Rohit Chikkaraddy, William D Deacon, Yao Zhang, Istvan Szabo, Edina Rosta, Javier Aizpurua, et al. Room-temperature optical picocavities below 1 nm3 accessing single-atom geometries. *Journal of Physical Chemistry Letters*, 9(24):7146–7151, 2018.

[36] Daniel O. Sigle, Elaine Perkins, Jeremy J. Baumberg, and Sumeet Mahajan. Reproducible deep-UV SERRS on aluminum nanovoids. *Journal of Physical Chemistry Letters*, 4(9):1449–1452, 2013.

[37] I C Freestone, N D Meeks, Margaret Sax, and Catherine Higgitt. The lycurgus cup - a roman nanotechnology. *Gold Bulletin*, 40(4):270–277, 2007.

[38] Stephan Link and Mostafa A Elsayed. Optical properties and ultrafast dynamics of metallic nanocrystals. *Annual Review of Physical Chemistry*, 54(1):331–366, 2003.

[39] Andrea E Schlather, Paul Gieri, Michael B Robinson, Silvia A Centeno, and Alejandro Manjavacas. Nineteenth-century nanotechnology: The plasmonic properties of daguerreotypes. *Proceedings of the National Academy of Sciences of the United States of America*, 116(28):13791–13798, 2019.

[40] Ting Xu, Yi-Kuei Wu, Xiangang Luo, and L. Jay Guo. Plasmonic nanoresonators for high-resolution colour filtering and spectral imaging. *Nature Communications*, 1(5):1–5, 2010.

[41] Karthik Kumar, Huigao Duan, Ravi S. Hegde, Samuel C.W. Koh, Jennifer N. Wei, and Joel K.W. Yang. Printing colour at the optical diffraction limit. *Nature Nanotechnology*, 7(9):557–561, 2012.

[42] Jeppe Sandvik Clausen, Emil Hojlundnielsen, Alexander Bruun Christiansen, Sadegh Yazdi, Meir Grajower, Hesham Taha, Uriel Levy, Anders Kristensen, and N Asger Mortensen. Plasmonic metasurfaces for coloration of plastic consumer products. *Nano Letters*, 14(8):4499–4504, 2014.

[43] Lei Shao, Xiaolu Zhuo, and Jianfang Wang. Advanced Plasmonic Materials for Dynamic Color Display. *Advanced Materials*, 1704338:1–18, 2017.

[44] Fei Cheng, Jie Gao, Ting S Luk, and Xiaodong Yang. Structural color printing based on plasmonic metasurfaces of perfect light absorption. *Scientific Reports*, 5(1):11045–11045, 2015.

[45] Stephen Y. Chou, Peter R. Krauss, and Preston J. Renstrom. Imprint of sub-25 nm vias and trenches in polymers. *Applied Physics Letters*, 67(1995):3114, 1995.

[46] Nazrin Kooy, Khairudin Mohamed, Lee Tze Pin, and Ooi Su Guan. A review of roll-to-roll nanoimprint lithography. *Nanoscale Research Letters*, 9(1):320–320, 2014.

[47] Hans Fredriksson, Yury Alaverdyan, Alexander Dmitriev, Christoph Langhammer, Duncan S Sutherland, Michael Zach, and Bengt Herbert Kasemo. Hole–mask colloidal lithography. *Advanced Materials*, 19(23):4297–4302, 2007.

[48] Hironori Nagai, Austen Poteet, Xu A Zhang, and Chih-Hao Chang. Three-dimensional colloidal interference lithography. *Nanotechnology*, 28(12):125302, 2017.

[49] Ting Xu, Erich C. Walter, Amit Agrawal, Christopher Bohn, Jeyavel Velmurugan, Wenqi Zhu, Henri J. Lezec, and A. Alec Talin. High-contrast and fast electrochromic switching enabled by plasmonics. *Nature Communications*, 7:1–6, 2016.

[50] Kunli Xiong, Gustav Emilsson, Ali Maziz, Xinxin Yang, Lei Shao, Edwin W.H. Jager, and Andreas B. Dahlin. Plasmonic Metasurfaces with Conjugated Polymers for Flexible Electronic Paper in Color. *Advanced Materials*, 28(45):9956–9960, 2016.

[51] Kunli Xiong, Daniel Tordera, Gustav Emilsson, Oliver Olsson, Ulrika Linderhed, Magnus P. Jonsson, and Andreas B. Dahlin. Switchable Plasmonic Metasurfaces with High Chromaticity Containing only Abundant Metals. *Nano Letters*, 17(11):7033–7039, 2017.

[52] Peiman Hosseini, C. David Wright, and Harish Bhaskaran. An optoelectronic framework enabled by low-dimensional phase-change films. *Nature*, 511(7508):206–211, 2014.

[53] Prakash R Somani and S Radhakrishnan. Electrochromic materials and devices: present and future. *Materials Chemistry and Physics*, 77(1):117–133, 2003.

[54] Roger J. Mortimer. Electrochromic materials. *Annual Review of Materials Research*, 41(241-268), March 2011.

[55] Avni A Argun, Pierrehenri Aubert, Barry C Thompson, Irina Schwendeman, Carleton L Gaupp, Jungseek Hwang, Nicholas J Pinto, D B Tanner, A G Macdiarmid, and John R Reynolds. Multicolored electrochromism in polymers: Structures and devices. *Chemistry of Materials*, 16(23):4401–4412, 2004.

[56] Guoping Wang, Xuechen Chen, Sheng Liu, Chingping Wong, and Sheng Chu. Mechanical Chameleon through Dynamic Real-Time Plasmonic Tuning. *ACS Nano*, 10(2):1788–1794, 2016.

[57] Chad P. Byers, Hui Zhang, Dayne F. Swearer, Mustafa Yorulmaz, Benjamin S. Hoener, Da Huang, Anneli Hoggard, Wei Shun Chang, Paul Mulvaney, Emilie Ringe, Naomi J. Halas, Peter Nordlander, Stephan Link, and Christy F. Landes. From tunable core-shell nanoparticles to plasmonic drawbridges: Active control of nanoparticle optical properties. *Science Advances*, 1(11):1–10, 2015.

[58] Bastiaan Molleman and Tjisse Hiemstra. Time, pH, and size dependency of silver nanoparticle dissolution: The road to equilibrium. *Environmental Science: Nano*, 4(6):1314–1327, 2017.

[59] Yiyang Li, Jorik Van De Groep, A Alec Talin, and Mark L Brongersma. Dynamic tuning of gap plasmon resonances using a solid-state electrochromic device. *Nano Letters*, 19(11):7988–7995, 2019.

[60] Nina Jiang, Xiaolu Zhuo, and Jianfang Wang. Active Plasmonics: Principles, Structures, and Applications. *Chemical Reviews*, 118(6):3054–3099, 2018.

[61] Kunli Xiong, Daniel Tordera, Magnus P. Jonsson, and Andreas B. Dahlin. Active control of plasmonic colors: Emerging display technologies. *Reports on Progress in Physics*, 82(2), 2019.

[62] Martien A. Cohen Stuart, Wilhelm T. S. Huck, Jan Genzer, Marcus Müller, Christopher Ober, Manfred Stamm, Gleb B. Sukhorukov, Igal Szleifer, Vladimir V. Tsukruk, Marek Urban, Françoise Winnik, Stefan Zauscher, Igor Luzinov, and Sergiy Minko. Emerging applications of stimuli-responsive polymer materials. *Nature Materials*, 9(2):101, jan 2010.

[63] Ihor Tokarev and Sergiy Minko. Tunable plasmonic nanostructures from noble metal nanoparticles and stimuli-responsive polymers. *Soft Matter*, 8(22):5980, 2012.

[64] Thanhhai Le, Yukyung Kim, and Hyeonseok Yoon. Electrical and electrochemical properties of conducting polymers. *Polymers*, 9(4):150, 2017.

[65] Richard Balint, Nigel J. Cassidy, and Sarah H. Cartmell. Conductive polymers: Towards a smart biomaterial for tissue engineering. *Acta Biomaterialia*, 10(6):2341–2353, 2014.

[66] Jeanluc Bredas and G Bryan Street. Polarons, bipolarons, and solitons in conducting polymers. *Accounts of Chemical Research*, 18(10):309–315, 1985.

[67] A O Patil, A J Heeger, and Fred Wudl. Optical properties of conducting polymers. *Chemical Reviews*, 88(1):183–200, 1988.

[68] Jurgen Heinze, Bernardo A Frontanauribe, and Sabine Ludwigs. Electrochemistry of conducting polymers: persistent models and new concepts. *Chemical Reviews*, 110(8):4724–4771, 2010.

[69] Pinar Camurlu. Polypyrrole derivatives for electrochromic applications. *RSC Advances*, 4(99):55832–55845, 2014.

[70] J C Lacroix, K K Kanazawa, and A Diaz. Polyaniline: A very fast electrochromic material. *Journal of The Electrochemical Society*, 136(5):1308–1313, 1989.

[71] H. Okuzaki and I. Kubota. Electrical and mechanical properties of poly(p-phenylene) films prepared by electrochemical polymerisation. *Synthetic Metals*, 153(1-3):161–164, 2005.

[72] Jaroslav Stejskal, Pavel Kratochvil, and A D Jenkins. The formation of polyaniline and the nature of its structures. *Polymer*, 37(2):367–369, 1996.

[73] Jaroslav Stejskal, Irina Sapurina, and Miroslava Trchova. Polyaniline nanostructures and the role of aniline oligomers in their formation. *Progress in Polymer Science*, 35(12):1420–1481, 2010.

[74] Edward Song and Jin-Woo Choi. Conducting Polyaniline Nanowire and Its Applications in Chemiresistive Sensing. *Nanomaterials*, 3(3):498–523, 2013.

[75] Irina Sapurina and Jaroslav Stejskal. The mechanism of the oxidative polymerization of aniline and the formation of supramolecular polyaniline structures. *Polymer International*, 57(12):1295–1325, 2008.

[76] W S Huang and A G Macdiarmid. Optical properties of polyaniline. *Polymer*, 34(9):1833–1845, 1993.

[77] Gagan Kaur, Raju Adhikari, Peter Cass, Mark Bown, and Pathiraja A Gunatillake. Electrically conductive polymers and composites for biomedical applications. *RSC Advances*, 5(47):37553–37567, 2015.

[78] Y T Kim, D L Allara, R W Collins, and K Vedam. Real-time spectroscopic ellipsometry study of theelectrochemical deposition of polypyrrole thin films. *Thin Solid Films*, pages 350–360, 1990.

[79] Barbero Cesar and Kotz Rudiger. Nanoscale Dimensional Changes and Optical Properties of Polyaniline Measured by In Situ Spectroscopic Ellipsometry. *Journal of The Electrochemical Society*, 141(4):859–865, 1994.

[80] Jing Zhou, Sajanlal R Panikkanvalappil, Saewon Kang, Shengtao Yu, Shuaidi Zhang, Mostafa A Elsayed, and Vladimir V Tsukruk. Enhanced electrochemical dark-field scattering modulation on a single hybrid core–shell nanostructure. *Journal of Physical Chemistry C*, 123(46):28343–28352, 2019.

[81] C. V. Raman and K. S. Krishnan. A new type of secondary radiation. *Nature*, 124(3048):501–502, 1928.

[82] E. C. Le Ru and P. G. Etchegoin. Single-molecule surface-enhanced Raman spectroscopy. *Annual Review of Physical Chemistry*, 63(1):65–87, 2012.

[83] R. L. McCreery. *Raman Spectroscopy for Chemical Analysis*. Wiley, 2005.

[84] P. L. Stiles, J. A. Dieringer, N. C. Shah, and R. P. Van Duyne. Surface-enhanced Raman spectroscopy. *Annual Review of Analytical Chemistry*, 1(1):601–626, 2008.

[85] Sebastian Schlucker. Surface-enhanced raman spectroscopy: Concepts and chemical applications. *Angewandte Chemie*, 53(19):4756–4795, 2014.

[86] E C Le Ru, E Blackie, M Meyer, and P G Etchegoin. Surface enhanced raman scattering enhancement factors: A comprehensive study. *Journal of Physical Chemistry C*, 111(37):13794–13803, 2007.

[87] E. Le Ru and P. Etchegoin. *Principles of Surface Enhanced Raman Spectroscopy and related plasmonic effects*. Elsevier, 2009.

[88] W Kiefer. The raman effect—a unified treatment of the theory of raman scattering by molecules. derek a. long, john wiley & sons, ltd., 2002, pp 597. isbn 0-471-49028-8. *Journal of Raman Spectroscopy*, 34(2):180–180, 2003.

[89] Jialong Peng, Hyeon-Ho Jeong, Qianqi Lin, Sean Cormier, Hsin Ling Liang, Michael F.L. De Volder, Silvia Vignolini, and Jeremy J. Baumberg. Scalable electrochromic nanopixels using plasmonics. *Science Advances*, 5(5):1–9, 2019.

[90] Molly M. Miller and Anne A. Lazarides. Sensitivity of metal nanoparticle surface plasmon resonance to the dielectric environment. *Journal of Physical Chemistry B*, 109(46):21556–21565, 2005.

[91] M. Wuttig, H. Bhaskaran, and T. Taubner. Phase-change materials for non-volatile photonic applications. *Nature Photonics*, 11(8):465–476, 2017.

[92] Wolfgang Knoll. Optical Properties of Polymers. In *Materials Science and Technology*. Wiley-VCH Verlag GmbH & Co. KGaA, Weinheim, sep 2006.

[93] Wenzheng Lu, Nina Jiang, and Jianfang Wang. Active Electrochemical Plasmonic Switching on Polyaniline-Coated Gold Nanocrystals. *Advanced Materials*, 29(8), 2017.

[94] Wenqi Zhu, Ruben Esteban, Andrei G Borisov, Jeremy J Baumberg, Peter Nordlander, Henri J Lezec, Javier Aizpurua, and Kenneth B Crozier. Quantum mechanical effects in plasmonic structures with subnanometre gaps, 2016.

[95] Antoine Moreau, Cristian Ciracì, Jack J. Mock, David R. Smith, Ryan T. Hill, Ashutosh Chilkoti, Qian Wang, and Benjamin J. Wiley. Controlled-reflectance surfaces with film-coupled colloidal nanoantennas. *Nature*, 492(7427):86–89, 2012.

[96] Cesar A Barbero and R Kotz. Nanoscale dimensional changes and optical properties of polyaniline measured by in situ spectroscopic ellipsometry. *Journal of The Electrochemical Society*, 141(4):859–865, 1994.

[97] Jon W Stewart, Gleb M Akselrod, David R Smith, and Maiken H Mikkelsen. Toward multispectral imaging with colloidal metasurface pixels. *Advanced Materials*, 29(6):1602971, 2017.

[98] Ju Won Jeon, Petr A. Ledin, Jeffrey A. Geldmeier, James F. Ponder, Mahmoud A. Mahmoud, Mostafa El-Sayed, John R. Reynolds, and Vladimir V. Tsukruk. Electrically Controlled Plasmonic Behavior of Gold Nanocube@Polyaniline Nanostructures: Transparent Plasmonic Aggregates. *Chemistry of Materials*, 28(8):2868–2881, 2016.

[99] Shuangxi Xing, Li Huey Tan, Miaoxin Yang, Ming Pan, Yunbo Lv, Qinghu Tang, Yanhui Yang, and Hongyu Chen. Highly controlled core/shell structures: tunable conductive polymer shells on gold nanoparticles and nanochains. *Journal of Materials Chemistry*, 19(20):3286, 2009.

[100] Tao Zhang, Haoyuan Qi, Zhongquan Liao, Yehu David Horev, Luis Antonio Panes-Ruiz, Petko St Petkov, Zhe Zhang, Rishi Shivhare, Panpan Zhang, Kejun Liu, et al. Engineering crystalline quasi-two-dimensional polyaniline thin film with enhanced electrical and chemiresistive sensing performances. *Nature communications*, 10(1):1–9, 2019.

[101] Martin Hegner, Peter Wagner, and Giorgio Semenza. Ultralarge atomically flat template-stripped Au surfaces for scanning probe microscopy. *Surface Science*, 291(1-2):39–46, jul 1993.

[102] G. Di Martino, V. A. Turek, A. Lombardi, I. Szabó, B. De Nijs, A. Kuhn, E. Rosta, and J. J. Baumberg. Tracking Nanoelectrochemistry Using Individual Plasmonic Nanocavities. *Nano Letters*, 17(8):4840–4845, 2017.

[103] Bart De Nijs, Felix Benz, Steven J. Barrow, Daniel O. Sigle, Rohit Chikkaraddy, Aniello Palma, Cloudy Carnegie, Marlous Kamp, Ravishankar Sundararaman, Prineha Narang, Oren A. Scherman, and Jeremy J. Baumberg. Plasmonic tunnel junctions for single-molecule redox chemistry. *Nature Communications*, 8(1):994, dec 2017.

[104] Li Cui, Bo Liu, David Vonlanthen, Marcel Mayor, Yongchun Fu, Jian Feng Li, and Thomas Wandlowski. In situ gap-mode raman spectroscopy on single-crystal Au(100) electrodes: Tuning the torsion angle of 4,4'-biphenyldithiols by an electrochemical gate field. *Journal of the American Chemical Society*, 133(19):7332–7335, 2011.

[105] Linan Zhou, Dayne F Swearer, Chao Zhang, Hossein Robatjazi, Hangqi Zhao, Luke Henderson, Liangliang Dong, Phillip Christopher, Emily A Carter, Peter Nordlander, et al. Quantifying hot carrier and thermal contributions in plasmonic photocatalysis. *Science*, 362(6410):69–72, 2018.

[106] Emiliano Cortés, Wei Xie, Javier Cambiasso, Adam S Jermyn, Ravishankar Sundararaman, Prineha Narang, Sebastian Schlücker, and Stefan A Maier. Plasmonic hot electron transport drives nano-localized chemistry. *Nature Communications*, 8, 2017.

[107] Noémie Elgrishi, Kelley J. Rountree, Brian D. McCarthy, Eric S. Rountree, Thomas T. Eisenhart, and Jillian L. Dempsey. A Practical Beginner's Guide to Cyclic Voltammetry. *Journal of Chemical Education*, 95(2):197–206, 2018.

[108] Harsha S. Kolla, Sumedh P. Surwade, Xinyu Zhang, Alan G. MacDiarmid, and Sanjeev K. Manohar. Absolute molecular weight of polyaniline. *Journal of the American Chemical Society*, 127(48):16770–16771, 2005.

[109] James Davis, Yi Hsuan Hsieh, and Hung Chi Lee. Humans perceive flicker artifacts at 500 Hz. *Scientific Reports*, 5(1):7861, jul 2015.

[110] Jialong Peng, Hyeon-Ho Jeong, Michael Smith, Rohit Chikkaraddy, Qianqi Lin, Hsin Ling Liang, Michael F.L. De Volder, Silvia Vignolini, Sohini Kar-Narayan, and Jeremy J. Baumberg. Fully-printed flexible plasmonic metafilms with directional color dynamics. *Advanced Science*, 2020.

[111] Laurent Malaquin, Tobias Kraus, Heinz Schmid, Emmanuel Delamarche, and Heiko Wolf. Controlled particle placement through convective and capillary assembly. *Langmuir*, 23(23):11513–11521, 2007.

[112] Songbo Ni, Jessica Leemann, Heiko Wolf, and Lucio Isa. Insights into mechanisms of capillary assembly. *Faraday Discuss.*, 181:225–242, 2015.

[113] Philip Born, Susanne Blum, Andres Munoz, and Tobias Kraus. Role of the meniscus shape in large-area convective particle assembly. *Langmuir*, 27(14):8621–8633, 2011.

[114] Inki Kim, Gwanho Yoon, Jaehyuck Jang, Patrice Genevet, Ki Tae Nam, and Junsuk Rho. Outfitting Next Generation Displays with Optical Metasurfaces. *ACS Photonics*, 5(10):3876–3895, 2018.

[115] Tobias Kraus, Laurent Malaquin, Heinz Schmid, Walter Riess, Nicholas D. Spencer, and Heiko Wolf. Nanoparticle printing with single-particle resolution. *Nature Nanotechnology*, 2(9):570–576, 2007.

[116] Tao Ding, Daniel O Sigle, Lars O Herrmann, D Wolverson, and Jeremy J Baumberg. Nanoimprint lithography of al nanovoids for deep-uv sers. *ACS Applied Materials & Interfaces*, 6(20):17358–17363, 2014.

[117] Se Hyun Ahn and L Jay Guo. Large-area roll-to-roll and roll-to-plate nanoimprint lithography: A step toward high-throughput application of continuous nanoimprinting. *ACS Nano*, 3(8):2304–2310, 2009.

[118] Tobias Seifert, Enrico Sowade, Frank Roscher, Maik Wiemer, Thomas Gessner, and Reinhard R Baumann. Additive manufacturing technologies compared: Morphology of deposits of silver ink using inkjet and aerosol jet printing. *Industrial & Engineering Chemistry Research*, 54(2):769–779, 2015.

[119] Michael Smith, Yeon Sik Choi, Chess Boughey, and Sohini Kar-Narayan. Controlling and assessing the quality of aerosol jet printed features for large area and flexible electronics. *Flexible and Printed Electronics*, 2(1), 2017.

[120] Wei W Yu and Ian M White. Inkjet printed surface enhanced raman spectroscopy array on cellulose paper. *Analytical Chemistry*, 82(23):9626–9630, 2010.

[121] Hongki Kang, Guhaeng Lee, Hyunjun Jung, Jee Woong Lee, and Yoonkey Nam. Inkjet-printed biofunctional thermo-plasmonic interfaces for patterned neuromodulation. *ACS Nano*, 12(2):1128–1138, 2018.

[122] Mykola Borzenkov, Anni Maattanen, Petri Ihalainen, Maddalena Collini, Elisa Cabrini, Giacomo Dacarro, Piersandro Pallavicini, and Giuseppe Chirico. Fabrication of inkjet-printed gold nanostar patterns with photothermal properties on paper substrate. *ACS Applied Materials & Interfaces*, 8(15):9909–9916, 2016.

[123] María Rodríguez Fernández, Eduardo Zalama Casanova, and Ignacio González Alonso. Review of display technologies focusing on power consumption. *Sustainability*, 7(8):10854–10875, 2015.

[124] Swathi Murthy, Henrik Pranov, Nikolaj Agentoft Feidenhansl, Jonas Skovlund Madsen, Poul Erik Hansen, Henrik Chresten Pedersen, and Rafael J Taboryski. Plasmonic color metasurfaces fabricated by a high speed roll-to-roll method. *Nanoscale*, 9(37):14280–14287, 2017.

[125] Yann Leroux, Jean Christophe Lacroix, Claire Fave, Gaelle Trippe, Nordin Félidj, Jean Aubard, Andreas Hohenau, and Joachim R Krenn. Tunable electrochemical switch of the optical properties of metallic nanoparticles. *ACS Nano*, 2(4):728–732, 2008.

[126] Mohammed Mohammed and Rebecca K Kramer. All-printed flexible and stretchable electronics. *Advanced Materials*, 29(19):1604965, 2017.

[127] Daniel Felix Fernandes, Carmel Majidi, and Mahmoud Tavakoli. Digitally printed stretchable electronics: a review. *Journal of Materials Chemistry C*, 7(45):14035–14068, 2019.

[128] Geonhui Lee, Hanul Moon, Hyemin Kim, Gae Hwang Lee, Woosung Kwon, Seunghyup Yoo, David Myung, Seok Hyun Yun, Zhenan Bao, and Sei Kwang Hahn. Multifunctional materials for implantable and wearable photonic healthcare devices. *Nature Reviews Materials*, 5(2):149–165, 2020.

[129] Zhongyang Li, Serkan Butun, and Koray Aydin. Large-area, lithography-free super absorbers and color filters at visible frequencies using ultrathin metallic films. *ACS Photonics*, 2(2):183–188, 2015.

[130] Matthew G. Millyard, Fu Min Huang, Richard White, Elisabetta Spigone, Jani Kivioja, and Jeremy J. Baumberg. Stretch-induced plasmonic anisotropy of self-assembled gold nanoparticle mats. *Applied Physics Letters*, 100(7):073101, 2012.

[131] Fumin Huang and Jeremy J. Baumberg. Actively tuned plasmons on elastomerically driven Au nanoparticle dimers. *Nano Letters*, 10(5):1787–1792, 2010.

[132] Robin M. Cole, Sumeet Mahajan, and Jeremy J. Baumberg. Stretchable metal-elastomer nanovoids for tunable plasmons. *Applied Physics Letters*, 95(15):18–21, 2009.

[133] Xiaolong Zhu, Sanshui Xiao, Lei Shi, Xiaohan Liu, Jian Zi, Ole Hansen, and N Asger Mortensen. A stretch-tunable plasmonic structure with a polarization-dependent response. *Optics Express*, 20(5):5237–5242, 2012.

[134] Li Gao, Yihui Zhang, Hui Zhang, Sage Doshay, Xu Xie, Hongying Luo, Deesha Shah, Yan Shi, Siyi Xu, Hui Fang, Jonathan A. Fan, Peter Nordlander, Yonggang Huang, and John A. Rogers. Optics and Nonlinear Buckling Mechanics in Large-Area, Highly Stretchable Arrays of Plasmonic Nanostructures. *ACS Nano*, 9(6):5968–5975, 2015.

[135] Nina Jiang, Xiaolu Zhuo, and Jianfang Wang. Active Plasmonics: Principles, Structures, and Applications, mar 2018.

[136] Wenzheng Lu, Tsz Him Chow, Sze Nga Lai, Bo Zheng, and Jianfang Wang. Electrochemical switching of plasmonic colors based on polyaniline-coated plasmonic nanocrystals. *ACS Applied Materials & Interfaces*, 2020.

[137] Xiaoyang Duan, Simon Kamin, and Na Liu. Dynamic plasmonic colour display. *Nature Communications*, 8:1–9, 2017.

[138] Jianxiong Li, Simon Kamin, Guoxing Zheng, Frank Neubrech, Shuang Zhang, and Na Liu. Addressable metasurfaces for dynamic holography and optical information encryption. *Science Advances*, 4(6), 2018.

[139] J. F. Elman, J. Greener, C. M. Herzinger, and B. Johs. Characterization of biaxially-stretched plastic films by generalized ellipsometry. *Thin Solid Films*, 313-314:814–818, feb 1998.

[140] Hyeon-Ho Jeong, Melanie C. Adams, Jan-Philipp Günther, Mariana Alarcón-Correa, Insook Kim, Eunjin Choi, Cornelia Miksch, Alison F. Mark, Andrew G. Mark, and Peer Fischer. Arrays of Plasmonic Nanoparticle Dimers with Defined Nanogap Spacers. *ACS Nano*, sep 2019.

[141] Rachel E. Armstrong, Willeke (J.C.) van Liempt, and Peter Zijlstra. Effect of Film Thickness on the Far- and Nearfield Optical Response of Nanoparticle-on-Film Systems. *The Journal of Physical Chemistry C*, 2019.

[142] Shuaidi Zhang, Shengtao Yu, Jing Zhou, James F. Ponder, Marcus J. Smith, John R. Reynolds, and Vladimir V. Tsukruk. Heterogeneous forward and backward scattering modulation by polymer-infused plasmonic nanohole arrays. *Journal of Materials Chemistry C*, 7(10):3090–3099, 2019.

[143] Valentin Flauraud, Massimo Mastrangeli, Gabriel D. Bernasconi, Jeremy Butet, Duncan T.L. Alexander, Elmira Shahrabi, Olivier J.F. Martin, and Juergen Brugger. Nanoscale topographical control of capillary assembly of nanoparticles. *Nature Nanotechnology*, 12(1):73–80, 2017.

[144] Mikhail a. Kats, Romain Blanchard, Patrice Genevet, and Federico Capasso. Nanometre optical coatings based on strong interference effects in highly absorbing media. *Nature Materials*, 12(October 2012), 2012.

[145] Chang Li, Maoxiong Zhao, Xue Zhou, Huizeng Li, Yang Wang, Xiaotian Hu, Mingzhu Li, Lei Shi, and Yanlin Song. Janus Structural Color from a 2D Photonic Crystal Hybrid with a Fabry–Perot Cavity. *Advanced Optical Materials*, 6(20):1–7, 2018.

[146] Grant T. England, Calvin Russell, Elijah Shirman, Theresa Kay, Nicolas Vogel, and Joanna Aizenberg. The Optical Janus Effect: Asymmetric Structural Color Reflection Materials. *Advanced Materials*, 29(29), 2017.

[147] Nityanand Sharma, Hamid Keshmiri, Xiaodong Zhou, Ten It Wong, Christian Petri, Ulrich Jonas, Bo Liedberg, and Jakub Dostalek. Tunable Plasmonic Nanohole Arrays Actuated by a Thermoresponsive Hydrogel Cushion. *Journal of Physical Chemistry C*, 120(1):561–568, 2016.

[148] Courtney D. Sorrell and Michael J. Serpe. Reflection order selectivity of color-tunable poly(N-isopropylacrylamide) microgel based etalons. *Advanced Materials*, 23(35):4088–4092, 2011.

[149] Tomoyuki Yokota, Peter Zalar, Martin Kaltenbrunner, Hiroaki Jinno, Naoji Matsuhisa, Hiroki Kitanosako, Yutaro Tachibana, Wakako Yukita, Mari Koizumi, and Takao Someya. Ultraflexible organic photonic skin. *Science Advances*, 2(4), 2016.

[150] Wei Gao, Sam Emaminejad, Hnin Yin Yin Nyein, Samyuktha Challa, Kevin Chen, Austin Peck, Hossain M Fahad, Hiroki Ota, Hiroshi Shiraki, Daisuke Kiriya, et al. Fully integrated wearable sensor arrays for multiplexed in situ perspiration analysis. *Nature*, 529(7587):509–514, 2016.

[151] Hsinling Liang, Melanie M Bay, Roberto Vadrucci, Charles H Bartyking, Jialong Peng, Jeremy J Baumberg, Michael De Volder, and Silvia Vignolini. Roll-to-roll fabrication of touch-responsive cellulose photonic laminates. *Nature Communications*, 9(1):4632, 2018.

[152] Qibing Pei and Renyuan Qian. Protonation and deprotonation of polypyrrole chain in aqueous solutions. *Synthetic Metals*, 45(1):35–48, 1991.

[153] Yongfang Li and Renyuan Qian. Electrochemical overoxidation of conducting polypyrrole nitrate film in aqueous solutions. *Electrochimica Acta*, 45(11):1727–1731, 2000.

[154] A Robert Hillman, Samantha J Daisley, and Stanley Bruckenstein. Ion and solvent transfers and trapping phenomena during n-doping of pedot films. *Electrochimica Acta*, 53(11):3763–3771, 2008.

[155] Y Hou, Ling Zhang, L Y Chen, Pan Liu, Akihiko Hirata, and Mingwei Chen. Raman characterization of pseudocapacitive behavior of polypyrrole on nanoporous gold. *Physical Chemistry Chemical Physics*, 16(8):3523–3528, 2014.

[156] Marcos Jose Leite Santos, Alexandre G Brolo, and Emerson M Girotto. Study of polaron and bipolaron states in polypyrrole by in situ raman spectroelectrochemistry. *Electrochimica Acta*, 52(20):6141–6145, 2007.

[157] Yu Chuan Liu, Bingjoe Hwang, Wen Jie Jian, and Raman Santhanam. In situ cyclic voltammetry-surface-enhanced raman spectroscopy: Studies on the doping-undoping of polypyrrole film. *Thin Solid Films*, 374(1):85–91, 2000.

[158] Achilleas Savva, Shofarul Wustoni, and Sahika Inal. Ionic-to-electronic coupling efficiency in pedot:pss films operated in aqueous electrolytes. *Journal of Materials Chemistry C*, 6(44):12023–12030, 2018.

[159] S Garreau, G Louarn, J P Buisson, Gerard Froyer, and S Lefrant. In situ spectroelectrochemical raman studies of poly(3,4-ethylenedioxythiophene) (pedt). *Macromolecules*, 32(20):6807–6812, 1999.

[160] Shalini Kulandaivalu, Zulkarnain Zainal, and Yusran Sulaiman. Influence of monomer concentration on the morphologies and electrochemical properties of pedot, pani, and ppy prepared from aqueous solution. *International Journal of Polymer Science*, 2016(2016):1–12, 2016.

[161] Regina Mažeikienė, Gediminas Niaura, and Albertas Malinauskas. Study of redox and protonation processes of polyaniline by the differential multiwavelength raman spectroelectrochemistry. *Spectrochimica Acta Part A: Molecular and Biomolecular Spectroscopy*, 221:117147, 2019.

[162] Regina Mažeikienė, Gediminas Niaura, and Albertas Malinauskas. Raman spectroelectrochemical study of polyaniline at uv, blue, and green laser line excitation in solutions of different ph. *Synthetic Metals*, 243:97–106, 2018.

[163] M C Bernard and A Hugotle Goff. Quantitative characterization of polyaniline films using raman spectroscopy: I: Polaron lattice and bipolaron. *Electrochimica Acta*, 52(2):595–603, 2006.

[164] Peng Wen, Changhui Tan, Junchang Zhang, Fanben Meng, Lin Jiang, Yinghui Sun, and Xiaodong Chen. Chemically tunable photoresponse of ultrathin polypyrrole. *Nanoscale*, 9(23):7760–7764, 2017.

[165] James Nightingale, Jessica Wade, Davide Moia, Jenny Nelson, and Jiseon Kim. Impact of molecular order on polaron formation in conjugated polymers. *Journal of Physical Chemistry C*, 122(51):29129–29140, 2018.

[166] Wing C Tsoi, David T James, Jong Soo Kim, Patrick G Nicholson, Craig E Murphy, D D C Bradley, Jenny Nelson, and Jiseon Kim. The nature of in-plane skeleton raman modes of p3ht and their correlation to the degree of molecular order in p3ht:pcbm blend thin films. *Journal of the American Chemical Society*, 133(25):9834–9843, 2011.

[167] William W Chiu, Jadranka Travassejdic, Ralph P Cooney, and Graham A Bowmaker. Spectroscopic and conductivity studies of doping in chemically synthesized poly(3,4-ethylenedioxythiophene). *Synthetic Metals*, 155(1):80–88, 2005.

[168] Hao Huang, Christoffer Karlsson, Fikret Mamedov, Maria Stromme, Adolf Gogoll, and Martin Sjodin. Polaron disproportionation charge transport in a conducting redox polymer. *Journal of Physical Chemistry C*, 121(24):13078–13083, 2017.

[169] William W. Chiu, Jadranka Travaš-Sejdić, Ralph P. Cooney, and Graham A. Bowmaker. Studies of dopant effects in poly(3,4-ethylenedi-oxythiophene) using raman spectroscopy. *Journal of Raman Spectroscopy*, 37(12):1354–1361, 2006.

[170] JC Thieblemont, A Brun, J Marty, MF Planche, and P Calo. Thermal analysis of polypyrrole oxidation in air. *Polymer*, 36(8):1605–1610, 1995.

[171] Tamer Uyar, Levent Toppare, and Jale Hacaloğlu. Spectroscopic investigation of oxidation of p-toluene sulfonic acid doped polypyrrole. *Synthetic metals*, 123(2):335–342, 2001.

[172] Magatte N Gueye, Alexandre Carella, Jérôme Faure-Vincent, Renaud Demadrille, and Jean-Pierre Simonato. Progress in understanding structure and transport properties of pedot-based materials: A critical review. *Progress in Materials Science*, 108:100616, 2020.

[173] Albertas Malinauskas and Rudolf Holze. Cyclic uv-vis spectrovoltammetry of polyaniline. *Synthetic Metals*, 97(1):31–36, 1998.

[174] Hideyuki Inouye, Koichiro Tanaka, Ichiro Tanahashi, and Kazuyuki Hirao. Ultrafast dynamics of nonequilibrium electrons in a gold nanoparticle system. *Physical Review B*, 57(18):11334–11340, 1998.

[175] Guillaume Baffou and Romain Quidant. Thermo-plasmonics: using metallic nanostructures as nano-sources of heat. *Laser & Photonics Reviews*, 7(2):171–187, 2013.

[176] J Noordegraaf. Conformal coating using parylene polymers. *Medical device technology*, 8(1):14–20, 1997.

[177] Taufik Abidin, Qiang Zhang, Kunli Wang, and Derjang Liaw. Recent advances in electrochromic polymers. *Polymer*, 55(21):5293–5304, 2014.

[178] Ye Shi, Chongbo Ma, Lele Peng, and Guihua Yu. Conductive "smart" hybrid hydrogels with pnipam and nanostructured conductive polymers. *Advanced Functional Materials*, 25(8):1219–1225, 2015.

[179] Yasuhiro Shiraishi, Eri Shirakawa, Kazuya Tanaka, Hirokatsu Sakamoto, Satoshi Ichikawa, and Takayuki Hirai. Spiropyran-modified gold nanoparticles: Reversible size control of aggregates by UV and visible light irradiations. *ACS Applied Materials and Interfaces*, 6(10):7554–7562, 2014.